Spring 5-6-2023

Polycationic Nanoparticle Delivery of Nucleic Acids for the Treatment of Fibrosis in Alcohol-Associated Liver Diseases

Chuhan Zhang
University of Nebraska Medical Center

POLYCATIONIC NANOPARTICLE DELIVERY OF NUCLEIC ACIDS FOR THE TREATMENT OF FIBROSIS IN ALCOHOL-ASSOCIATED LIVER DISEASES

by

Chuhan Zhang

A DISSERTATION

Presented to the Faculty of

the University of Nebraska Graduate College

in Partial Fulfillment of the Requirements

for the Degree of Doctor of Philosophy

Pharmaceutical Science Graduate Program

Under the Supervision of Professor David Oupicky

University of Nebraska Medical Center

Omaha, Nebraska

March 2023

Supervisory Committee:

Benita L. McVicker, Ph.D. Robert G. Bennett, Ph.D.

Martin Conda-Sheridan, Ph.D. Geoffrey M. Thiele, Ph.D.

ACKNOWLEDGEMENTS

I would like to express my deepest appreciation to my professor Dr. David Oupicky for his invaluable patience, mentoring and feedback during my Ph.D. career. I am also deeply grateful for the advice and mentoring from our collaborative professors Dr. McVicker and Dr. Bennett. I also could not have undertaken this journey without my defense committee Dr. Conda-Sheridan and Dr. Thiele, who generously provided knowledge and expertise. Also, I am thankful for all lab members who gave me generous support during my research study. This endeavor would not have been possible without the NIH grant R01 AA027695. My thanks also go to the pharmaceutical science department who gave me kind support. Lastly, I am grateful to my family, especially my parents. Their belief in me has kept my spirits and motivation high during this process.

ABSTRACT

Alcohol-associated liver disease (AALD) is a major cause of liver disorders worldwide. Current treatment options are limited, especially for AALD-related fibrosis. Targeted therapies are urgently needed for severe forms of AALD. In my project, dual-functioning nanoparticles for the effective delivery of antifibrotic RNA were designed and developed, together with combined CXCR4 inhibition or CD44 targeting as a way to improve the treatment of AALD fibrosis. An alcoholic fibrosis model of moderate alcohol consumption with secondary liver insult was built for evaluation of nanoparticle performance in vivo. In Chapter 2, a cholesterol-modified polymeric CXCR4 inhibitor (Chol-PCX) was synthesized and used to encapsulate anti-miR-155. Treatment with the Chol-PCX/anti-miR-155 particles resulted in significantly reduced aminotransferase enzymes as well as collagen content in the liver parenchyma. In Chapter 3, hyaluronic acid-cyclam (HA-C) nanoparticles with CXCR4 and CD44 dual targeting ligands were fabricated to provide an improved biodistribution in AALD. HA-C nanoparticles represent a promising active targeting strategy to deliver nucleic acids to fibrogenic activated HSC (aHSCs), while reducing the uptake to the mononuclear phagocyte system (MPS), therefore, maximizing the therapeutic effect of antifibrotic RNAs. In Chapter 4, biomimetic macrophage membrane-camouflaged miRNA nanocarriers (MP) were formulated. The MP keep the bioactive function of the source macrophage while enabling a prolonged nanoparticle blood circulation time by evading mononuclear phagocytotic system/reticuloendothelial system (MPS/RES), thus, enhancing the nucleic acids delivery to AALD. In conclusion, polymer-based nanoparticles can enhance delivery of nucleic acids to AALD mice and exert antifibrotic effects.

CONTENTS

ACKNOWLEDGEMENTS i

ABSTRACT ii

LIST OF TABLES ix

LIST OF ABBREVIATIONS x

Chapter 1. Introduction 1

1.1 Significance of AALD 1

1.2 Pathogenesis and Fibrogenesis in AALD 2

1.2.1 Steatosis 2

1.2.2 Alcoholic hepatitis (AH) 3

1.2.3 Liver fibrosis 4

1.3 Non-coding RNAs in AALD 6

1.4 Nanoparticle targeting 9

1.5 Recent progress in nanomedicines for liver fibrosis 12

1.6 Interactions between NPs and hepatic cells in AALD 17

1.6.1 Kupffer cells (KCs) 18

1.6.2 Liver sinusoidal endothelial cells (LSECs) 20

1.6.3 Hepatocytes 24

1.6.4 Hepatic stellate cells (HSCs) 26

Chapter 2. Dually active Chol-PCX/anti-miR-155 nanoparticles for the treatment of fibrosis in alcohol-associated liver disease 29

2.1 Introduction 29

2.2 Materials and methods 33

2.2.1 Materials 33

2.2.2 Synthesis and characterization of Chol-PCX 33

2.2.3 Preparation and characterization of PCX/miRNA nanoparticles 34

2.2.4 Cellular viability and cellular trafficking 34

2.2.5 In Vitro miRNA Transfection 35

2.2.6 CXCR4 Antagonism Assay 36

2.2.7 In Vivo Anti-miR-155 Therapy in AALD Fibrosis 36

2.2.8 Biodistribution 38

2.2.9 Histology and Immunohistochemistry 38

2.2.10 Second Harmonic Generation (SHG) Imaging 39

2.2.11 Statistical Analysis 40

2.3. Results 40

2.3.1 Preparation and Characterization of miRNA Nanoparticles 40

2.3.2 Cytotoxicity and Intracellular Trafficking 42

2.3.3 Chol-PCX/anti-miR-155 Nanoparticles Downregulate miR-155 Expression in Macrophages 44

2.3.4 Inhibition of CXCR4 by Chol-PCX in Vitro 45

2.3.5 Chol-PCX Nanoparticles Biodistribution in AALD Fibrosis Model 45

2.3.6 Chol-PCX/anti-miR-155 Treatment Ameliorates AALD Fibrosis 47

2.3.7 Analysis of the Therapeutic Mechanism of Action of the Nanoparticles in AALD Fibrosis 52

2.4 Discussion 57

Chapter 3. Targeted delivery of nucleic acids using hyaluronic acid coated nanoparticles to activated HSCs in AALD 60

3.1 Introduction 60

3.2 Materials and Methods 62

3.2.1 Synthesis of Hyaluronic acid-Cyclam polymer (HA-C) 62

3.2.2 Preparation and Characterization of HA-C Nanoparticles 62

3.2.3 CXCR4 antagonism Assay 63

3.2.4 Cell Viability and Intracellular Trafficking 64

3.2.5 In Vitro miRNA Transfection 65

3.2.6 Biodistribution of HA-C NP in Alcoholic fibrosis 66

3.2.7 Biodistribution on cellular level 66

3.2.8 Statistical Analysis 67

3.3 Results and Discussion 68

3.3.1 aHSCs – Main cell type for liver fibrosis targeting 68

3.3.2 Synthesis and characterization of HA-C polymer 69

3.3.3 CXCR4 antagonism of HA-C 70

3.3.4 Preparation and characterization of HA-C NPs 72

3.3.5 Cytotoxicity and cellular uptake of HA-C NPs/miRNA in hepatic cells 74

3.3.6 Efficacy of HA-C NPs/miRNA transfection 76

3.3.7 In Vivo Tissue Distribution and Cellular Localization of HA-C NPs 77

3.4 Conclusion 81

Chapter 4. Macrophage membrane-camouflaged miRNA nanocarriers ameliorate alcohol-associated liver fibrosis 81

4.1 Introduction 81

4.2 Methods and Materials 84

4.2.1 Isolation of macrophage membranes 84

4.2.2 Preparation and fabrication of MPs 85

4.2.3 Cellular uptake 85

4.2.4 In Vivo Biodistribution of MPs on EtOH/CCl_4 model 85

4.2.5 Flow cytometry 86

4.2.6 In Vivo Anti-fibrosis efficacy measurements of MPs 87

4.2.7 Statistical Analysis 89

4.3 Results and Discussion 89

4.3.1 Fabrication and characterization of MP 89

4.3.2 In vitro toxicity of MP and uptake by macrophages 91

4.3.3 Biodistribution of biomimetic MPs in EtOH/CCl_4 model 91

4.3.4 MP ameliorated fibrosis in EtOH/CCl_4 model 93

4.3.5 MP modulating hepatic microenvironment by recruiting $Ly6C^{lo}$ phenotype restorative macrophages 95

4.4 Conclusion 96

Discussion 96

Future work 99

Bibliography 100

List of Figures

Figure 1. Schematic illustration of the mechanisms of the antifibrotic effect of Chol-PCX/anti-miR-155. 32

Figure 2. Characterization of Chol-PCX/anti-miR-155. 41

Figure 3. Cytotoxicity of Chol-PCX and Chol-PCX/anti-miR-155. 42

Figure 4. Cellular uptake of Chol-PCX/FITC-RNA. 43

Figure 5. Transfection efficiency of Chol-PCX/anti-miR-155. 44

Figure 6. CXCR4 redistribution. 45

Figure 7. Biodistribution of Chol-PCX and PEI Cy5.5-siRNA nanoparticles. 47

Figure 8. Experimental and treatment scheme. 48

Figure 9. Hepatic CXCR4, Col1a1, and miR-155 gene expression, ALT and AST levels. 49

Figure 10. Therapeutic efficacy of Chol-PCX/anti-miR-155 in AALD fibrosis. 50

Figure 11. SHG imaging of liver collagen fibers. 52

Figure 12. Analysis of AALD fibrosis markers. 53

Figure 13. Immunohistochemistry for F4/80 (total macrophage or KCs stain) and CD163 (M2 phenotype). 55

Figure 14. Immunohistochemistry for α-SMA (activated HSCs stain) and CD44. 57

Figure 15. Immunohistochemistry for α-SMA (activated HSC stain) and CD44. 69

Figure 17. NMR of HA and HA-C. 70

Figure 16. Synthesis scheme for HA-C. 70

Figure 18. HA-C polymer and CXCR4 antagonism. 72

Figure 19. HA-C NP formulation. 74

Figure 20. Cytotoxicity of HA-C NPs on hepatic cells. 75

Figure 21. Cellular uptake of HA-C NPs in mpHSC. 76

Figure 22. Efficacy of HA-C NPs/miR-34a transfection on aHSC. 77

Figure 23. Biodistribution of HA-C NPs. 79

Figure 24. Multi-color flow cytometry sorting by different antibodies, including myeloid cells and non-parenchymal cells. 80

Figure 25. Fluorescent NPs distribution on cellular level and quantification of MFI of NPs in different cells. 80

Figure 26. Comparison of Cy5.5 fluorescence in different hepatic cells in alcoholic liver. 81

Figure 27. Mechanism of biomimetic NPs (MP) for the treatment of alcohol-associated liver fibrosis. 84

Figure 28. Fabrication of biomimetic nanoparticles. 89

Figure 29. Characterization of biomimetic NPs. 90

Figure 30. Biodistribution of MP in alcoholic liver fibrosis. 92

Figure 31. Therapeutic effects of MP/anti-miR-NC on alcoholic liver fibrosis. 94

Figure 32. Antifibrotic mechanism of MPs. 95

LIST OF TABLES

Table 1. MiRNAs in AALD 7

Table 2. Nanoparticles targeting to hepatic cells via specific ligand-receptor interactions. 16

LIST OF ABBREVIATIONS

AALD	Alcohol-associated liver disease
AAV	Adeno-associated virus vector
ADH	Alcohol dehydrogenases
AH	Alcoholic hepatitis
AKT	Protein kinase B
ALT	Alanine aminotransferase
AMPK	AMP-activated protein kinase
APCs	Antigen present cells
ApoE	Apolipoprotein E
ASGP	Asialoglycoprotein
ASO	Antisense oligonucleotide
AST	Aspartate aminotransferase
αSMA	Alpha-smooth muscle actin
BDL	Bile duct ligation
BMDM	Bone marrow derived macrophage
BSA	Bovine serum albumin
CCl_4	Carbon tetrachloride
CLRs	C-type lectin receptors
CYP	Cytochromes P450
DALYs	Disability-adjusted life years

DAMP	Damage-associated molecular patterns
DC	Dendritic cells
ECM	Extracellular matrix
FDA	U.S. Food and Drug Administration
FSA	Formaldehyde-treated serum albumin
FXR	Farnesoid X receptor
GalNAc	N-acetylgalactosamine
GMP	Germacrone
Gli2	GLI family zinc finger 2
HA	Hyaluronic acids
HA-C	Hyaluronic acid-cyclam
HARE	Hyaluronan receptor for endocytosis
hATTR	Hereditary transthyretin (TTR)-mediated amyloidosis (hATTR)
HCC	Hepatocellular carcinoma
HCV	Hepatitis C Virus
HEPES	(4-(2-hydroxyethyl)-1-piperazineethanesulfonic acid)
HIF1α	Hypoxia inducible factor 1 alpha
HSC	Hepatic stellate cell
IKKε	IκB kinase ε
KC	Kupffer cell

KLF2	Kruppel-like factor 2
KO	Knockout
LDLR	Low density lipoprotein receptor
LPS	Lipopolysaccharides
LSEC	Liver sinusoidal endothelial cell
IFN	Interferon
IL	Interleukin
IRF3	Interferon regulatory factor 3
M6P	Mannose 6-phosphate
MAPK	Mitogen-activated protein kinases
mDF	Maddrey discriminant function
MELD	The model for endstage liver disease scores
MHC	Major histocompatibility complex
MMPs	Metalloproteinases
MPS	Mononuclear phagocytotic system
MRs	Mannose receptors
MyD88	Myeloid differentiation factor 88
NADH/NAD+	Nicotinamide adenine dinucleotide
NAFLD	Non-alcoholic fatty liver disease
NFκB	Nuclear Factor kappa B
NK cells	Nature killer cells
NMR	Nuclear magnetic resonance

NPs	Nanoparticles
NVs	Nanovesicles
PAMP	Pathogen-associated molecular patterns
PDGF	Platelet-derived growth factor
PD-L1	Programmed cell death protein-1
PEG	Polyethylene glycol
PLGA	Polylactic-co-glycolic acid
PIK3	Phosphoinositide 3-kinases
PPAR	Peroxisome proliferator-activated receptors
PR	Pattern recognition receptors
PS	Polystyrene
QDs	Quantum dots
RANTES	Regulated upon Activation, Normal T Cell Expressed and Presumably Secreted
RES	Reticuloendothelial system
RBP	Retinol binding protein
ROS	Reactive oxygen species
SHG	Second Harmonic Generation
SMV	Simvastatin
STAT	Signal Transducer and activator of transcription
SREBP1-c	Sterol regulatory element-binding protein

SRs	Scavenger receptors
TGF-β	Transforming Growth Factor-β
TIMPs	Tissue inhibitors of metalloproteinases
TLR	Toll-like receptors
TRIF	Toll-IL-1-resistance (TIR) domain-containing adaptor-inducing interferon-β
TNF-α	Tumor necrosis factor alpha
TTR	Hereditary transthyretin
Tregs	Regulatory T cells
VLDL	Very low-density lipoprotein
VIS	Vismodegib

Chapter 1. Introduction

1.1 Significance of AALD

In 2016, it was estimated that 3 million deaths (5.3% of all deaths) were attributable to the harmful use of alcohol worldwide. Alcohol consumption also accounts for 132.6 million disability-adjusted life years (DALYs) accounting for 5.1% of all DALYs in a single year [1]. Chronic liver disease and cirrhosis became the 9th leading cause of death in the United States in 2021[2]. Alcohol intake is the leading cause of liver cirrhosis, responsible for majority of alcohol-related morbidity and mortality [3]. AALD represents a wide spectrum of liver pathologies, starting from steatosis, steatohepatitis, to liver fibrosis and cirrhosis. Almost all heavy alcohol drinkers are generally asymptomatic. According to a previous study, only 20–40% of alcoholics develop fibrosis, 10–20% eventually progress to cirrhosis, and 1–2% of cirrhosis patients are eventually diagnosed with hepatocellular carcinoma [4].

Cessation of alcohol use reverses the early fatty liver, however, other forms of AALD tend to decompensate even with abstinence. Many factors are associated with the progression of AALD, including female sex, smoking, obesity, and genetic polymorphisms [5]. Treatment for AALD is mainly through pharmacological therapies and non-pharmacological interventions. Corticosteroids, e.g. prednisolone, are the standard of care for severe alcoholic hepatitis, however, side effects and high risk of infections are important considerations for their use. Severity of AALD is determined by the Maddrey discriminant function (mDF) that represent histological steatohepatitis, or by the model for end-stage liver disease scores (MELD). Patients

with mDF >32 and MELD >20 are considered to have high risk for short-term mortality and experience with severe alcoholic hepatitis that can be treated with corticosteroids [6]. For patients who fail to respond to corticosteroids, liver transplantation is another treatment option [5]. There are plenty of antioxidants and anti-inflammatory drugs that are being developed and show potential in AALD treatment, such as the antioxidant N-acetylcysteine, IL-1β inhibitor Anakinra, anti-fibrotic IL-22, and anti-TNFα antibody as well as bile acid receptor farnesoid X receptor (FXR) inhibitor obeticholic acid [7]. However, there are no pharmacological therapeutics approved in clinics for AALD. Therefore, more efforts are urgently needed to develop targeted therapeutics for severe forms (e.g., alcoholic hepatitis and fibrosis) of AALD.

1.2 Pathogenesis and Fibrogenesis in AALD

AALD occurs on the multicellular levels, involving parenchymal hepatocytes and innate immune cells, mainly Kupffer cells (KCs) [8]. Alcohol-induced hepatocyte injury and KC activation further activate hepatic stellate cells (HSCs) to promote liver fibrosis during AALD. Here we describe the pathogenesis during the progressive stages of AALD.

1.2.1 Steatosis

Steatosis is characterized by fat accumulation in hepatocytes. The pathogenesis of alcohol steatosis is complicated and is currently explained by several different mechanisms, including increased fatty acid synthesis, decreased β-oxidation of fatty acids, and inhibition of very low-density lipoprotein (VLDL) secretion to the blood [9]. It is largely unknown what is the main molecular mechanism involved in steatosis. Alcohol consumption can directly or indirectly

regulate lipid metabolism-associated transcription factors, such as acetaldehyde, NADH/NAD+, adiponectin, AMP-activated protein kinase (AMPK), which increase sterol regulatory element-binding protein (SREBP1-c) and downregulate peroxisome proliferator activated receptor α (PPARα) [10,11]. Elevated SREBP-1c is related to expression of lipogenic enzymes as well as the accumulation of triglycerides in the liver. The decrease of PPARα causes the reduction of fatty acid β-oxidation genes, leading to the inhibition of fatty acid β-oxidation. Increased lipogenesis and decreased fatty acid β-oxidation together initialize the histologic steatosis [12].

1.2.2 Alcoholic hepatitis (AH)

AH is inflammation in AALD that is histologically characterized by the infiltration of neutrophils, hepatocyte ballooning, and Mallory-Denk hyaline inclusions [13]. Alcoholic liver damage is regulated directly by alcohol or indirectly by the alcohol metabolites. Alcohol is primarily metabolized in the liver to acetaldehyde by alcohol dehydrogenase, cytochrome P450 (CYP) enzyme complex and catalase. CYP ethanol metabolizing enzyme systems are more abundant in centrilobular than periportal hepatocytes, which causes a zonal pattern of lesions. Acetaldehyde is directly toxic to hepatocytes, leading to elevated reactive oxygen species (ROS), mitochondrial damage, and S-adenosylmethionine depletion. Overall, disturbances of lipid metabolism prime hepatocellular injury shown by the hepatocellular ballooning or death [11].

AH includes innate and adaptive immune responses. LPS from the alcohol-induced leaky gut recognizes receptor complexes including TLR4 and its coreceptors [14]. In non-parenchymal KCs, TLR4 triggers signaling that includes the myeloid differentiation factor 88 (MyD88)

dependent pathway to activate nuclear factor kappa B (NF-κB), or MyD88-independent pathway to activate Toll-IL-1-resistance (TIR) domain-containing adaptor-inducing interferon-β/interferon regulatory factor-3 (TRIF/IRF3). These pathways promote the secretion of TNF-α to activate innate immune responses [15,16]. In parenchymal cells, TLR4 can trigger MyD88-independent signaling which causes activation of IRF3 and an increase of downstream type I IFN and delayed NF-κB activation. These signals suppress proinflammatory cytokines like TNF-α, which in turn modulates the inflammatory function in non-parenchymal immune cells [17]. Other innate immune events include complement C3 and C5 activation that can stimulate KC activation to produce TNF-α [18]. Alcohol intake promotes the ROS stress through activation of LPS/TLR4. One of the consequences of ROS is formation of lipid peroxidation adducts like malondialdehyde or 4-hydroxynonenal that can serve as antigens for adaptive immune responses. The increased number of T and B cells as well as the circulating antibodies against lipid peroxidation adducts mark the activation of an adaptive immune response in AH [19].

1.2.3 Liver fibrosis

Liver fibrosis is a wound-healing process characterized by extracellular matrix deposition that can exist in all kinds of chronic liver injury. Alcohol-induced liver fibrosis is the main stage we are investigating in AALD. The predominant cause of liver fibrogenesis is the activation of HSCs. Extracellular matrix (ECM) deposition and alpha-smooth muscle actin (αSMA) increase caused by the trans-differentiation and activation of HSCs myofibroblasts is important for the pathogenesis of AALD fibrosis. ECM deposition mainly occurs in the space of Disse and

circumscribing hepatocytes [20]. The space of Disse is the home for HSCs, it is a location that separates parenchymal hepatocytes and liver sinusoids. In the healthy state, type IV and VI are the major constitutes of collagen fibers, providing a structural scaffold and architecture for the space of Disse. Following the activation of HSCs, type I and III collagen are excessively produced resulting in ECM deposition and the progression of liver fibrosis [21].

Ballooning and dying hepatocytes secrete hedgehog ligands that induce αSMA and vimentin gene elevation in adjacent stromal cells that promote the activation of HSCs [22]. The dying hepatocytes also produce damage-associated molecular patterns, which in combination with ROS released from alcohol metabolism activate KCs and induce the hepatic inflammation [13,23]. Hedgehog ligands from ballooned or dying hepatocytes, inflammatory chemokines from activated Kupffer cells, LPS translocation from leaky gut, and alcohol metabolites (i.e., acetaldehyde), are all critical factors for the activation of HSCs [24].

A centrilobular pattern of injury implicated by perivenular fibrosis can be developed in fatty liver diseases including AALD and advanced non-alcoholic fatty liver (NAFLD) compared to the portal-based fibrosis pattern in most chronic liver diseases, such as viral hepatitis. This centrilobular pattern is formed by the configuration of ethanol metabolizing enzyme systems, e.g. CYP2E1 which are more predominantly found in centrilobular than periportal hepatocytes. The main components of ECM include fibrillar collagen types I, III and IV, integrins, proteoglycans, hyaluronan, and fibronectin, which can further fuel the fibrogenesis by contributing to the survival of activated HSCs. [20].

Furthermore, alcohol can inhibit antifibrotic mechanisms. The most important one is the inhibition of natural killer cell-mediated interferon-gamma (IFN-γ)-induced elimination of

activated HSCs. The antifibrotic NK cells can directly stop HSC activation and proliferation, or indirectly secrete IFN-α and IFN-γ which induce apoptosis or inhibit the cell cycle progression of HSCs [25]. However, long-term alcohol consumption significantly impedes the functions of antifibrotic NK cells, accelerating the fibrosis progression. Moreover, the activated HSCs produce tissue inhibitors of metalloproteinases (TIMPs) which in turn inhibit the ECM dissolving metalloproteinases (MMPs). Profibrogenic activity related to KC activation and hepatic inflammation induce prolonged survival of activated HSCs [26]. These ongoing hepatic events accelerate the disruption of the lobular architecture, the development of hepatic fibrosis, and advancement to cirrhosis. Collectively, these antifibrotic effects are suppressed by alcohol.

1.3 Non-coding RNAs in AALD

Over the past decade, RNA-based therapeutics such as, siRNA, antisense oligonucleotides (ASO), and mRNA have gained interest and have been extensively developed. Among them, miRNAs are short, endogenous, 21-23 nucleotides RNA molecules that participate in regulatory mechanisms and can serve as promising therapeutic targets for various diseases [27]. The miRNAs regulate gene expression by binding to 3'UTR of mRNAs, with complementary binding resulting in mRNA degradation while non-complementary pairing causes translation regression. miRNAs can bind to more than one mRNA instead of one specific mRNA substrate [28]. The main hurdle of RNA therapy is efficient delivery to diseased organs and cells with efficient penetration of cell membranes in order to perform intracellular actions. Furthermore, unprotected RNAs are degraded by nucleases in serum. As such, early terminations of clinical trials for some of non-coding RNAs (ncRNAs) have resulted because of inefficient delivery

and toxicity. MiRNAs are involved in multiple pathologies of AALD, including inflammation, oxidative stress, lipid metabolism, and apoptosis, providing promising targets for treatment of AALD. In this section, miRNAs involved in the progression of AALD are discussed (Table 1).

Table 1. MiRNAs in AALD

MiRNAs	**Regulation**	**Mechanisms**	**Functions**	**Ref**
miR212	Upregulation	LPS/TLR4	inflammation	[29]
miR155	Upregulation	LPS/TLR4, PPRE/PPARα	inflammation, steatosis, fibrosis	[30]
miR21	Upregulation	IL-6/Stat3, LPS/TLR4	Inflammation,	[31]
miR34a	Downregulation	TGF-β1/Smad2/3, SIRT1/p53	fibrosis	[32] [33]
miR122	Downregulation	Inhibiting hypoxia inducible factor 1(HIF1α)	steatosis, inflammation, and hepatocytes apoptosis	[34]
miR217	Upregulation	SIRT1 suppression	steatosis	[35]

During AALD, alcohol-induced miR-212 upregulation increases intestinal hyperpermeability by inhibiting Zonula occludens (ZO-1) protein synthesis [29], thus leading to translocation of LPS to liver through the portal vein. LPS/TLR4 is the main axis for inflammation, in which miR125b, miR146a, miR132 and miR155 regulate inflammatory responses to LPS and innate immune responses. TNFα secretion by the resident liver macrophages, KCs, play important roles in inflammation and steatosis. Chronic alcohol consumption increases miR-155

expression, which enhances the LPS-induced TNFα production through increasing TNFα mRNA stability and its translation [30]. Alcohol can induce LPS/TLR4 signaling to promote miR-155 production. MiR-155 upregulation mainly occurs in hepatocytes and KCs, which promotes fat accumulation by decreasing peroxisome proliferator-activated receptor response element (PPRE) and peroxisome proliferator-activated receptor (PPAR). The alcohol-induced increase in neutrophil, leukocyte, and profibrotic $CD163^{+}CD206^{+}$ (M2) macrophages were prevented in miR-155 knockout (KO) mice in a CCL_4 induced liver fibrosis mouse model and alcohol fed mice [15]. Increased miR146a expression negatively regulates chemokines IL-8 and RANTES (Regulated upon Activation, Normal T Cell Expressed and Presumably Secreted) upon IL-1β-induced inflammation and thus serves a protection effect for AALD [36]. miR21 shows a positive correlation in the up-regulation of LPS signaling with alcohol consumption when produced by MyD88 pathway in a NF-κB-dependent pathway in macrophages [37]. Alcohol also activates IL-6/Stat3 signaling that increases miR-21 levels in hepatocytes and HSCs. miR-21 regulates cell cycle and mediates an anti-apoptotic response through synergistic effects induced by IL-6 [31]. MiR-34a upregulates TGF-β1/Smad2/3 pathway to increase proinflammatory cytokines, which contribute to liver fibrosis [32].

Alcohol exposure regulates a series of miRNAs involved in cell apoptosis. Alcohol markedly upregulates miR-34a expression, which is a critical regulator of apoptosis. Overexpression of miR-34a decreases SIRT1 (silent mating type information regulation 2 homolog 1) expression, causing an increase in acetylated p53 levels and p53 targets, like p21. This miR-34a/SIRT1/p53 signaling induces apoptosis and cell cycle arrest of hepatocytes to promote alcohol-associated liver fibrosis [33]. MiR-34a expression is also regulated epigenetically. Alcohol exposure

induces hypomethylation of the miR-34a promoter, which is associated with the elevation of miR-34a in the liver, which in turn activates caspase-2 and sirtuin 1. miR-34a promotes the activity of MMP-2 and MMP-9 as well, mediating the liver tissue remodeling and the formation of liver fibrosis [38].

MiR-122 reduction in hepatocytes contributes to steatosis, inflammation, and hepatocytes apoptosis in AALD. Restoration of miR-122 levels reverses hepatic injury via the inhibition of hypoxia inducible factor 1(HIF1α) after alcohol administration [34]. In healthy liver, miR-34a is anti-apoptotic and cooperatively regulates the balance of proliferation and cell cycle with miR-122. However, in the alcohol liver a miR-34a increase and a miR-122 reduction break the balance of gene expression, exacerbating liver injury by increased cell proliferation of hepatocytes and HSCs [39]. Other miRNA changes, like the increase of miR-217 abundance in the alcoholic liver results in SIRT1 suppression and promotion of the steatosis [35].

In my study, miR-155 is the main target for the treatment of liver fibrosis in AALD. Polymeric nanoparticles were used to delivery anti-miR-155 to silence the increased miR-155 in activated KCs to suppress profibrotic effects in AALD.

1.4 Nanoparticle targeting

The journey of nanoparticles begins with the injection into the bloodstream and continues with distribution to the site of action, endocytosis, endosomal escape, intracellular localization and finally action. However, there are barriers at every level of drug distribution, including systemic tissue and cellular levels for drug delivery to the site of action [40]. Physicochemical properties largely determine the fate of nanoparticles in the body. Knowledge on manipulating the

properties of nanoparticles is helpful for targeting to disease sites to give sufficient concentration of drugs for efficient therapeutic effects. Efficient nano system delivery relies on specific targeting to desired tissues and cell types through targeting mechanisms categorized as passive, active, and endogenous targeting [41].

Passive targeting refers to tuning the physical properties of a nanomedicine such as size, morphology, surface charge, hydrophilicity, and hydrophobicity that can navigate particle movement to target sites. The enhanced permeability/ retention effect is one example of passive targeting and regarded as main principle for tumor drug delivery systems. Special biological structures in tumor, including hypervasculature, leaky blood vessels, and impaired lymphatic drainage, enable enhanced permeability and retention of large particles including liposomes, micelles, proteins and macromolecules, into the interstitial space of the tumor [42]. For passive targeting to liver, the fenestrated endothelium in the unique liver sinusoids structure in the body need to be considered when designing NPs. In healthy humans, the size of liver sinusoidal endothelial cell (LSEC) fenestrae is around 50-300 nm. Nanoparticles that are of small size are prone to passively move through the fenestrae to arrive at aHSC and hepatocytes [43]. However, perisinusoidal fibrosis formation involves LSEC capillarization and defenestration which impedes nanoparticle crossing the sinusoids [44].

Active targeting is based on ligand affinity to receptors on cells to deliver a certain amount of nucleic acids or drugs to specific sites of disease [45]. Usually, highly selective targeting ligands are modified on the surface of nanoparticles. These ligands could be peptides, antibodies or small molecules that specifically bind to the receptors on the target sites. One example of active targeting is tripeptide (RGD)-targeted nanocarriers. Extracellular matrix (ECM) composed of

fibronectin, collagens, and osteopontin are rich in tumors or liver fibrosis. RGD is a common peptide sequence for these proteins and is responsible for cell adhesion by binding to the integrins on the cell surface. Integrins regulate angiogenesis and RGD conjugated or modified nanoparticles are widely used as targeting to tumors or liver fibrosis. Examples include RGD peptide cross-linked cyclodextrin for the targeted delivery of doxorubicin as an chemotherapy modality [46]. Another example is cRGDfK modified Polyethylene glycol-Polylactic-co-glycolic acid (PEG-PLGA) NPs delivered with germacrone (GMP), miR-29b, or RGD-Lip/vismodegib to treat liver fibrosis [47,48].

Endogenous targeting indicates engineering a nanoparticle through changing physicochemical properties or modifying with special ligand to make it bind to a distinct subset of plasma proteins, which navigate it to a specific population of cells [41]. Nanoparticles are exposed to high protein concentrations after systemic administration. Opsonins in serum bind to NPs, forming corona proteins on the surface of NPs and the sequestration and removal of the modified NPs by cells of the MPS/RES [49]. Phagocytosis and clearance of NPs by MPS is one of the major hurdles for targeted delivery. Phagocytic cells in MPS include hepatic KCs, splenic red pulp, marginal zone macrophages, as well as bone marrow derived macrophages and LSECs [50]. Corona proteins formed on NPs surface may have dramatically difference when varying the physiochemical parameters of NPs, such as surface charge, functional group [49]. Corona might block the modified ligands on NPs and hamper their targeting functions to specific cells. Hydrophilic PEG modification of NPs is widely used to avoid opsonization. PEGylated liposomes are referred as to “stealth liposomes” which show dose-independent pharmacokinetics. PEG helps avoid NPs binding to serum opsonins, prolonging blood

circulation time in body [51]. Other strategies to prevent MPS uptake include saturation of the Kupffer cell phagocytic response or depletion of RES macrophages using clodronate liposome [52]. Whereas researchers also tried to leverage the corona to dictate the nanoparticles to their destination. For example, Zhang et al. conjugated retinol on the small molecular weight polyethyleneimine (PEI) to actively recruit plasma proteins, particularly retinol binding protein (RBP), to form corona on the NPs surface. In a murine model of liver fibrosis, the RBP/retinol NPs successfully delivered antifibrogenic antisense oligonucleotide (ASO) uptake into fibrogenic HSCs [53].

1.5 Recent progress in nanomedicines for liver fibrosis

Some antifibrotic treatment attempts have been made with numerous small molecules and compounds being tested in clinical trials. Clinical antifibrotic therapies mainly encompass two categories, that is, etiology treatments and antifibrotic therapeutics. Many innovative therapies like interleukin 10 (IL10), angiotensin II antagonists, and interferon γ (IFNγ) remain successful in preclinical trials [54], however, there is a lack of cause-specific treatments for chronic liver diseases, especially for liver fibrosis. The underlying reasons are 1) the complicated molecular mechanisms of liver fibrosis; 2) traditional formulations devoid of efficient targeting to specific pathogenetic sites; 3) murine models that cannot mimic all the conditions of chronic liver fibrosis; and 4) the inability to recruit appropriate patients for prospective clinical trials [55]. All these reasons lead to a lack of pharmacotherapy to date for liver fibrosis [22]. Among them, the lack of specific targeting to responsible cells or molecules reduces efficient drug concentration at the target site and induces side-effects in non-target tissues [56]. One example

is the clinical application for IFNs which are widely accepted as anti-fibrotic cytokines in vitro and in CCl_4 or dimethylnitrosamine animal models [57,58]. However, an anti-fibrotic effect was not achieved in clinical trials due to poor efficacy, disappointing off-target effects, and short half-life periods [56]. Thus, better systems are required to improve the delivery efficiency of nucleic acids and small molecules. Furthermore, naked genetic drugs including DNA and RNA molecules are easily degraded by enzymes in biological fluids and thus cannot get to target tissues or penetrate the cell membrane even if they arrive at target sites. NPs, like LNPs lead non-viral delivery systems to protect genetic drugs from degradation and endocytosis into cells [59]. Small molecules have been widely studied in various diseases; however, their clinical uses are limited by poor solubility, nonspecific targeting and inefficient biodistribution. NPs can enhance drug efficacy by improving drug solubility, increasing drug $t_{1/2}$ in circulation, and targeting to specific tissue and cells as well as providing constant drug release [60].

During the last several decades, gene-based treatment strategies have become a promising therapeutic opportunity for liver fibrosis. Research demonstrates gene-based drug treatments for various diseases by silencing pathogenic genes, expressing therapeutic proteins, and editing gene defects to regulate a series of downstream pathogenic behaviors [27]. In 2017, the FDA-approved LUXTURNA™ used for the treatment of inherited retinal disease marked a breakthrough in gene therapy development. Also, the first gene therapy for haemophilia B, Hemgenix, an adeno-associated virus vector–based (AAV) gene therapeutic expressing the hyperactive FIX-Padua variant targeting to liver cells was approved in 2022. Additionally, oligonucleotides including siRNAs, ncRNAs, and ASO have been actively developed for use in clinical trials. Several oligonucleotides and one siRNA therapeutic have received FDA

approval. For example, Patisiran, an siRNA therapeutic, was approved in 2018 to treat hereditary transthyretin (TTR)–mediated amyloidosis (ATTR). Numerous studies have been focused on genetic changes in the pathogenesis of AALD. For example, IFNγ induces downstream gene STAT1 which reverses liver fibrosis through inhibition of HSC activation via attenuation of TGF-β signaling and abrogation of NK cell-mediated elimination of aHSCs [25]. Other promising targets are miRNAs, such as miR-155, miR-132, and miR-21 that are upregulated in AALD through LPS/TLR4 signaling as illustrated in section 1.3.

Other therapeutics such as small molecules have been widely developed for biomedical applications. Small molecule therapies for liver fibrosis like sorafenib, one of the PDGFR-β antagonists, results in the inhibition of HSC proliferation and related effects such as reductions in portal pressure in cirrhotic rats, intrahepatic fibrosis and liver injury, angiogenesis, and inflammation [61,62]. In humans, Sorafenib was approved for the treatment of advanced HCC patients [63]. However, the efficacy of sorafenib was limited due to its insolubility in water and toxicity in clinical practice, which have hampered its pharmacodynamic actions [64].

Nanomedicines designed for site-specific targeting have been used for delivering gene therapeutics, small molecules, proteins, or cytokines. Nanomedicines include inorganic nanoparticles (NPs), lipid NPs, and synthetic polymers. The successful liver delivery of drug or gene therapy could be ascribed to the favorable physiology of the liver, which is highly perfused and encompasses a fenestrated endothelium, enabling NPs equipped with naturally liver oriented physical properties. Furthermore, targeting effects via specific ligand-receptor interactions navigate NPs to arrive at particular hepatic cell types. Such nanomedicines accumulate in the sites of diseases to overcome the shortcomings that traditional therapeutics

cannot conquer. Currently, there are few studies published for alcoholic liver targeting, however, implications could be found from other liver diseases using NPs. Multiple gene-based therapeutics using NPs targeting to liver cells are under clinical trials or approved by FDA. Patisiran (ONPATTRO^{TM}), the first RNAi-based therapy to treat hereditary transthyretin (TTR)-mediated amyloidosis (hATTR), is formulated in LNPs that target hepatocytes that produce TTR. Another case is a Vitamin A-coupled liposome encapsulate HSP47 siRNA (BMS-986263) developed for silencing HSP47 to inhibit collagen secretion in hepatic fibrosis. The safety and effectiveness of BMS-986263 has been tested in a Phase 2 clinical trial in hepatic cirrhosis and fibrosis patients (NCT03420768) [65]. Most of the nanoparticles delivered by systemic administration are taken up by the liver and typically retained in the MPS even though the majority of the parenchyma is composed of hepatocytes [66]. Physicochemical properties influence the efficiency of NP delivery of nucleic acids to hepatic cells. The size of nanoparticles is among the most important factors influencing NP-hepatic cell interactions. The particle size plays a pivotal role in the cellular uptake, intracellular trafficking, biodistribution, and toxicity of nanoparticles. Relatively large particles are prone to uptake by macrophages. NPs smaller than 100 nm tend to cross the liver fenestrae and be taken up by HSCs and hepatocytes [43]. Nanoparticles larger than 200 nm are prone to stay in the sinusoid and be taken up by LSECs and KCs [67].

Thus, to achieve selective uptake by specific populations of hepatic cells, the most effective way is active targeting [67]. Table 2 summarizes studies published to date for the active targeting of nanoparticles for liver fibrosis. The reports are categorized by specific ligand-receptor bindings and implications for the design of nanomedicines for alcohol-associated liver

fibrosis could be found from the identified NPs.

Table 2. Nanoparticles targeting to hepatic cells via specific ligand-receptor interactions.

Cell types	Ligand-receptor binding		Gene or drug delivery	size	ξ	Ref
	receptor	ligand				
HSC	RBP	Vitamin A	Va-coupled Valsartan liposome	169.9±2.4nm	35.7±0.8 mV	[68]
			VA-modified core-shell polymer micelles loaded with Silibinin/siCol1α1	150nm	7mV	[69]
			Collagenase I and retinol co decorated PLGA-PEG-Mal nanodrill loaded with nilotinib	217.0±8.1nm	-16.55 ± 2.92mV	[70]
	Sigma-1 receptor	aminoethyl anisamide (AEAA)	AEAA-LNP/pRLN	189.5nm	-6.82mV	[71]
	CD44	Hyaluronic acids (HA)	silibinin-loaded HA micelles	44.9±2.1nm	-15.2±2.3 mV	[72]
	Fibroblast activation protein (FAP)	Promelittin	Promelittin-modified liposomes	160nm	-37mV	[73]
	CXCR4	Cyclam	Chol-PCX /anti-miR-155 polyplex	~70nm	25mV	[74]
	Platelet-derived growth factor receptor beta (PDGFR-β)	Anti-PDGFRβ	gold nanorods coated with anti-PDGFRβ	n/a	n/a	[75]
			Chitosan NPs/TGF-β1 siRNA	110±6nm	35±1mV	[76]
		Cyclic peptides (pPB)	IFN-γ encapsulated in sterically stable liposomes modified by pPB	83.5nm	n/a	[77]
	M6P receptor	M6P-BSA	M6P-BSA-conjugated hesperidin liposome	238.8 ± 75.85nm	-26.7 ± 9.17nm	[78]
	Integrin αvβ3	cRGDfK peptides	cRGDfK modified -PEG-PLGA NPs codeliver GMP and miR-29b	231.2nm	-12.0mV	[48]
		cRGDyK peptides	RGD-Lip/vismodegib	75.6±2.4nm	-24.8±1.8 mV	[47]
KC	Mannose receptor	Mannose	Mannosylated liposomes	~95nm	n/a	[79]
			Mannosylated cationic liposomes/NFκB decoy complex	64.6±1.70nm	61.4±0.91mV	[80]
			Mannosylated cationic liposomes/Plasmid DNA	200nm	~12mV	[81]
			Mannose-modified trimethyl chitosan-cysteine (MTC) conjugate NPs/TNF-α siRNA	146.9±5.4nm	25.9±0.9 mV	[82]

	Galactose receptor	Lactobionic acid	Galactosylated LDL nanoparticle	27nm	n/a	[83]
	Scavenger receptor	BSA/IgG and calcitriol	QDs	34.6nm	-29.7mV	[84]
	Fucose receptor	Fucosylated lipid	Fuc-liposome/NFκB decoy	64.5±1.84nm	37.4±2.84mV	[85]
Hep	LDLr	ApoE	high-Chol phospholipid-free small unilamellar vesicles / doxorubicin	76.5±4.5nm	-5.5±3.5mV	[86]
		Cholesterol ApoE	a DNA tetrahedron with trivalent cholesterol conjugation /TGF-β ASO	n/a	n/a	[87]
	ASGPRs	Galactose/GalNAc	GalNAc moiety conjugated to the AlgS-Ca2+-siRNA	~140nm	<-10mV	[88]
	Glycyrrhizin receptor	Glycyrrhizin	Glycyrrhizin conjugated chitosan nanoparticles	145.8±4.2nm	15.6±0.8mV	[89]
			Glycyrrhizin-modified O-carboxymethyl chitosan nanoparticles	111.9±1.0nm	-30.3±0.3mV	[90]
LSEC	Stabilin2/HARE	HA	PLL-g-HA/DNA	100-200nm	n/a	[91]
			HA coated QDs	50-120nm	n/a	[92]
	Stabilin2	Formaldehyde-BSA (FSA)	Ag2S-QD-FSA	72.5 ± 5.3nm	-35.2 ± 0.7mV	[93]
	Mannose/scavenger	Mannan	Mannan or ApoBP coated PLGA NPs /ovalbumin (NPOVA)	NPOVA/man: 279.5±2.74nm NPOVA/ApoBP: 268.8±4.96nm	NP OVA-man: -51.63±4.05mV NPOVA/ApoBP:-8.63±1.38mV	[80]
LSEC/HSC	HARE/CD44	HA	HA derivatives conjugated quantum dots	42.3nm	-21.3mV	[67]
	HARE, CD44, IFNα receptor	HARE, CD44, IFNα	AuNPs	52.23nm	n/a	[94]

1.6 Interactions between NPs and hepatic cells in AALD

As the largest solid organ in the body, the liver is composed of parenchymal cells and non-parenchymal cells. Hepatocytes account for about 60-80% of hepatic parenchymal cells. Non-

parenchymal cells include LSCEs, HSCs, KCs, infiltrating macrophages, cholangiocytes, and resident immune cells [95].

Hepatic artery, portal vein, and bile duct form portal triads in the liver and arrays of these triads form discrete polygonal liver lobules. Blood from hepatic artery and portal vein traverses the liver lobules via the special channels of liver called hepatic sinusoids and then drains to the central vein [96]. Nanoparticles like liposomes or polymeric NPs are mainly metabolized and cleared by the MPS or through the hepatobiliary system [66]. To understand the fate, therapeutic effects, and metabolism of the NPs, the characterization of hepatic cell type clearance mechanisms is of great importance. Physiochemical properties such as size and surface charge of NPs can influence distribution to specific cell types [97]. Active targeting strategies using selective ligand-receptor binding enable specific delivery to certain populations of hepatic cells. Here are some understandings from current studies of nanomaterials to describe the factors and barriers that influence distribution of NPs to different hepatic cells in liver fibrosis.

1.6.1 Kupffer cells (KCs)

In sinusoids, KCs are resident tissue macrophages responsible for removing foreign particles from circulation and they account for 80-90% of the total macrophage population in the body. Initially, yolk sac is the first organ where macrophages develop in mammals, primitive or fetal macrophages migrate from bloodstream to colonize in the fetal liver. After the initiation of bone marrow hematopoiesis in animals [98], KCs are derived from monocytes that originate from precursor cells in the bone marrow. Monocytes migrate from the peripheral blood circulation to the liver and then they mature into resident tissue macrophages with differentiated surface

receptors specific for foreign materials [98]. Except for KCs, many of the macrophages that appear with injury also come from bone marrow derived macrophages (BMDMs) that home to the liver. As the first line of the innate immune system, KCs are the main cell type in MPS, serving as a key phagocytic system in the body [99]. Activation of KCs during alcoholic liver injury can induce a series of events such as cytokine/chemokine production and the recruitment of other immune cells into the liver. KCs play major roles in mediating innate immune responses. KCs crosstalk with other hepatic cells including HSCs to facilitate AALD progression [100]. Overall, the dysregulation of inflammatory responses in KCs is a main contributor for chronic inflammation in AALD.

For many nanomedicine applications, the initial uptake by KCs is considered a drawback because avoiding the surveillance of nanoparticles from blood circulation by KCs is a problematic issue for selective distribution to other desired targets. The underlying reason is highly cationic and anionic nanoparticles bind with opsonins, forming ‘protein corona’, which makes them prone to aggregate and be phagocytosed by KCs. To increase the specific uptake by other liver cells, the neutral nanoparticles using PEG coating or PEG-like hydrophilic polymers may impart “stealth” properties and help reduce the surface protein adhesion to evade opsonization [101]. Indeed, PEGylation has become the mainstay for prolonging circulation time of intravenous therapies since the first FDA-approved PEGylated liposome Doxil®. By increasing the PEG density on the surface of polystyrene (PS) NPs, the blood circulation time is significantly increased [102]. One pharmacokinetic study showed that dense PEG coating was leveraged to improve brain tissue penetration of PS NPs. In that study, PS-PEG NPs remained in systemic bloodstream, whereas uncoated PS-COOH NPs accumulated in the liver

[103].

In contrast, NPs targeting KCs could be developed to reduce inflammatory pathogenic signaling. KCs internalize nanoparticles via multiple scavenger, toll-like, mannose, and Fc receptors. Mannose receptors (MRs) like CD206 belong to the C-type lectin receptors (CLRs) superfamily and the SR-E family expressed in the mice or humans [104]. Mannose, fucose, and galactose bind to MRs overexpressed on antigen presenting cells and macrophages which are desirable targets on KCs [11]. Mannosylated nanocarriers including mannosylated liposomes or BSA provide opportunities for NPs targeting to KCs [81].

1.6.2 Liver sinusoidal endothelial cells (LSECs)

Liver endothelial cells line close to KCs in the liver sinusoids. Unlike other endothelium, there is no basement membrane, instead fenestrae form between LSECs allowing for blood to pass through the Space of Disse, where hepatocytes and HSCs are located. It was demonstrated that chronic alcohol consumption contributes to the loss of fenestrae, nevertheless, there is no deep understanding of direct or indirect reason for the correlation of alcohol and fenestrae changes [105]. LSECs fenestrae have size in a range of 50-200 nm that varies based on the animal species and liver disease stage. From one previous study, the average diameter in humans is 107±1.5 nm, which is significantly smaller than in C57BL/6 mice (141±5.4 nm) or Sprague–Dawley rats (161±2.7 nm) [106].

In healthy states, LSECs protect HSCs from activation and keep homeostasis in the liver. In cirrhosis, LSECs become capillarized, meaning they lose their fenestrae and impede nanodrug transport across the membrane and infiltration into the Space of Disse [107]. Zhang et al.

engineered a LSEC-targeting and fenestrae-repairing nanoparticle using hyaluronic acids (HA) and vitamin A modified liposome loaded with simvastatin (SMV) to target LSEC and HSC. In fibrotic mice, the HA-NPs/SMV repairs the first barrier of the endothelium capillarization, then collagenase I on the CV-NPs/ siCol1α ablates collagen in ECM, and the vitamin A ligand targets to aHSC for the siCol1α delivery [108]. Off-target effect could be one limitation for this nanoparticle since HA not only express on LSECs but also on HSCs or Hepatocytes [109,110].

In mammals, the body's largest scavenger endothelial cell (SEC) is LSEC. As part of the MPS, LSECs express several common receptors with KCs, including mannose, scavenger receptor (SR) and Fc-γRIIb2 [111]. Zebrafish is a model organism offering a reference to higher organism to explore preclinical pharmacokinetics of nanomedicines in LSEC. 3 days post-fertilization at which embryonic macrophages display basic immune and homeostatic functions of liver were chosen where macrophages and SECs showed a competitive nature of SiO2 NPs clearance. The underlying trafficking mechanism for SECs is the fast route of micropinocytosis [112]. Among the receptors on LSEC, stabilin-1 and stabilin-2 SRs are mainly expressed on LSEC, whereas mannose receptors also appear on the KC surface [113]. Stabilins were reported to preferentially bind and internalize large polyanionic components of the ECM, such as HA, dermatan sulfates, chondroitin and other glycosaminoglycans. Campbell et al. studied that the uptake of anionic liposome in zebrafish SECs was effectively prevented by knockout of the stabilin-2 gene [114]. Hyaluronic acid-conjugated nanoparticles were successfully delivered to LSECs through binding with SRs as well [108].

Liver has a unique system of antigen presenting cells (APCs), including natural tolerogenic APCs such as KC, dendritic cells (DC) and LSECs. LSEC lining the hepatic sinusoids,

expresses pattern recognition receptors (PR), especially Toll-like receptors (TLR). LSECs efficiently scavenge blood-born antigen and are able to present it on MHC-class I and II molecules to T cells. Orally ingested antigens or intravenously injected soluble antigens have been observed to induce immune tolerance by LSEC through the production of antigen-specific Tregs, TGF-β generation and upregulation of programmed cell death protein 1 (PD-L1) for PD-1 receptor [115]. Liu et al. designed polylactic-co-glycolic acid (PLGA) NPs with ligands that target scavenger and mannose receptors on the liver APC -LSEC to generate regulatory T-cells (Tregs) to induce immune suppression effects [80].

Larger nanoparticles (>500 nm) are prone to be taken up by KCs, whereas soluble macromolecules or small particles are likely cleared preferentially by clathrin-mediated endocytosis in nonphagocytic LSECs [113]. LSECs can compensate the phagocytic function of KCs, helping the internalization of particles sizing up to 1000 nm. LSECs are regarded to avidly endocytose collagen degradation products, heparin, and formaldehyde-treated serum albumin (FSA). In one study, Hunt et al. generated quantum dots (QDs) coated with either FSA, heparin, or gelatin. They aimed to leverage endocytosis of macromolecules by LSECs. Oral administration was preferred instead of parenteral injection of QDs because the target cells are LSECs. LSECs are the first organ-based cells exposed to orally administrated QDs once they are absorbed and traversed though portal vein. Therefore, oral administration enhances selective uptake of QDs to LSECs. Among these various coated QDs, FSA and gelatin coating performed high specificity targeting and bioavailability via clathrin- and caveolae-mediated pathways in mice [93].

Adjusting the size of particles and PEG content is another method to navigate the lipid

nanoparticles (LNPs) to cell types other than liver hepatocytes, especially to LSECs. Kim et al. engineered different PEG lipid content to adjust the particle uptake by hepatic cells. Transfection efficiency of LNPs was tested on hepatocytes where the presence of Cre recombinase can induce tdTomato expression. Higher PEG content LNPs have reduced ApoE absorption and when loaded with Cre recombinase mRNA, there is a reduced tdTomato fluorescence in hepatocytes attributable to this reduced ApoE-mediated cellular uptake of LNPs [116]. It was found that as the PEG-lipid content increases from 1, 1.5 to 3.0%, the size of LNP reduces from 100 nm to 60 nm. Correspondingly, 1.0% PEG-lipid LNPs with size around 100 nm showed highest LSECs uptake compared with 1.5% and 3.0% PEG-lipid with size around 60 nm. The reason is when the size of LNPs is less than LSEC fenestrae diameter (100 nm), LNPs can target to hepatocytes through fenestrae. But the relatively large particles likely stay on liver sinusoids interacting with LSECs for cellular entry. However, only by adjusting the PEG content cannot achieve LSEC specific targeting. Incorporation of mannose to these LNPs further allowed for the selective delivery of RNA to LSECs, which minimize the undesired cellular uptake by hepatocytes [116].

Manipulating hydrophobicity and hydrophilicity of NPs also increases the possibility of targeting to LSEC. Lee et al. showed that hydrophobic surfaced-silica NPs were preferentially taken up by LSECs, whereas hydrophilic surfaced-silica NPs mainly went to HSCs. They also clarified that hydrophilic modifications NPs mainly uptake by KCs (38%) and HSCs (29%) followed by LSECs and hepatocytes [117].

1.6.3 Hepatocytes

Hepatocytes play pivotal roles in the pathogenesis of various liver diseases because they are involved in a broad array of liver functions, including bile production and metabolism. Alcohol use can alter the metabolism. Cytochrome P4502E1 (CYP2E1) and alcohol dehydrogenase (ADH) enzymes in hepatocytes are responsible for the oxidation of ethanol to acetaldehyde. The elevated oxidative stress and lipid peroxidation correlates with the increased CYP2E1 and ADH levels in AALD [118]. Chronic alcohol consumption causes functional impairments in hepatocytes including a change in the number of organelles due to mitochondrial stress, damaged Golgi trafficking, endoplasmic reticulum stress, microtubule dysfunction, impaired activity of the proteasome, and dysregulated histone acetylation. Consequently, these events lead to a profound impact on detoxification and metabolic activities which sensitize hepatocytes to necrosis and apoptosis [119] [120,121].

Hepatocytes are a main cell type for hepatic gene therapy via delivery to widely characterized hepatocyte receptors, the low-density lipoprotein receptor (LDLR) and the asialoglycoprotein (ASGP) receptor [122]. Apolipoproteins are well-known ligands for LDLRs which play a crucial role in the hepatocellular clearance of lipoproteins in the body [123]. ApoE can serve as an endogenous targeting ligand for ionizable LNPs (iLNPs), but not cationic LNPs (cLNPs). Most of the ionizable lipids in LNPs contain lipid headgroups with weak basicity. The surface charge of the iLNPs changes in a pH-dependent manner. They are positively charged at acidic pH but close to neutral at physiologic pH in circulation. Neutral liposomes were found to absorb ApoE to enhance uptake into hepatoma cells or hepatocytes [124]. Research shows that iLNP binding to recombinant ApoE3, the dominant isoform in humans, showed significantly

enhanced cellular uptake and GFP gene silencing effect on Hela cells compared with cLNPs. Silencing factor VII activity of iLNP supplemented with ApoE was found to be efficient in an ApoE dose dependent manner in ApoE-/- mice [125]. LNPs enter cells in a cell type-specific manner using clathrin-mediated endocytosis as well as micropinocytosis [126].

The ASGPR is a highly expressed receptor on hepatocytes with approximately 500,000 copies per cell. The ASGPR is a high-capacity receptor which has innate binding affinity to a broad range of ligands, including galactose, and N-acetylgalactosamine residues, like lactose, galactoside, and asialofetuin [127]. Among the ligands, N-acetylgalactosamine (GalNAc) targeting liposomes are investigated in a large number of research and clinical trials. The affinity of GalNAc to ASGPR is approximately 50-fold higher than D-galactose (Gal). GalNAc liposomes showed higher overall targeting efficiency in vivo and in cultured HepG2 cells [128]. GalNAc is an amino sugar derivative of galactose that binds to ASGPR, however, KCs express homologous C-lectin type receptors that have the similar affinity to GalNAc, resulting in the targeting effect of GalNAc liposomes to both hepatocytes and KCs in the liver.

Glycyrrhizin/glycyrrhetinic acid (GL/GA) receptors on the hepatocyte cell membrane take up GL/GA through receptor-mediated endocytosis. Even though GL/GA receptors are also expressed on other organs, such as kidney, colon, they have antihepatitis and anti-hepatotoxic functions, enabling their useful therapeutic targeting to hepatocytes [89]. For instance, Glycyrrhizin-modified O-carboxymethal chitosan NPs (PTXCMCNP-GL) or Glycyrrhizin-conjugated chitosan nanoparticles (GL-LMWC-NPs) were designed to target HCC [90]

1.6.4 Hepatic stellate cells (HSCs)

Quiescent HSCs are located in the perisinusoidal Space of Disse. They function as pericytes and store around 80% vitamin A in healthy humans. After liver injury and following stimulation by fibrogenic mediator, the expression of vitamin A, GFAP, and PPARγ downregulate in quiescent HSC. qHSCs therefore differentiate to activated collagen type I-producing myofibroblasts, promoting extracellular matrix deposition and connective scar tissue formation [26]. As activation of HSC is a major factor in the development of liver fibrosis, most of the NPs for liver fibrosis aim to target aHSCs. To arrive at aHSCs, particles should be small enough due to the small average diameter of liver fenestrae. The accumulation of ECM in the Space of Disse functions as a physiological barrier that impedes the transport of particles from the endothelial cells to hepatocytes and HSCs. To achieve the best antifibrotic impact, nanosystems with proteolytic surface molecules like collagenase can facilitate their penetration in physiological ECM barriers and improve the delivery efficiency to HSCs [129]. Several studies exemplified that the in situ breaking down ECM collagen barriers by collagenase increases drug penetration. For example, a collagenase I and retinol co-decorated PLGA-PEG-MAL polymeric micelle possesses nanodrill-like and HSC-targeting function for liver fibrosis therapy [70]. Also, Glycyrrhetinic acid (GA)-conjugated prodrug micellar system with collagenase I (COL) decoration (CHG) increased sorafenib delivery to HSCs and potentiated ECM degradation in fibrotic mice [130].

The two potent profibrogenic factors for HSC activation and fibrogenesis include transforming growth factor-β (TGF-β) and the connective tissue growth factor platelet-derived growth factor (PDGF) in injured liver. PDGF receptor is an assembled dimer connected by disulfide bonds.

PDGF binding to its receptor PDGFR-β triggers the stimulation of HSC proliferation via the PI3K/AKT signaling pathway to promote TGF-β secretion, collagen deposition, and angiogenesis [131]. The construction of nanomedicines using PDGFRβ-specific polypeptides could selectively target to the upregulated PDGFR-β on aHSCs. For example, IFNγ loaded into PDGFR binding cyclic peptide pPB liposomes (SSLs) enhanced the delivery of IFNγ to aHSC [77].

Other receptors on aHSCs are also investigated. Integrins receptors on aHSCs bind to a family of cell adhesion molecules in ECM, such as type VI collagen and fibronectin, regulating a diverse array of cellular functions crucial to the biological functions in liver. All the adhesion molecules contain the RGD peptide sequence, which is modified on nanoparticles to have high affinity and selectivity for integrin αvβ3 [77]. Work by Li et al. proved the cRGDyK-guided liposomes loaded with vismodegib have high selectivity toward activated HSCs, but not quiescent HSCs, and preferentially accumulates in fibrotic liver, effectively inhibits the Hh pathway and deactivation of HSCs both in vitro and in vivo [47]. Vitamin A (VA) modified nanoparticle is another delivery system for antifibrosis therapy to aHSCs. VA binds with retinol binding proteins (RBP) then to RBP receptors on the surface of HSC. VA-conjugated valsartan loaded liposomes and Silibinin/siCol1α1 co-loaded core-shell VA-modified polymer micelles (PVMs), exhibited selective genes or small molecules delivery to aHSCs [68,69]. Mannose-6-phosphate/IGF-IIreceptor plays a crucial role in regulating cell growth and lysosome targeting ability. M6P-modified human serum albumin (M6P26-HSA)/ 18β-glycyrrhetinic acid (18β-GA) treatment showed substantially reduced ALT and AST level and improved collagen deposition compared with mice injected with 18β-glycyrrhetinic acid alone in BDL model [132].

In my study, CXCR4 antagonist cyclam conjugated on polymers were used to target aHSCs. CXCR4/CXCL12 signaling can induce HSC activation both in vivo and in vitro. This activation of HSCs is marked by increased expression of α-SMA and type I collagen, forming hepatic fibrosis [133]. Also, by triggering CXCL4/CXCL12 signaling, there was an upregulation of immune cell infiltration in patients with liver hepatic fibrosis [134]. Previous study on CXCR4-targeted NPs showed successful delivery of vascular endothelial growth factor (VEGF) siRNAs to fibrotic livers, suppression of angiogenesis, and normalization of distorted vessels in a CCl_4 mouse model [135].

Chapter 2. Dually active Chol-PCX/anti-miR-155 nanoparticles for the treatment of fibrosis in alcohol-associated liver disease

2.1 Introduction

Alcohol overuse causes damage to the liver and multiple other organs. Up to a third of people who misuse alcohol develop liver damage [136,137]. Long-term alcohol consumption causes chronic liver disease, including liver fibrosis, cirrhosis, and hepatocellular carcinoma [121]. There are no approved treatments for liver fibrosis, resulting in liver transplantation as the only curative option. The mechanisms underlying alcohol-associated liver disease (AALD) are complicated. Heavy alcohol use can affect fatty acid synthesis and oxidation [138,139]. Furthermore, alcohol-related changes in gut permeability increase portal vein endotoxins, leading to innate immune responses and liver inflammation through the activation of several cytokine cascades. Multiple hepatic cells are involved in modulating the complex liver microenvironment, including resident macrophages (e.g.,, Kupffer cells (KCs), hepatic stellate cells (HSCs), liver sinusoidal endothelial cells (LSECs), and hepatocytes [95]. A central event during AALD is the sensitization of KCs, resulting in the promotion of inflammatory factors and fibrogenesis rather than wound healing. The KC inflammatory response leads to the production of cytokines/chemokines and reactive oxygen species that promote the transformation of normally quiescent HSCs into an activated myofibroblast phenotype that facilitates the deposition of extracellular matrix (ECM) and scar formation [140]. The events surrounding KC and HSC activities during AALD progression provide opportunities for targeted drug delivery to improve treatment.

Nanoparticle delivery systems have been developed for a range of liver diseases due to their tendency to accumulate in the liver [141,142]. However, very few nanoparticle delivery systems have been tested in alcohol-associated liver fibrosis models. Therefore we focused on delivery carrier mechanisms for AALD fibrosis. The use of nanoparticles for the treatment of AALD fibrosis is appropriate as nanoparticles are efficiently taken up by KCs followed by other hepatic cells, including LSECs and HSCs [143-147]. The predominant uptake in KCs is due to their phagocytic nature and portal location. To further enhance the specificity of nanoparticle delivery, specific ligands can be used to partially redirect uptake from KCs to other types of hepatic cells.

RNA interference (RNAi) is a promising method for treating various diseases, including cardiovascular disorders, cancers, and liver problems [148]. The biggest challenge to the use of RNAi is successful systemic delivery, because small RNAs, such as siRNA and miRNA, are unstable in serum and their highly negative charge makes crossing cell membranes difficult. However, nanoparticles can be used to encapsulate small RNAs to achieve targeted delivery to disease sites, thereby overcoming the obstacles of unencapsulated RNA [149]. MiRNAs are small, endogenous, non-coding 21–23-nucleotide RNAs that participate in various regulatory mechanisms in liver diseases. They regulate gene expression by binding to the 3′ untranslated region of target mRNA to suppress translation or induce mRNA cleavage [150]. Among potential targets in AALD, miR-155 is involved in the pathogenesis of the disease, with reported upregulation in KCs and hepatocytes [151]. The therapeutic potential of the miR-155 pathway was demonstrated by reduced fat accumulation in miR-155 knockout (KO) mice through an increase in peroxisome proliferator hormone response elements binding with peroxisome

proliferator-activated receptors in KCs [15]. Lipopolysaccharide (LPS) is recognized by the Toll-like receptor (TLR) 4 complex and is considered an important player in regulating inflammatory cytokine activation in the liver. Through continuous alcohol exposure, KCs are sensitized by LPS, which induces an inflammatory response. Thus, miR-155 knockdown can reduce alcohol-induced liver injury, steatosis, and inflammation by the inhibition of TLR4 signaling [152].

The activation of HSCs is an important event in the development and progression of fibrosis during AALD [153]. Among various chemokine receptors, CXC receptor 4 (CXCR4) and its ligand, CXCL12, are overexpressed in activated HSCs known to regulate pathogenic mechanisms. CXCR4 promotes the activation and differentiation of HSCs in liver fibrosis through MAPK activation [154]. Though there is no consensus on the role of CXCR4 in AALD fibrosis, there are studies showing that the blockade of CXCR4 signaling suppresses HSC activation and proliferation, leading to a downregulation of collagen I and α-SMA expression in liver fibrosis [133,154].

Our previous studies reported on the development of a series of polycationic CXCR4 antagonists (PCX) that deliver siRNA and miRNA in various disease models, including metastatic cancers, leukemia, and lung fibrosis [155-157]. Small-molecule CXCR4 antagonists, such as AMD3100, show therapeutic effects stemming from the inhibition of the CXCL12/CXCR4 axis [158]. Here, we hypothesized that nanoparticles consisting of the CXCR4-inhibiting PCX and encapsulated miRNA will be capable of therapeutically targeting both the KCs and activated HSCs in AALD. For our investigation, we performed the synthesis

of cholesterol- modified PCX (PCX-Chol) based on polyethyleneimine (PEI) as a system to simultaneously target activated HSCs and KCs in a model of AALD fibrosis. Figure 1 illustrates the proposed mechanism of action of the PCX system for the delivery of anti-miR-155. This study characterized the effect of nanoparticles on miR-155 and CXCR4 expression as well as therapeutic outcomes in a model of hepatic fibrosis during AALD.

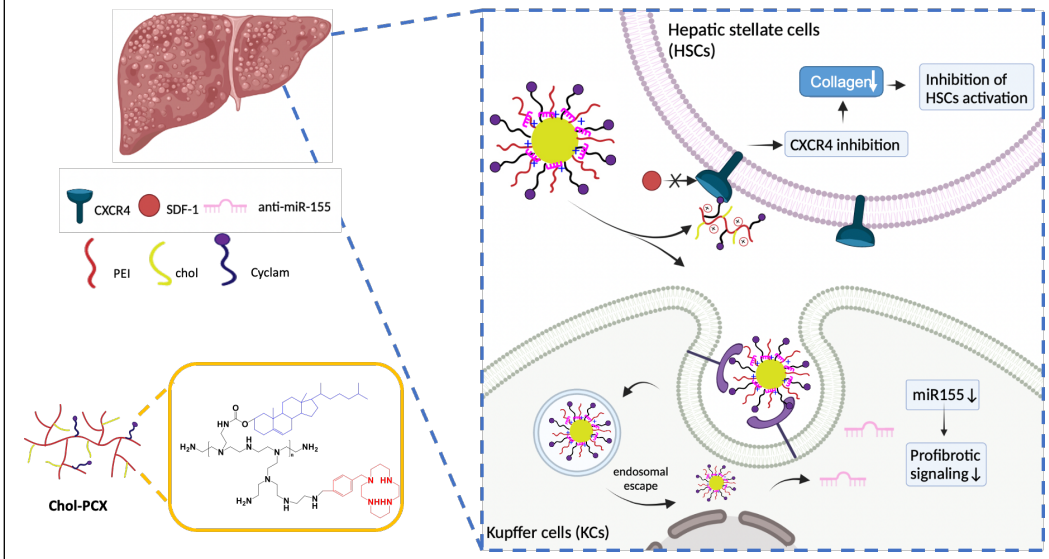

Figure 1. Schematic illustration of the mechanisms of the antifibrotic effect of Chol-PCX/anti-miR-155.

2.2 Materials and methods

2.2.1 Materials

Cyclam (1,4,8,11-tetraazacyclotetradecane) was purchased from Sigma-Aldrich (St. Louis, MO). Branched PEI (10 kDa) was from Polysciences (Warrington, PA). Solvents (certified ACS grade) were purchased from Fisher and used without further purification. miRIAN microRNA hairpin inhibitor (anti-miR-155) and miRIDIAN microRNA hairpin inhibitor negative control (anti-miR-NC) were bought from Horizon (Perkin Elmer, UK). Dulbecco's phosphate buffered saline (PBS), trypsin, penicillin/streptomycin (Pen-Strep), Dulbecco's modified Eagle medium (DMEM), and fetal bovine serum (FBS) were from Hyclone (Waltham, MA). FAMTM Dye-Labeled anti-miRTM Negative Control was purchased from Fisher. Lipopolysaccharides (LPS) from Escherichia coli O127:B8 was bought from Sigma. CXCR4, type I collagen (Col1a1), matrix metalloproteinases (MMPs) and tissue inhibitors of metalloproteinases (TIMPs) primers were from Sigma.

2.2.2 Synthesis and characterization of Chol-PCX

PEI (64.65 mg), tri-tert-butyl-11-(4-(chloromethyl)benzyl)-1,4,8,11-tetraazacyclotetradecane-1,4,8-tricarboxylate (772 mg, 1.2 mmol) (synthesized as previously described [159]), and potassium carbonate (415 mg, 3 mM) were suspended in acetonitrile (20 mL) and refluxed for 16 h, followed by filtration and solvent evaporation to obtain PCX. The PCX (100 mg) was then dissolved in a mixture of anhydrous methylene chloride and N,N-diisopropylethylamine. Cholesteryl chloroformate (15 mg, 3.3 mM) in anhydrous methylene chloride was added

dropwise over 1 h. The reaction was continued under stirring for another 24 h. The product was obtained by evaporating the solvent and washing with diethyl ether three times to remove the unreacted cholesteryl chloroformate. Trifluoroacetic acid (20 mL) was added, and the mixture stirred overnight to remove the t-butyloxycarbonyl (Boc) pro-tecting groups prior to dialysis against distilled water and lyophilization to obtain Chol-PCX. 1H NMR spectrum of Chol-PCX in DMSO-d6 was recorded on a Bruker 500 MHz NMR spectrometer at room temperature.

2.2.3 Preparation and characterization of PCX/miRNA nanoparticles

The nanoparticles were prepared by mixing equal volume of miRNA (20 μg/mL in 10 mM HEPES, pH 7.4) and Chol-PCX to achieve the desired polymer/RNA w/w ratios and incubated at room temperature for 30 min before further use. Hydrodynamic particle size and zeta potential were measured by dynamic light scattering (DLS) at 25°C using Malvern NANO ZS (UK).

2.2.4 Cellular viability and cellular trafficking

Immortalized human HSC cells (LX-2 cells, received as a kind gift from Dr. Scott L. Friedman, Icahn School of Medicine at Mount Sinai [160]) were cultured under 5% CO2 in DMEM supplemented with 2% FBS and 1% Pen-Strep at 37°C. Murine RAW 264.7 macrophages (ATCC, Manassas, VA) were cultured under 5% CO2 in DMEM supplemented with 10% FBS and 1% Pen-Strep at 37°C. When confluency reached 80-90%, the cells were trypsinized and subcultured.

Cell viability was evaluated by the CellTiterBlue assay following the manufacturer's protocol

(Promega Corp.). In brief, cells were seeded in a 96-well plate and cultured for 20-24 h. A series of increasing concentrations of the polymers and nanoparticles were added, and the plates incubated at 37℃ for 24 h. Cell viability was normalized to cells incubated with PBS by measuring the absorbance at 560Ex/590Em nm using a SpectraMax iD3 Multi-Mode Microplate Reader.

For uptake evaluation, the cells were seeded in 12-well plates and cultured to 60% confluency. The cells were incubated with the nanoparticles containing fluorescently labeled FAM-miRNA (100 nM) for 4 h. Cellular uptake was measured in trypsinized cells using a BD FACS LSR II green flow cytometer.

2.2.5 In Vitro miRNA Transfection

RAW 264.7 cells (2×10^5 cells/well) were seeded in 6-well plates and cultured to 60% confluency. The cells were incubated with the nanoparticles (100 nM of anti-miR-155) or 100 nM of anti-miR-155/Lipofectamine 2000 as

the positive control for 6 h in a serum-free medium, then removing the nanoparticle solutions followed by stimulation with LPS (100 ng/mL) for 24 h. RT-PCR analysis was performed using a Rotor-Gene Q (QIAGEN) thermocycler with a miRCURY LNA miRNA PCR Starter Kit (QIAGEN). The universal reverse transcription was followed by real-time PCR amplification with the LNA-enhanced primers. MiR-155 expression was expressed relative to the internal control UniSp6.

2.2.6 CXCR4 Antagonism Assay

The CXCR4 antagonism efficacy of Chol-PCX was determined by a CXCR4 redistribution assay. Human epithelial osteosarcoma U2OS cells with EGFP-CXCR4 fusion protein (Fisher Scientific Waltham, MA, USA) were cultured in DMEM supplemented with 2 × 10−3 M L-glutamine, penicillin (100 U/mL), streptomycin (100 µg/mL), G418 (0.5 mg/mL), and 10% FBS. The cells (8000 cells/well) were seeded in black 96-well microplates. After 24 h, the cells were washed with an assay buffer and treated with Chol-PCX at different concentrations for 30 min. AMD3100 (300 nM) was used as a positive control. The CXCL12 (10 nM) was added and incubated for 1 h. Cells were fixed and visualized using EVOS xl microscopy under the GFP channel.

2.2.7 In Vivo Anti-miR-155 Therapy in AALD Fibrosis

All animal experiments were performed in C57BL/6 female mice purchased from Jackson Laboratories and following the protocol approved by the University of Nebraska Medical Center Institutional Animal Care and Use Committee. An AALD fibrosis model was established by feeding the mice an EtOH-containing Lieber–DeCarli (LD) daily liquid diet (Dyets Inc., Bethlehem, PA, USA) combined with repeated intraperitoneal injection of CCl_4 for 3 weeks, modified from a previous report [161]. In brief, on day 0 mice were started on 1% (v/v) EtOH LD liquid diet or control isocaloric liquid diet without EtOH for two days. Starting on day 3, the mice were injected twice per week with CCl_4 (1 mL/kg of 10%CCl_4 in olive oil) and fed with 2% EtOH LD liquid diet or the control isocaloric diet. The daily intake of the EtOH mice was monitored, and the following day the equivalent calories were administered to control mice.

Starting the second week, mice were injected twice with the treatment or control nanoparticles. All nanoparticle treatments were given 24 h after a CCl_4 injection. There were four treatment groups, with 6 mice per group: (i) pair-fed control, (ii) EtOH LD diet + CCl_4 + PBS, (iii) EtOH LD diet + CCl_4 + Chol-PCX/anti-miR- NC, and (iv) EtOH LD diet + CCl_4 + Chol-PCX/anti-miR-155. Nanoparticles (10 μL/kg) were injected via tail vein at a dose of 1 mg/kg of miRNA and a polymer/miRNA ratio of 4. Mice were sacrificed 24 h after the last treatment and the liver tissues as well as the blood samples were collected. The livers were stored in RNAlater (Qiagen, Valencia, CA, USA) or 10% formalin. The mRNA expression of fibrotic markers was analyzed by SYBR Green RT-PCR. Extracted RNA (2 μg) was converted into cDNA using a High-Capacity cDNA Transcription Kit (Applied Biosystems, Waltham, MA, USA). The PCR reactions were run on Rotor-Gene Q (QIAGEN) equipment with iTaq Universal SYBR Green Supermix (Bio- Rad, Hercules, CA, USA) and GAPDH as a housekeeping gene. Relative mRNA levels were calculated based on the comparative threshold value (Ct) method. Primers used are as follows:

FM1_Col1a1: CGTATVACCAAACTCAGAAG
RM1_Col1a1: GAAGCAAAGTTTCCTCCAAG
FM1_MMP2: GAGATCTTCTTCTTCAAGGAC
RM1_MMP2: AATAGACCCAGTACTCATTCC
FM1_MMP9: CTTCCAGTACCAAGACAAAG,
RM1_MMP9: ACCTTGTTCACCTCATTTTG;
FM1_MMP13: CTTTAGAGGGAGAAAATTCTGG,

RM1_MMP13: CATCATCATAACTCCACACG;
FM1_Timp2: GGATTCAGTATGAGATCAAGC
RM1_Timp2: GCCTTTCCTGCAATTAGATAC

The serum concentration of alanine transaminase (ALT) and aspartate amino transaminase (AST) was determined by a VITROS 5.1 FS Chemistry System (Ortho Clinical diagnostics) at the Omaha VA Medical Center Clinical Chemistry Laboratory.

2.2.8 Biodistribution

AALD fibrosis in C57BL/6J mice was induced as stated in Section 2.7. Then, both the EtOH mice and pair-fed mice were injected intravenously with 200 μL of fluorescently labeled Cy3−Chol−PCX/Cy5.5−siRNA or Cy3−PEI/cy5.5−siRNA (1 mg/kg Cy5.5−siRNA, 4 mg/kg Cy3−Chol−PCX or Cy3−PEI). Mice were sacrificed 24 h post-injection, and major organs were harvested for imaging by Xenogen IVIS 200.

2.2.9 Histology and Immunohistochemistry

The liver specimens were fixed in 10% formalin overnight and then embedded in paraffin. Sections (5 μm) were stained with Sirius Red, hematoxylin and eosin (H&E), and Masson's trichrome by the UNMC Tissue Sciences Facility. Brightfield images at low power (10× objective) were captured for at least 5 random fields per sample using a Nikon Eclipse 80i microscope and DS-Fi2 camera. Automated image analysis was performed in a blinded manner

by using ImageJ software with the color deconvolution, background subtraction, and threshold (max entropy) functions [162-164].

For immunohistochemistry, formalin-fixed paraffin-embedded sections were dewaxed and subject to epitope retrieval by heating in a pressure cooker in 10 mM tris(hydroxymethyl) aminomethane buffer containing 1 mM ethylenediamine tetraacetic acid (EDTA) with pH 9.0 for 30 min, followed by cooling at room temperature for 30 min. Endogenous peroxidases were quenched for 10 min with Bloxall (Vectorlabs), followed by blocking in 5% normal goat serum for 30 min. Slides were incubated overnight at 4 ◦C with primary rabbit monoclonal antibodies specific for F4/80 (#70076, Cell Signaling Technology, 1:500), CD44 (#37259, Cell Signaling Technology, 1:400), smooth muscle actin (SMA, #19245, Cell Signaling Technology, 1:1000), or rabbit recombinant antibody specific for CD163 (#ab182422, Abcam, 1:2000), diluted in SignalStain Antibody Dilution Buffer (Cell Signaling Technology). After washing, slides were incubated for 30 min at room temperature with horseradish peroxidase polymer-conjugated anti-rabbit antibody (Cell Signaling Technology). The detection was carried out by tyramide signal amplification as described in [165], using AlexaFluor-647 or -488 tyramide (ThermoFisher), and slides were mounted in Prolong Gold with DAPI (ThermoFisher). Fluorescent micrographs were captured from low-power fields using a Nikon Eclipse 80i microscope and Cool SnapEZ camera (Photometrics). Automated image analysis was performed in a blinded manner with ImageJ software using the Threshold (Ohtsu) function.

2.2.10 Second Harmonic Generation (SHG) Imaging

Imaging of endogenous collagen by second harmonic generation (SHG) was conducted in the

Mutliphoton Intravital and Tissue Imaging (MITI) core at UNMC using an upright Olympus FVMPE-RS microscope equipped with a Spectra-Physics InSight X3 laser and 25x (1.05 NA) objective. Images were collected from regions containing central venules using 860 nm excitation. SHG-specific emission was collected in individual images taken at 1 μm intervals throughout each 5 μm section using a 432nm (45nm bandpass) emission filter and zoom of 1.2. To optimize the visualization of collagen fiber lengths, 5 μm image stacks were compressed using NIH ImageJ (max projection) [165]. Collagen fiber counts, organization (fiber length, width, curvature), and alignment were subsequently quantified in individual SHG images (424 mm x 424 mm x 5 mm, 0.414 mm/pixel) using CT-FIRE and CurveAlign for Fibrillar Collagen Quantification [166-168]. All images and subsequent analyses were conducted by a researcher blinded to the sample conditions.

2.2.11 Statistical Analysis

The results are presented as mean ± SD or SEM. One-way ANOVA was used and followed by Tukey's multiple comparison test to analyze statistical differences among multiple groups. Differences were assessed to be significant: *$p<0.05$ was considered as a minimal level of significance, and **$p<0.01$ and ***$p<0.001$ were considered as very significantly difference. All the statistical analyses were performed with GraphPad Prism 8.

2.3. Results

2.3.1 Preparation and Characterization of miRNA Nanoparticles

Chol-PCX was synthesized as previously described [169]. We used a synthetic approach that

was designed to minimize the modification of the CXCR4-binding cyclam moieties with cholesterol by using the Boc protection of the cyclams. Thus, the cholesterol modification was primarily directed at the secondary amines of PEI (Figure 1).

The hydrodynamic size and zeta potential of Chol-PCX/miRNA nanoparticles prepared at different w/w ratios were measured using DLS. The particle size increased slightly from 60 to 80 nm with an increase in the polymer/miRNA w/w ratio (Figure 2). The zeta potential of the nanoparticles also increased slightly along with the enhanced w/w ratio.

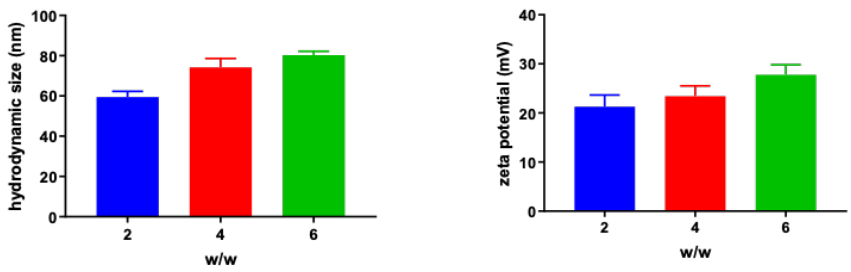

Figure 2. Characterization of Chol-PCX/anti-miR-155.

Hydrodynamic size and zeta potential of nanoparticles prepared at different Chol-PCX/miRNA w/w ratios. Data are expressed as means ± SD (n=3).

2.3.2 Cytotoxicity and Intracellular Trafficking

We next investigated the cytotoxicity of Chol-PCX in human HSC LX-2 and murine macrophage RAW 264.7 (Figure 3). We used PEI as the control polymer as it has been widely used as a non-viral nucleic acid delivery vector, but its practical application has been hindered by severe cytotoxicity [170]. In both RAW 264.7 and LX-2 cells, control PEI showed strong toxicity starting from a low concentration of 20 μg/mL. However, Chol-PCX showed lower toxicity in both cell lines. These results aligned well with our previous study showing that

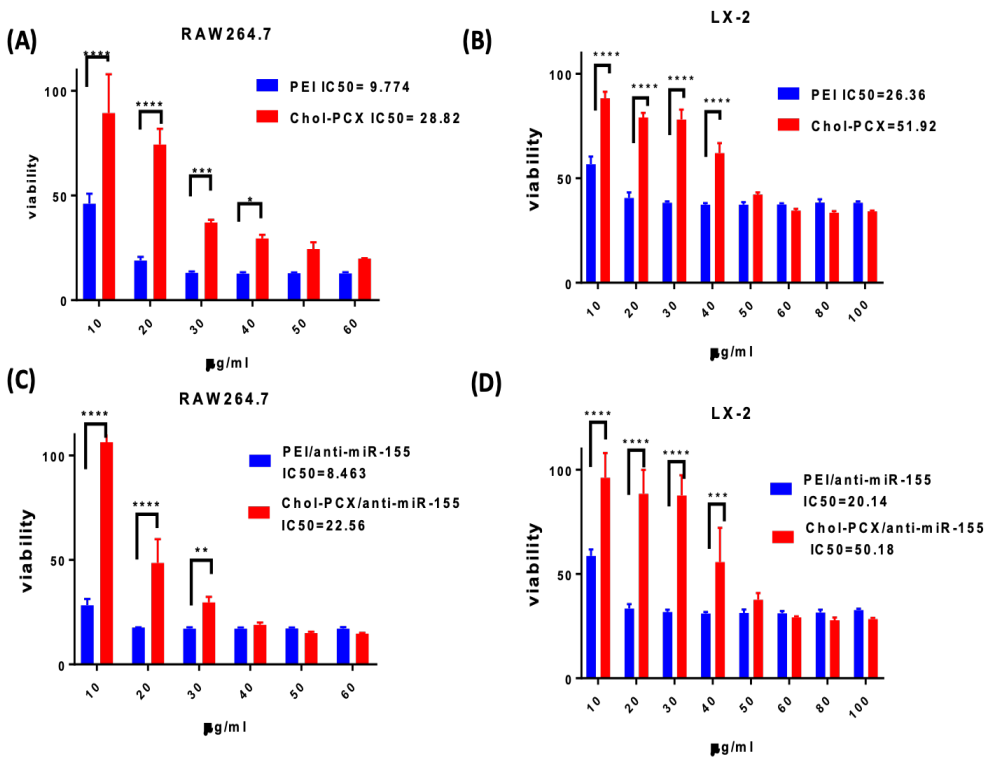

Figure 3. Cytotoxicity of Chol-PCX and Chol-PCX/anti-miR-155.
(A, B) Cell viability of the polymers after 24 h of incubation with the macrophage RAW 264.7 and HSC LX-2. (C, D) Cell viability of Chol-PCX/anti-miR-155 after 24 h of incubation with the macrophage RAW 264.7 and HSC LX-2. Data were analyzed by one-way ANOVA followed by Tukey's comparison test. Data are expressed with mean ± SD (n=3). *p<0.01, **p<0.01, ***p<0.001, and ****p<0.0001.

covalent cholesterol modification decreases the cytotoxicity of polycations [169]. Moreover, we tested the cytotoxicity of Chol-PCX/anti-miR-155 and PEI/anti-miR-155 on the RAW 264.7

and LX-2 cell lines. The results showed that encapsulation of miRNA had no significant change in the cytotoxicity of the polymers (Figure 3 C, D).

To evaluate if Chol-PCX facilitates effective intracellular uptake and trafficking for miRNA delivery, we measured cellular uptake in the macrophage cell line. We used nanoparticles prepared with fluorescently labeled FAM-RNA. Cell uptake, expressed as the % of fluorescence-positive cells, was increased from 50% to 93% as the w/w ratio of Chol-PCX/RNA increased from two to six. The uptake was comparable or higher than the control PEI (Figure 4). Nanoparticles prepared at w/w four had a relatively small size, moderately positive zeta potential, and good cellular uptake. Thus, w/w four was chosen for most subsequent in vitro and in vivo experiments.

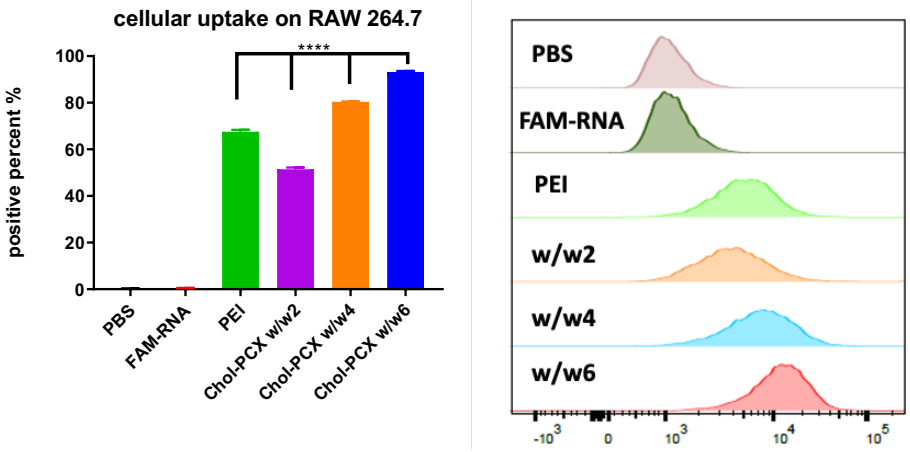

Figure 4. Cellular uptake of Chol-PCX/FITC-RNA.
Uptake of Chol-PCX/miRNA nanoparticles after 4 h of incubation with RAW 264.7 macrophages by flow cytometry (histogram on the right). Data were analyzed by one-way ANOVA followed by Tukey's comparison test. Data are expressed as mean ± SD (n=3). ****p<0.0001.

2.3.3 Chol-PCX/anti-miR-155 Nanoparticles Downregulate miR-155 Expression in Macrophages

In vitro knockdown effects of Chol-PCX/anti-miR-155 were evaluated in the RAW 264.7 cells (Figure 5). We used LPS, an endotoxin related to the pathogenesis of AALD, to activate the macrophages and induce miR-155 overexpression [15]. The cells treated with LPS showed a two-fold increase in the expression of miR-155 over the control group. Lipofectamine 2000/anti-miR-155 was used as the positive control, and it silenced 38% of miR-155 expression. Chol-PCX/anti-miR-155 outperformed the Lipofectamine 2000 control at both w/w ratios as it decreased the miR-155 expression by 59% (w/w two) and 72% (w/w four).

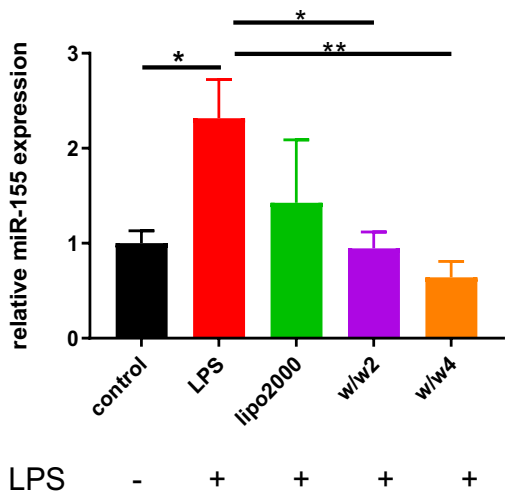

Figure 5. Transfection efficiency of Chol-PCX/anti-miR-155.
Silencing of miR-155 expression by Chol-PCX/anti-miR-155 in activated macrophages. Chol-CPX/anti-miR-155 prepared at w/w 2 and 4. Lipofectamine 2000 (lipo2000) was used as the positive control. Data were analyzed by one-way ANOVA followed by Turkey's comparison test. Data are expressed as mean ± SD (n=3). *p<0.05, **p<0.01.

2.3.4 Inhibition of CXCR4 by Chol-PCX in Vitro

The CXCR4 antagonism efficacy of Chol-PCX in vitro has been tested using a CXCR4 redistribution assay (Figure 6). This assay can be applied to track and visualize the translocation of EGFP-tagged CXCR4 receptors on the cell membrane to endosomes upon CXCL12 stimulation, which is a typical behavior for G-protein-coupled receptors. As shown in Figure 6, the CXCL12-activated cells (PBS) exhibited CXCR4 translocation, shown by higher fluorescence inside the cells, while minimal fluorescence was found on the cell membrane surface. Cells that were treated with CXCR4 antagonist AMD3100 exhibited a diffused pattern of green fluorescence, indicating the inhibition of CXCR4 translocation after SDF-1 stimulation. All the Chol-PCX demonstrated strong CXCR4 inhibition. Our results confirmed that Chol-PCX functions as a CXCR4 antagonist polymer.

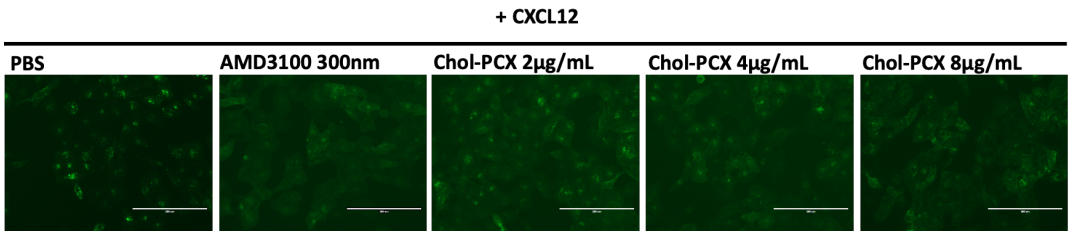

Figure 6. CXCR4 redistribution.
U2OS-overexpressing EGFP-CXCR4 cells were treated with Chol-PCX for 30 min before incubation with 10 nM CXCL12. AMD3100 (300nM) was used as the positive control (scale bar = 200μm).

2.3.5 Chol-PCX Nanoparticles Biodistribution in AALD Fibrosis Model

We investigated the biodistribution of Cy3-Chol-PCX/Cy5.5-siRNA and control Cy3-PEI/Cy5.5-siRNA by IV injection in established AALD fibrosis. The nanoparticles were

injected at the end of the model and were sacrificed after 24 h (Figure 7A). The organs were harvested and imaged using IVIS. As shown in Figure 7B and C, polymers and RNA accumulated predominantly in the liver. Chol-PCX nanoparticles had significantly enhanced accumulation in the liver compared with PEI nanoparticles.

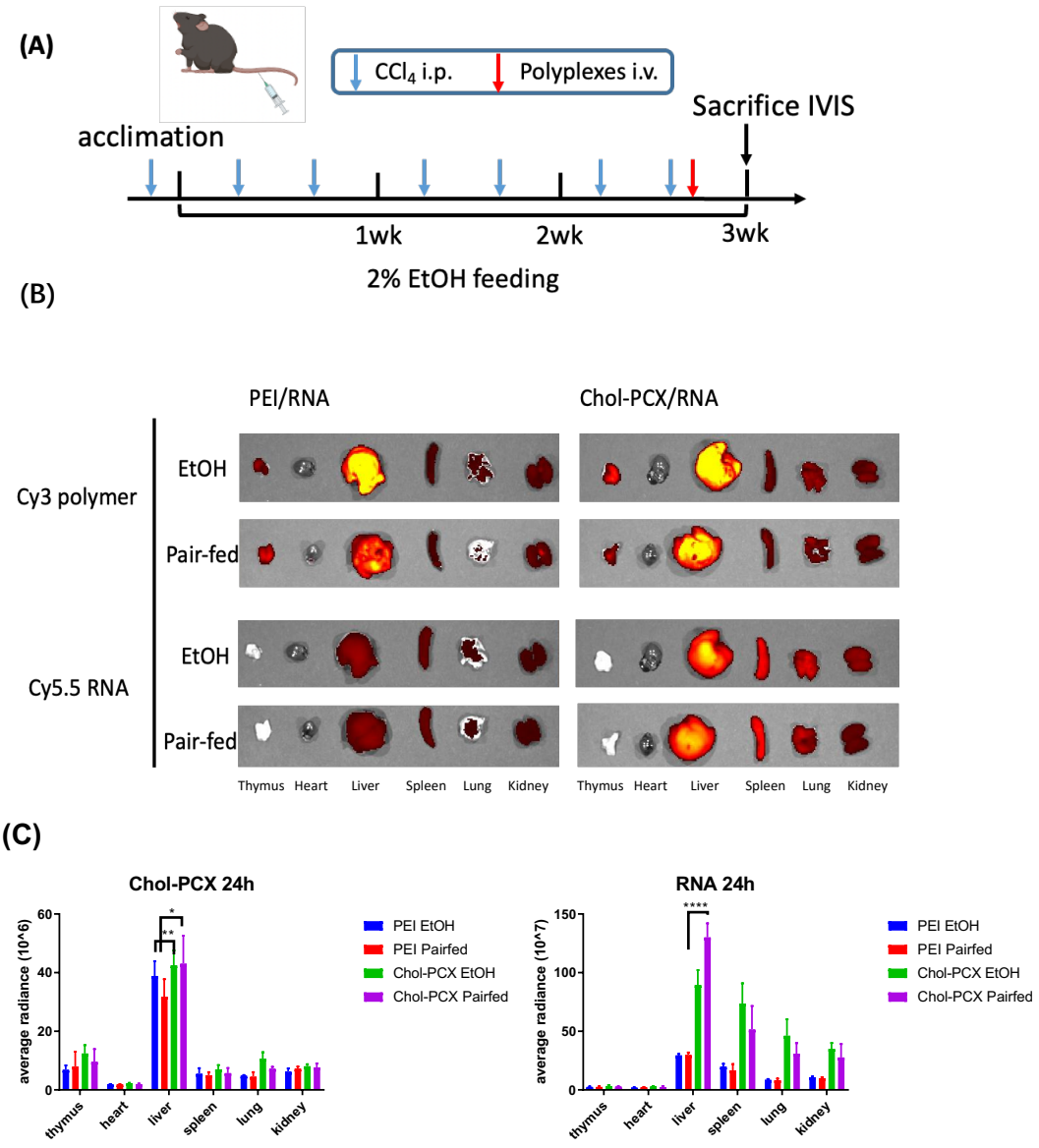

Figure 7. Biodistribution of Chol-PCX and PEI Cy5.5-siRNA nanoparticles.
(A) Mice were treated with CCl_4 for 3 weeks and fed 2% EtOH or a control diet, with the intravenous (IV) injection of the nanoparticles at the end of feeding. (B) Distribution in different organs 24 h after the IV injection of nanoparticles, and average radiance of fluorescence was quantified. Organs included thymus, heart, liver, spleen, lung, kidney. Data were analyzed by two-way ANOVA followed by Tukey's comparison test. Data are expressed as mean ± SD (n=6). *p<0.05, **p<0.01, and ****p<0.0001.

2.3.6 Chol-PCX/anti-miR-155 Treatment Ameliorates AALD Fibrosis

To establish a model of AALD fibrosis, we put the mice on a 2% EtOH LD or isocaloric (pair-fed group) diet and combined it with a secondary liver insult achieved by injection with CCl_4

for 3 weeks [161]. The feeding and treatment schedule is shown in Figure 8. We first validated that both of our therapeutic targets are upregulated in the AALD fibrosis. The hepatic gene expression of CXCR4 increased almost 2.5-fold and miR-155 was also elevated around 3-fold in the AALD fibrosis group (EtOH/CCl_4) (Figure 9A, B). This was accompanied by a 100-fold increase in collagen I (Col1a1) expression in the mice treated with CCl_4 (Figure 9C).

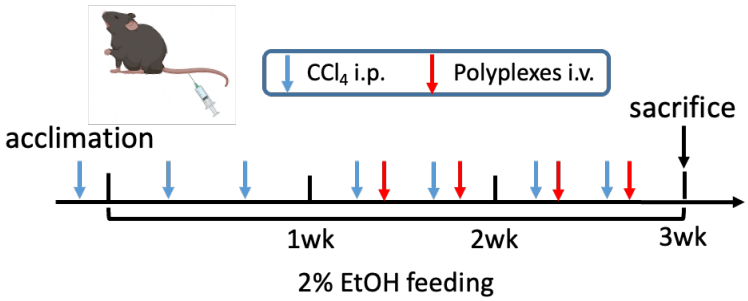

Figure 8. Experimental and treatment scheme.
Mice were treated with CCl4 for 3 weeks and fed 2% EtOH or control diet, with intravenous (i.v.) treatments twice per week for two weeks.

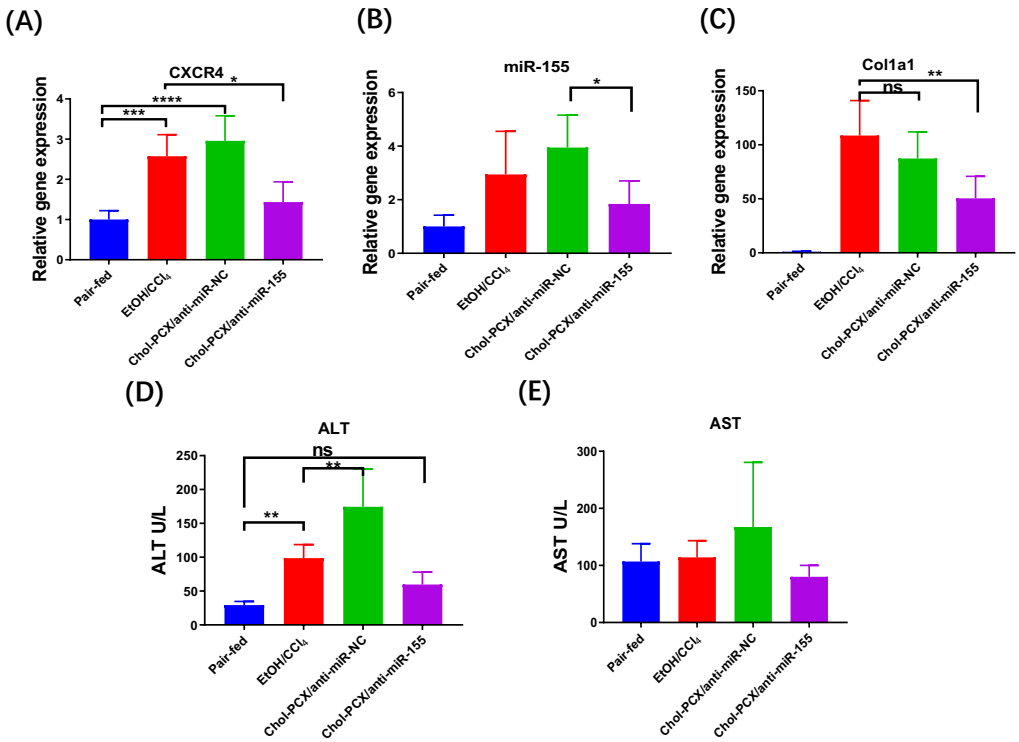

Figure 9. Hepatic CXCR4, Col1a1, and miR-155 gene expression, ALT and AST levels.
(A–C) Effect of treatment on hepatic CXCR4, Col1a1, and miR155 gene expression. (D, E) Serum ALT and AST. Data were analyzed by one-way ANOVA followed by Tukey's comparison test. Data are expressed as mean ± SD. (n = 6) * $p < 0.05$, ** $p < 0.01$, *** $p < 0.001$, **** $p < 0.0001$.

To evaluate the therapeutic efficacy, we first measured the levels of ALT and AST. ALT and AST are important biomarkers for liver injury. In AALD, EtOH usually exacerbates ALT but AST is often not changed [161]. We found that treatment with Chol-PCX/anti-miR-155 nanoparticles significantly decreased the level of ALT and slightly decreased AST when compared with the untreated AALD fibrosis group (EtOH/CCl_4 + PBS injected) (Figure 9D,E). Surprisingly, ALT was elevated significantly in the Chol-PCX/anti-miR-NC group. We then examined whether anti-miR-155 delivery reduced liver fibrosis using histological analyses. The untreated AALD fibrosis liver samples showed bridging fibrosis and fat droplets clearly visible in the H&E and MTC slides (Figure 10A). Quantification of Sirius red staining indicated that

treatment with Chol-PCX/anti-miR-155 markedly suppressed collagen deposition compared with the untreated animals and animals treated with nanoparticles containing anti-miR-NC (Figure 10B). Collagen reduction also was verified by the Col1a1 expression using RT-PCR as shown in Figure 7C. Overall, the morphological and mRNA assessments indicate that treatment with Chol-PCX/anti-miR-155 particles results in efficient silencing of miR-155 and CXCR4 antagonism in the AALD-fibrosis livers that is likely due to reduced KC-mediated signaling and HSCs activation. Chol-PCX nanoparticles containing control anti-miR-NC showed a moderate therapeutic effect on the collagen expression compared with Chol-PCX/anti-miR-155.

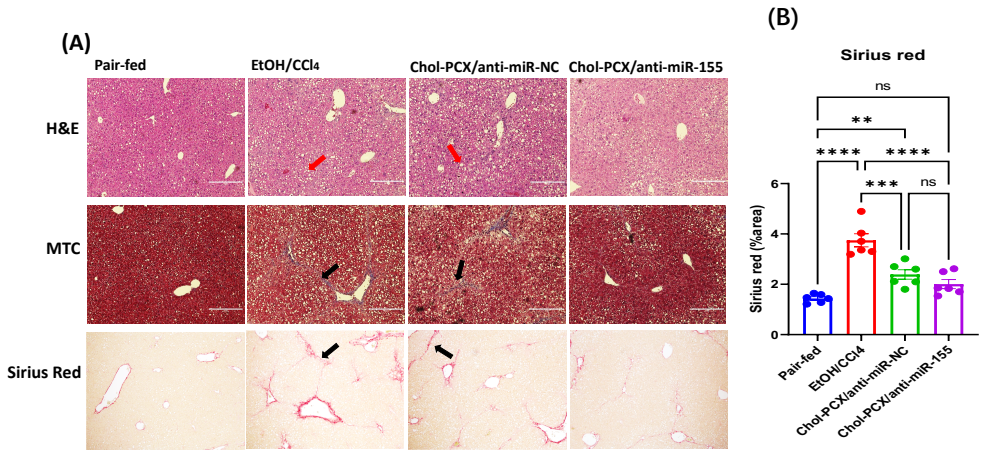

Figure 10. Therapeutic efficacy of Chol-PCX/anti-miR-155 in AALD fibrosis.
(A) Hematoxylin & eosin stain (H&E), Masson's trichrome stain (MTC) and Sirius Red staining for liver tissues in different group. Red arrows in H&E represent fat droplets, black arrows in MTC or Sirius Red represent bridging fibrosis. (B) Sirius red quantification for collagen deposition by Image J. Data were analyzed by one-way ANOVA followed by Tukey's comparison test. Data are expressed by mean ± SEM. ** $p < 0.01$, *** $p < 0.001$, **** $p < 0.0001$.

Further confirmation of the antifibrotic effects of the Chol-PCX/anti-miR-155 particles was performed using SHG microscopy to image collagen and its molecular organization [171]. AALD fibrosis has pericentral vein pattern of collagen accumulation, which can be differentiated from most chronic liver diseases where fibrosis is mainly located around portal

veins [20]. Collagen fibers were imaged at 860 nm in the untreated AALD fibrosis and animals treated with the Chol-PCX/anti-miR-155 nanoparticles (Figure 11). Images were collected from central venules in a blinded fashion. We observed decreased number of fibers and decreased fiber length in the nanoparticle group relative to the untreated group. There were no additional differences or trends in collagen fiber curvature. Standardized 50 μm square ROIs were used to calculate the average collagen fiber counts at the central vein (excluding surrounding tissue). Three independent ROIs were measured and then averaged to determine the average collagen fiber number/count and assess the alignment of those fibers relative to each other. There was no difference in the alignment, but a significantly elevated average number of collagen fibers (150 vs. 133, $p < 0.001$) and fiber length (48 vs. 46.5, $p < 0.01$) and width (3.95 vs. 3.79, $p < 0.001$) associated with the 50 μm sampling ROIs at the central vein was observed for the untreated group.

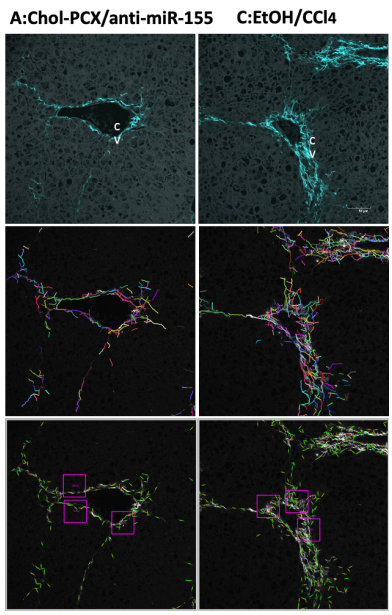

Figure 11. SHG imaging of liver collagen fibers. Representative images from central veins of liver samples with individual pseudocolored collagen fibers identified, pink squares show the 50 μm ROIs to calculate average collagen fiber counts) quantitative analyses of collagen organization and content.

2.3.7 Analysis of the Therapeutic Mechanism of Action of the Nanoparticles in AALD Fibrosis

Further analysis of the liver samples showed enhanced expression of crucial fibrosis markers, including MMPs and TIMPs that play an important role in extracellular matrix remodeling. It has been previously reported that an increase in these markers correlates with miR-155 expression in AALD, however, no changes were seen in miR-155 KO mice [15]. In our study, the mRNA expression levels of MMP-2, -9 and -13, and TIMP 1 and 2 were significantly increased in the untreated AALD fibrosis group. Treatment with Chol-PCX/anti-miR-155 particles resulted in a significant reduction in most of the analyzed fibrotic markers (Figure 12).

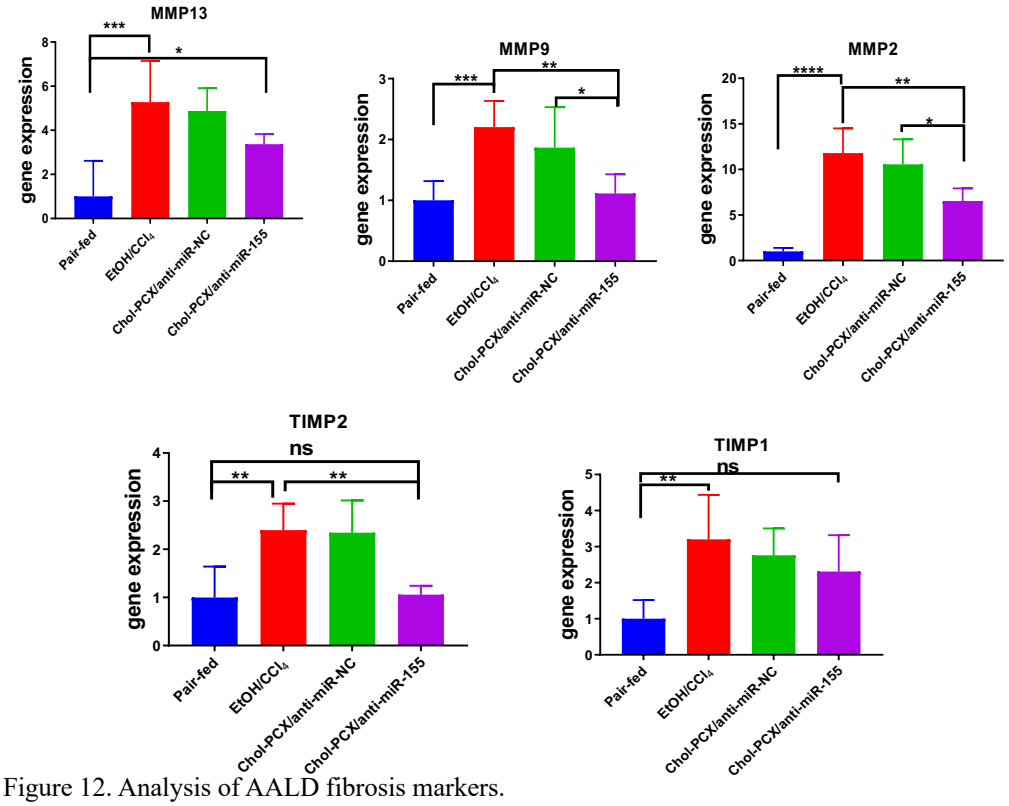

Figure 12. Analysis of AALD fibrosis markers.
MMP and TIMP expression. Data were analyzed by one-way ANOVA followed by Tukey's comparison test. Data are expressed as mean ± SD (n= 5 or 6). * $p < 0.05$, ** $p < 0.01$, *** $p < 0.001$, **** $p < 0.0001$.

Alcohol and associated metabolites can initiate hepatic inflammation that contributes to the progression of AALD. An alcohol-induced increase in profibrotic macrophage infiltration was previously observed in wild type mice compared to miR-155 KO mice [15]. In our study, we analyzed hepatic accumulation of macrophages by F4/80 immunohistochemistry. Untreated AALD fibrosis samples (EtOH/CCl_4 + PBS injected) showed a "chicken wire" pattern compared with the pair-fed group (Figure 13A). Also, the number of F4/80+ macrophages in the EtOH/CCl_4 (PBS injected) group significantly increased when compared with the pair-fed group. The number and distribution pattern of the hepatic F4/80+ macrophages in mice treated with the control anti-miR-NC particles were similar to the untreated group. However, the Chol-

PCX/anti-miR-155 group clearly had significantly reduced F4/80+ macrophage accumulation than EtOH/CCl4 (Figure 13B), to a level comparable to the pair-fed group. Therefore, there was a significant anti-inflammatory effect in Chol-PCX/anti-miR-155 treatment group compared with other groups, which contributed to the reversal of the AALD fibrosis. Moreover, the CD163+ macrophages decreased in the AALD fibrosis group, indicating decreased M2 polarization in this model. In the Chol-PCX/anti-miR-155 group, there was a slight increase of CD163+-to-F4/80+ ratio compared with the untreated group, suggesting the start of recovery of M2 polarized macrophages after treatment (Figure 13B). The observed increase in M2 macrophages does not account for the changes observed in the total macrophages. The nanoparticles are thus likely decreasing the M1 macrophages, which contributes to the total macrophages decrease in the Chol-PCX/anti-miR-155 treatment group.

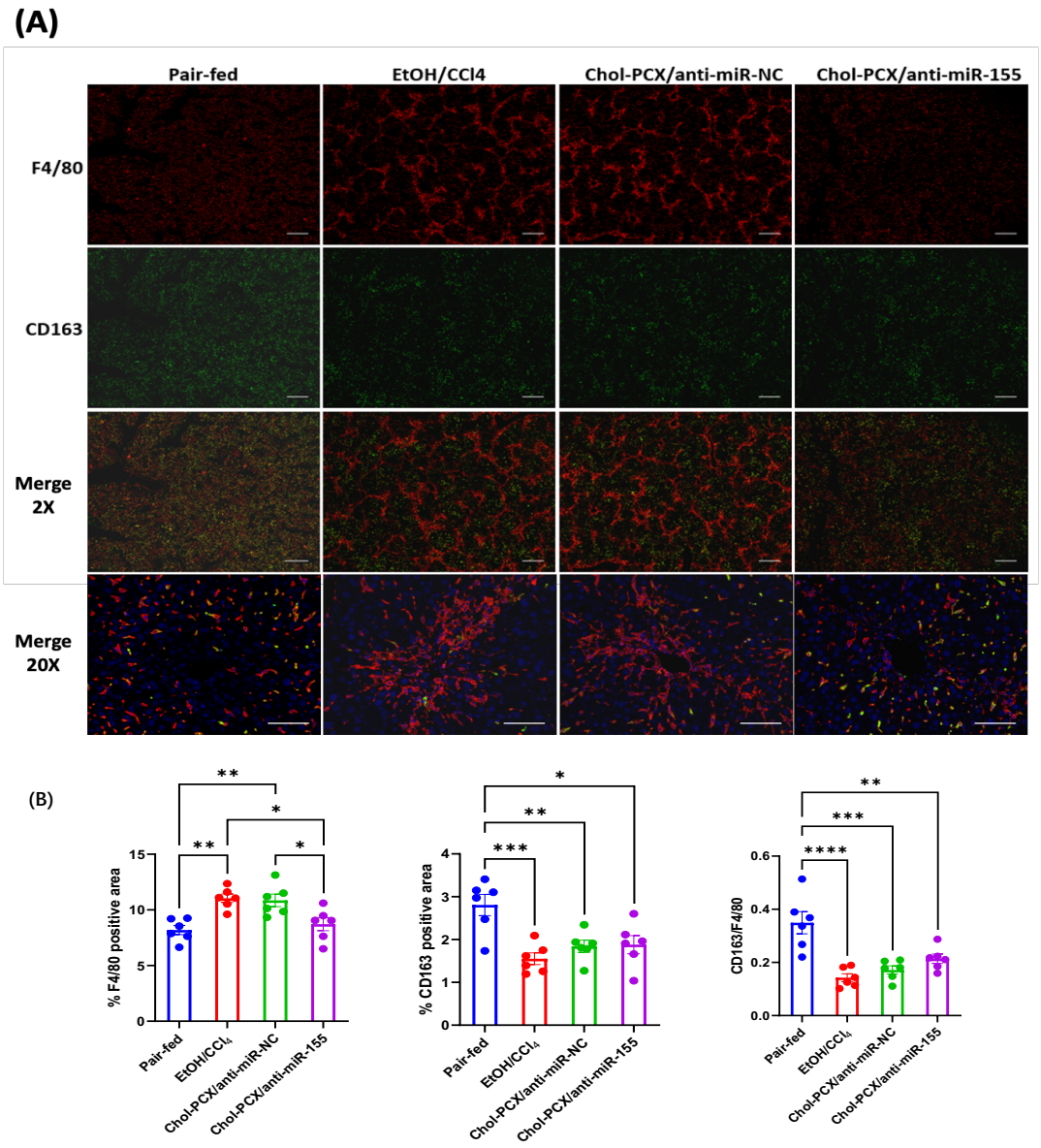

Figure 13. Immunohistochemistry for F4/80 (total macrophage or KCs stain) and CD163 (M2 phenotype).
(A) red fluorescence representing F4/80 and green fluorescence representing CD163. Scale bar: 2× (400 µm), 20× (200 µm). (B) Total macrophage content and CD163+ M2 macrophage quantification from the confocal images. Data were analyzed by one-way ANOVA followed by Tukey's comparison test. Data are expressed as mean ± SEM (n = 6) * $p < 0.05$, ** $p < 0.01$, *** $p < 0.001$, **** $p < 0.0001$.

The activation of HSCs in AALD is marked by the overexpression of CD44 receptors. CD44 is highly expressed in tumors but not very common in healthy liver. During fibrosis, however, as the HSCs proliferate this is accompanied by increased CD44 expression [72,172]. Moreover,

CD44 has high expression on aHSCs in AALD patients according to previous paper. CD44 is not only overexpressed on aHSCs, but is also expressed on LSECs and hepatocytes in disease states like hepatocellular carcinoma (HCC) [109,110]. Here, we illustrate the effect of the nanoparticle treatment on CD44 expression in the liver. α-SMA immunohistochemistry was used for staining the activated HSCs. It was shown that the untreated EtOH/CCl_4 group had significant increase in the number of activated HSCs than the pair-fed group. The activation of HSCs was markedly reduced in the Chol-PCX/anti-miR-155 treatment group (Figure 14A). CD44 expression also significantly increased in the untreated EtOH/CCl_4 group, and it was at least partly colocalized with α-SMA, confirming expression in activated HSCs. However, significant amount of CD44 expression did not overlap with α-SMA, indicating its presence also in macrophages and other immune cells. In the Chol-PCX/anti-miR-155 group, CD44 expression was significantly lowered when compared with the untreated EtOH/CCl_4 group. The percent of CD44 positive area was quantified, and the results are shown in Figure 14B. Treatment with Chol-PCX/anti-miR-155 completely reversed the increase of CD44 expression across all the cell types observed in the untreated AALD fibrosis.

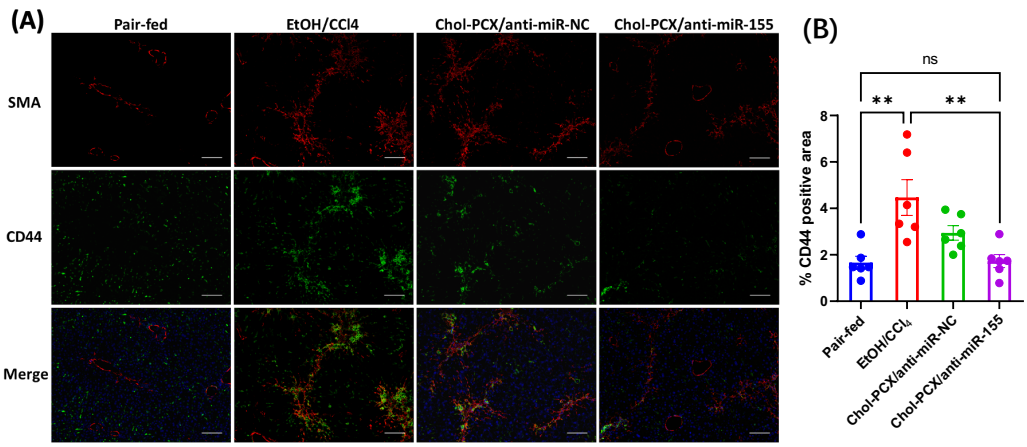

Figure 14. Immunohistochemistry for α-SMA (activated HSCs stain) and CD44.
(A) Red fluorescence representing α-SMA and green fluorescence CD44. Scale bar = 100 μm, (B) CD44-positive area quantification from the confocal images. Data were analyzed by one-way ANOVA followed by Turkey's comparison test. All data are shown as mean ± SEM (n = 6). ** $p < 0.01$.

2.4 Discussion

To test our hypothesis that CXCR4-inhibiting polymers can deliver therapeutic miRNA as a new approach to combination treatment, we synthesized Chol-PCX and evaluated its transfection efficacy in vitro and its therapeutic effects in vivo. A model of moderate alcohol consumption with secondary liver insult was established to evaluate in vivo therapeutic effects. We focused our studies on the overall efficacy of the combination treatment and on dissecting the contributions of CXCR4 inhibition and miR−155 silencing on the effectiveness of the treatment.

We first examined the role of CXCR4 inhibition. Non-parenchymal liver cells are crucial players in AALD fibrogenesis. HSCs differentiate and proliferate into activated HSCs, while KCs secrete proinflammatory cytokines. These two cell types communicate with other hepatic cells to accelerate the progression of fibrosis [95]. Inhibition of the CXCR4 axis in activated

HSCs has been previously used successfully in the treatment of liver fibrosis [135,173]. However, there are also studies suggesting that the effect of CXCR4 inhibition depends on the degree of liver injury. For example, in an acute liver injury and early chronic liver fibrosis model, mice treated with a CXCR4 antagonist AMD3100 expressed higher hepatic α-SMA and showed increased hepatic collagen content and fibrosis over untreated controls. This suggested that CXCR4 inhibition worsens the hepatic injury in the early stage disease [174]. The CXCR4 ligand CXCL12 was previously shown to have a potentially protective role during hepatic fibrosis through expansion of hepatic progenitor and oval cells [175], which are beneficial for the liver regeneration. HSCs were activated and the number of circulating neutrophils increased in liver in mice receiving AMD3100 at the onset of liver injury [176]. Our study confirms the complex role of CXCR4 in early stages of AALD fibrosis. On one hand, CXCR4 inhibition alone (animals treated with Chol−PCX/anti-miR-NC) decreased hepatic collagen content (Figure 10B, $p = 0.0003$) but there was no effect on the α-SMA expression observed in other studies with similar polymers. On the other hand, liver injury marker ALT was elevated in animals treated with the CXCR4 inhibition alone. Our results are consistent with the previous studies of liver fibrosis and expand them to AALD to suggest similarly complex effects of CXCR4 inhibition in the AALD fibrosis liver microenvironment.

In contrast to CXCR4, miR-155 proved to be valid therapeutic target in AALD fibrosis. miR−155 was strongly upregulated in the AALD livers and its silencing with the Chol−PCX/anti-miR-155 nanoparticles resulted in overall therapeutic benefit. We have observed multiple effects of the miR−155 silencing, including a decrease in the hepatic expression of CXCR4 and CD44. To explain this finding, we have to look into the initial stages

of the liver injury, when KCs trigger the recruitment of additional immune cells. During AALD pathogenesis, LPS binds to CD14/TLR4 on KCs causing nuclear factor kappa beta (NF-κB) activation, which in turn leads to KC secretion of a series of cytokines and chemokines, such as transforming growth factor-β (TGF-β), and tumor necrosis factor-α (TNF-α) [177]. The inflammatory factor TGF-β is one of the most widely recognized and powerful profibrogenic mediators and promotes the accumulation of ECMs by HSCs [133]. The cytokines released by activated KCs damage hepatocytes and induce HSC activation [178]. Downregulation of miR-155 contributes to HSC activation by regulating the EMT process and the ERK1 pathway [179]. CXCL12/CXCR4 is also known to activate the ERK1/2 cascade to induce the proliferation of HSCs in liver fibrosis [133]. We believe that there is a communication between HSCs and KCs that is partly regulated by miR-155 and CXCR4 and which participates in the regulation of overlapping pathways during the progression and reversal of AALD fibrosis. Treatment with the Chol−PCX/anti−miR−155 nanoparticles reduce a series of inflammatory factors from the activated KCs, causing reduced activation of HSCs and CXCR4 and CD44 expression. This is further supported by our finding that the inflammatory F4/80+ macrophages were significantly reduced in the treated group, while the CD163+ M2 macrophages were increased as a result of the treatment.

Chapter 3. Targeted delivery of nucleic acids using hyaluronic acid coated nanoparticles to activated HSCs in AALD

3.1 Introduction

The crosstalk between hepatic cells is of vital importance for the pathogenesis of alcoholic liver fibrosis. Ethanol is mainly metabolized in hepatocytes to acetaldehyde which contributes to lipid synthesis and steatosis formation. ROS produced by apoptotic hepatocytes and the LPS from the alcohol-related compromised gut activate KCs to secrete pro-inflammatory cytokines or chemokines, giving rise to the activation of HSCs. HSC-targeted delivery bears great potential for the reversion of fibrosis since HSCs are the main cell type responsible for the extracellular matrix deposition. Most of the targeting delivery systems for liver fibrosis are focused on how to increase the specificity of cargos to HSCs, such as, vitamin A-RBP, M6P-BSA/M6P receptor.

Hyaluronic acid (HA) is a glycosaminoglycan and main component of extracellular matrix produced by HSCs. As an endogenous substance, HA is considered a biodegradable, biocompatible, non-immunogenic and non-toxic biomaterial. HA hydrogels or nanocarriers are usually developed to specifically target CD44 overexpressed on tumors [180]. CD44 receptors are not very common in healthy liver. However, CD44 overexpression on activated HSCs was validated on alcoholic liver patients and CCl_4 induced fibrotic rodents [172,181]. CD44 is also expressed on other liver cells, including LSECs and hepatocytes after injury and during regeneration [109,110].

CXCR4/CXCL12 axis plays pivotal roles on alcoholic liver fibrosis, CXCR4 expression is elevated on aHSCs during the progression of alcoholic liver fibrosis. CXCR4 antagonists conjugated to polycations are proven useful for delivery of nucleic acids to liver fibrosis as shown in the previous chapter 2. To further enhance the specificity to aHSCs, CXCR4 ligand binding could be used to allow for more nucleic acids delivery to the diseased alcoholic liver.

Most of the nanoparticles in systemic circulation undergo opsonization and are taken up by reticuloendothelial system (RES)/mononuclear phagocyte systems (MPS), mainly composed of KCs with phagocytosis function and LSECs with endocytosis function. KCs and LSECs are main inflammation related cell types which are activated and involved in the progression of liver fibrosis. Due to the structure of hepatic triads where hepatocytes and HSCs are separated from the bloodstream by a layer of LSECs, the exposure of nanoparticles to the different hepatic cells is not homogeneous. Especially in the fibrotic liver, the fenestration size of LSECs layer size (50-200nm) changes based on the disease states. NPs with size > 200nm are difficult to pass through the fenestrate and tend to stay within the sinusoid where they are easily taken up by MPS (KCs and LSECs). NPs around 150 to 200 nm in size are small enough to pass through the diseased sinusoidal fenestrae.

To overcome the uptake of NPs by RES and increase taken up by HSCs, we designed a nanocarrier system having two targeting ligands for activated HSCs. That is, HA-cyclam coated nanoparticles bind to CD44 and CXCR4 receptors simultaneously in the liver, both of receptors being highly expressed on aHSCs in alcoholic liver fibrosis. Moreover, nanoparticles were formulated with size around 100 nm enabling them to pass through the diseased liver fenestrae

and target aHSCs. This carrier can enhance the selective uptake of nucleic acids by aHSCs while keeping some uptake efficiency for KCs to exert a dual cell targeting function.

3.2 Materials and Methods

3.2.1 Synthesis of Hyaluronic acid-Cyclam polymer (HA-C)

The HA-C was synthesized by an alkylation reaction between cyclam derivate and HA. The typical conjugation procedure is described as follows. First, the cyclam derivative α-cyclam-p-toluic acid (CPTA) was synthesized follow a previous paper [182], then the CPTA (product 2) was conjugated with *tert*-butyl (aminomethyl) carbamate. CPTA (1equiv) was added into a 100mL reaction flask and dissolved in water, CDMT (1equiv) was separately dissolved in acetonitrile and added into the flask, the final ratio of water/acetonitrile volume is 3/2, then followed by addition of *N*-methylmorpholine (1.5 equiv). After 1h, tert-butyl (aminomethyl) carbamate was added into the reaction mixture stirring for overnight in the ice bath to form tert-butyl ((4-((1,4,8,11-tetraazacyclotetradecan-1-yl)methyl)benzamido)methyl) carbamate (product 3). Then the product 3 was under de-boc protection by 1M HCl for overnight. The sodium hyaluronate dissolved in water (10mg/mL) was added into the reaction mixture and stirring for overnight. The final product was purified by dialysis (cellulose acetate, 3.5 kDa molecular weight cut-off) against water over 4 days. Afterwards, the product is lyophilized and characterized by ^{1}H NMR.

3.2.2 Preparation and Characterization of HA-C Nanoparticles

To formulate HA-C nanoparticles, polycation (PEI-Cholesterol) complex with different small

RNA (scramble siRNA, anti-miR-NC or miR-34a) were used in this study to form polyplex as the inner core first, then coated with HA-C to form HA-C nanoparticles. Polyplexes were formulated first by mixing equal volumes of RNA and polycation (10nM HEPES, pH7.4) to achieve the desired polymer/RNA w/w ratios. The RNA condensation ability of polycations was evaluated by agarose gel electrophoresis assay, polyplexes were prepared at different w/w ratios and loaded to a 2% agarose gel (0.5 μg/mL SYBR), followed by running at 100 V in 0.5 × Tris/Borate/EDTA buffer for 15 min. Then, the gel was imaged with E-Gel Imager (Life Technologies, CA) under UV. The hydrodynamic particle size and zeta potential were measured by dynamic light scattering (DLS) at 25 ◦C using a Malvern NANO ZS (Cambridge, UK). Then the HA-C NPs were formulated by coating a mixture of HA-C and HA polymer, the (HA-C + HA)/polycation w/w4 was used to coat on the polyplexes with different w/w ratios. Different formulations of HA-C NPs were tested by DLS.

Heparin replacement assay was used to test the dissociation of RNA from HA-C NPs. Polyplexes and HA-C NPs were incubated with different concentration of Heparin for 30min, then loaded to a 2% agarose gel (0.5 μg/mL SYBR), followed by running at 100 V in 0.5 × Tris/Borate/EDTA buffer for 15 min. After running, the gel was imaged with E-Gel Imager under UV.

3.2.3 CXCR4 antagonism Assay

The CXCR4 antagonism efficacy of HA-C was determined by a CXCR4 redistribution assay. Human epithelial osteosarcoma U2OS cells with EGFP-CXCR4 fusion protein (Fisher Scientific Waltham, MA, USA) were cultured in DMEM supplemented with 2 × 10−3 M L-

glutamine, penicillin (100 U/mL), streptomycin (100 μg/mL), G418 (0.5 mg/mL), and 10% FBS. The cells (8000 cells/well) were seeded in black 96-well microplates. After 24 h, the cells were washed with an assay buffer and treated with different concentrations of HA-C or HA for 30 min. The CXCR4 antagonist AMD3100 (300 nM) was used as a positive control. Then CXCL12 (10 nM) was added and incubated for 1 h. Cells were fixed and 20x images were visualized and collected using EVOS xl microscopy under the GFP channel. To calculate EC_{50}, Cellomics ArrayScan VTI High Content Analysis Reader (Thermo Scientific) and SpotDetectorV3 software were used to analyze the internalized EGFP-tagged CXCR4 receptors. The relative CXCR4 antagonism was calculated by setting AMD3100 (0.15 μg/mL) as 100% antagonism and CXCL12 only group as 0%. EC_{50} then was calculated from the dose-response curve in GraphPad software.

3.2.4 Cell Viability and Intracellular Trafficking

Primary mouse HSC cells (mpHSC) were isolated by liver perfusion [183]. mpHSC were cultured under 5% CO2 in DMEM supplemented with 10% FBS and 1% Pen-Strep at 37◦C. Murine RAW 264.7 macrophages (ATCC, Manassas, VA, USA) were cultured under 5% CO2 in DMEM supplemented with 10% FBS and 1% Pen-Strep at 37◦C. When confluency reached 80-90%, the mpHSCs cells were trypsinized and subcultured. The RAW 264.7 cells were scraped to dislodge and subcultured.

Cell viability was evaluated by a CellTiterBlue assay following the manufacturer's protocol (Promega Corp. Madison, WI, USA). In brief, 8000 cells/well were seeded in a 96-well plate and cultured for 20–24 h. A series of increasing concentrations of the polymers and

nanoparticles were added, and the plates were incubated at 37 ◦C for 24 h. Cell viability was normalized to cells incubated with PBS by measuring the absorbance at 560Ex/590Em nm using a SpectraMax iD3 Multi-Mode Microplate Reader.

For uptake evaluation, the cells (15,000 cells/well) were seeded in 12-well plates and cultured to 60% confluency. The cells were incubated with the nanoparticles containing fluorescently labeled FAM-miRNA (100 nM) for 12 h. Cellular uptake was measured in trypsinized cells using a BD FACS LSR II Green flow cytometer.

3.2.5 In Vitro miRNA Transfection

Mouse primary HSCs (2×10^5 cells/well) were seeded in 6-well plates and cultured to 60% confluency. The cells were incubated with the HA-C NPs (100 nM of miR-34a) for 6 h in a serum-free medium, then removing the nanoparticle solutions followed by stimulation with TGFβ (5 ng/mL) for 48 h. The RNA was extracted using RNAlater (Qiagen, Valencia, CA, USA). The mRNA expression of fibrotic markers was analyzed by SYBR Green RT-PCR. Extracted RNA (2 μg) was converted into cDNA using a High-Capacity cDNA Transcription Kit (Applied Biosystems, Waltham, MA, USA). The PCR reactions were run on Rotor-Gene Q (QIAGEN) equipment with iTaq Universal SYBR Green Supermix (Bio- Rad, Hercules, CA, USA) and GAPDH as a housekeeping gene. Relative mRNA levels were calculated based on the comparative threshold value (Ct) method. The primers used for Col1a1: FM1_Col1a1: CGTATVACCAAACTCAGAAG, RM1_Col1a1: GAAGCAAAGTTTCCTCCAAG.

3.2.6 Biodistribution of HA-C NP in Alcoholic fibrosis

All animal experiments were performed in C57BL/6J female mice purchased from Jackson Laboratories and following the protocol approved by the University of Nebraska Medical Center Institutional Animal Care and Use Committee. An AALD fibrosis model was established by feeding the mice an EtOH-containing Lieber-DeCarli (LD) daily liquid diet (Dyets Ins., Bethlehem, PA, USA) combined with repeated intraperitoneal injection of CCl_4 for 3 weeks. In brief, on day 0 mice were started on 1% (v/v) EtOH LD liquid diet or control isocaloric liquid diet without EtOH for two days. Starting on day 3, the mice were injected twice per week with CCl_4 (1mL/kg of 10% CCl4 in olive oil) and fed with 2% EtOH LD liquid diet or the control isocaloric diet. The daily intake of the EtOH mice was monitored, and the following day the equivalent calories were administered to control mice. At the end of the animal model, both the EtOH mice and Pair-fed mice were injected intravenously with 200μL of fluorescently labeled HA-C NPs/Cy5.5-siRNA (1mg/kg Cy5.5-siRNA). Mice were sacrificed 24 h post-injection, and major organs were harvested for imaging by Xenogen IVIS 200.

3.2.7 Biodistribution on cellular level

Flow cytometric analysis of tissue leukocytes and non-parenchymal cells were performed. Briefly, liver tissues were digested with collagenase type-IV (Worthington) at 37◦C with collagenase solution for 40min. Extracts were filtered using 40μm cell strainers and parenchymal cells were removed by sedimentation for 45 min at 4◦C followed by centrifugation for 5 min at 15g (method modified from previous paper) [184]. The remaining non-parenchymal cell mixture was subjected to red blood cell lysis and washed by PBS using centrifugation for

5 min at 300g. Then the cell pellets were stained by unconjugated anti-CD16/32 (Fc block, BD), and followed by staining with fluorochrome-conjugated cell surface antibodies in cell staining buffer (Biolegend®). After 30min incubation, unbound antibody was washed with PBS. Then the cells were fixed in fixation buffer (Biolegend®) in the dark for 20 min at room temperature, centrifuged cells at 350×g for 5min, supernatant was discarded and cells were washed with PBS. After fixation, cells were permeabilized with 1× intracellular staining perm wash buffer (Biolegend®) and washed with PBS twice. Intracellular staining was performed by resuspending fixed/permeabilized cells in intracellular antibodies solutions (e.g. α-SMA) for 30min, then wash with PBS. The fluorescence antibodies including, Alexa fluor 594-CD11b (Biolegend®), PE-Cy7-F4/80, (Biolegend®) Alexa fluor-647 Ly6G (Biolegend®), APC-Cy7-CD31 (Biolegend®), Pacific blue-CD45 (Biolegend®), PE-Ly6C (Biolegend®), Alexa fluor 488-α-SMA (Invitrogen, US) [185]. Flow cytometry were performed using a BD FACS LSR II Green flow cytometer. Data were analyzed using FlowJo. The Median fluorescence of nanoparticle fluorescence in alcoholic liver ($EtOH/CCl_4$) or control liver (Pair-fed) were compared in each cell type.

3.2.8 Statistical Analysis

The results are prepared as mean ± SD or SEM. Significance difference between two groups were determined by student's t-test. One-way ANOVA was used and followed by Tukey's multiple comparison test to analyze statistical differences among multiple groups. Differences were assessed to be significant: *$p<0.05$ was considered as a minimal level of significance, and **$p<0.01$ and ***$p<0.001$ were considered as very significantly different. All the statistical

analyses were performed with GraphPad Prism 8.

3.3 Results and Discussion

3.3.1 aHSCs – Main cell type for liver fibrosis targeting

Liver is composed of parenchymal cell hepatocytes and non-parenchymal cells, including HSCs, LSECs and KCs. The favorable liver tropism of nanomedicines is mainly attributed to the MPS uptake, namely, phagocytosis by KCs and compensated taken up by LSECs through endocytosis. To target aHSCs, innovative nanomedicines with specific ligand-receptor interactions for aHSCs are needed. In our previous study, we took advantage of CXCR4 overexpressed on aHSCs and used CXCR4 antagonist cyclam as a targeting ligand to improve delivery efficiency for nucleic acids [74]. Here, in this study, we explored the CD44 overexpression on the alcoholic liver (Figure 15B) by quantification of CD44 positive fluorescence showed in Chapter 2, immunofluorescence staining for CD44 and α-SMA partially overlapped in alcoholic mice liver, indicating the aHSCs expressed higher level of CD44 compared with control liver (Figure 15A).

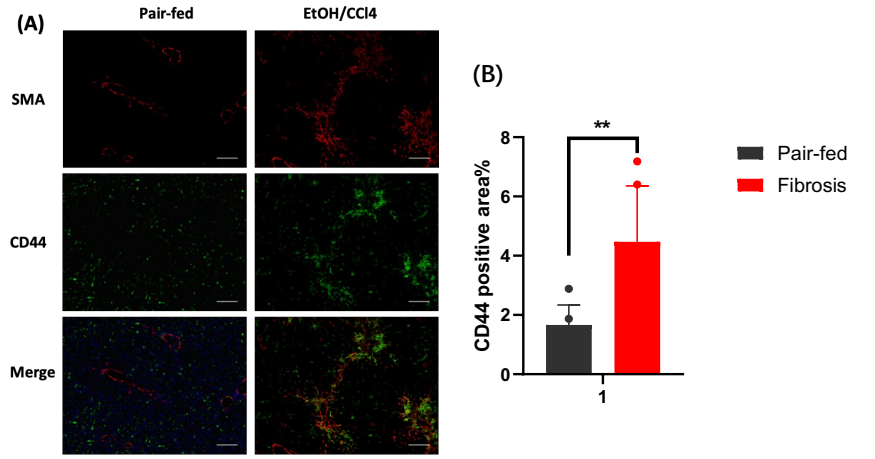

Figure 15. Immunohistochemistry for α-SMA (activated HSC stain) and CD44, which is a subset of that shown in Fig 14.
(A) Red fluorescence representing α-SMA and green fluorescence CD44. Scale bar = 100 μm, (B) CD44-positive area quantification from the confocal images. Data was analyzed by unpaired t-test. All data are shown as mean ± SEM (n = 6). ** $p < 0.01$.

3.3.2 Synthesis and characterization of HA-C polymer

Based on the increase of CD44 and CXCR4 on aHSCs, we designed the HA-C polymer (Figure 16), cyclam serves as CXCR4 targeting ligand and HA targets CD44. HA is a linear glycosaminoglycan polymer which composed of repeating polymeric disaccharides of D-glucuronic acid (GlcUA) and *N*-acetyl-glucosamine (GlcNAC). The HA-C was successfully synthesized by an alkylation reaction between the cyclam derivate (CPTA) and HA. The typical conjugation procedure is described as follows. First, the cyclam derivative α-cyclam-p-toluic acid (CPTA) was synthesized as described [182], then the CPTA (product 2) was conjugated with *tert*-butyl (aminomethyl) carbamate to form product 3 (Figure 16). Then the product 3 was under de-boc protection by 1M HCl for overnight. The sodium hyaluronate dissolved in water (10mg/mL) was added into the reaction mixture and stirred overnight followed by dialysis and lyophilization. The structure of HA-C was verified by ^{1}H NMR (Figure 17), the successful

conjugation of cyclam on HA was verified by the signal of protons on the phenylene ring (δ

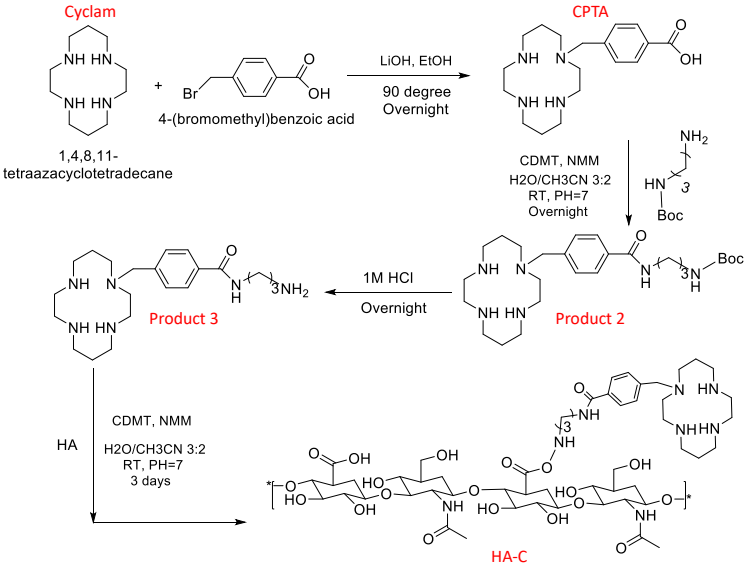

Figure 17. Synthesis scheme for HA-C.

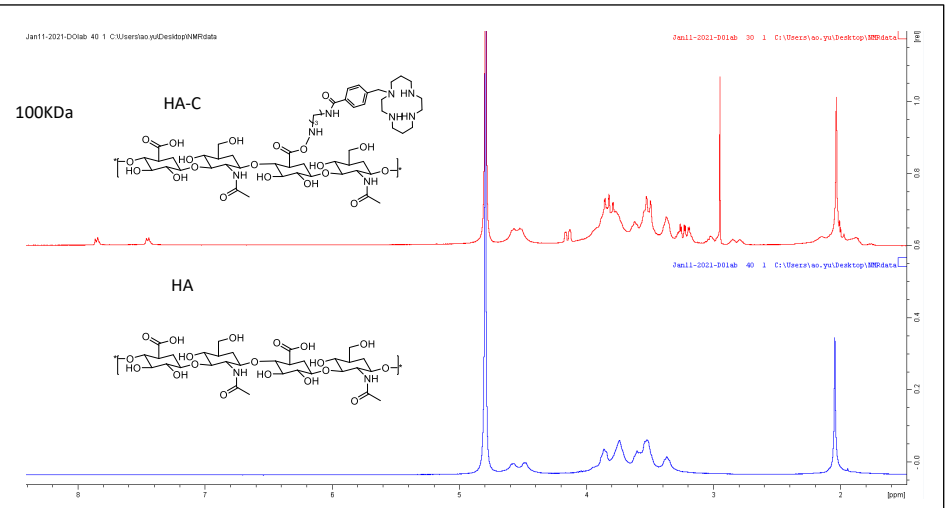

Figure 16. NMR of HA and HA-C.

6.7–7.6) in HA-C polymer which did not show in HA.

3.3.3 CXCR4 antagonism of HA-C

The CXCR4 antagonism efficacy of HA-C in vitro was tested using a CXCR4 redistribution assay (Figure 18B). This assay can be applied to track and visualize the translocation of EGFP-

tagged CXCR4 receptors on the cell membrane to endosomes upon CXCL12 stimulation, which is a typical behavior for G-protein-coupled receptors. As shown in Figure 18B, the CXCL12-activated cells (PBS) exhibited CXCR4 translocation, shown by higher fluorescence inside the cells, while minimal fluorescence was found on the cell membrane surface. Cells that were treated with CXCR4 antagonist AMD3100 exhibited a diffused pattern of green fluorescence, indicating the inhibition of CXCR4 translocation after CXCL12 stimulation. HA-C also shows similar diffused pattern of green fluorescence, which demonstrated strong CXCR4 inhibition.

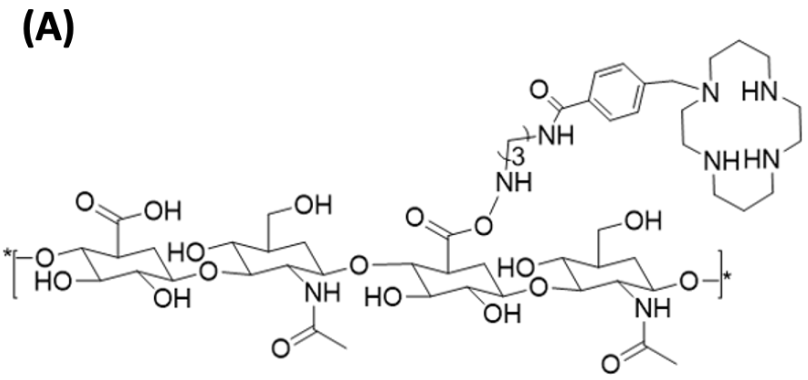

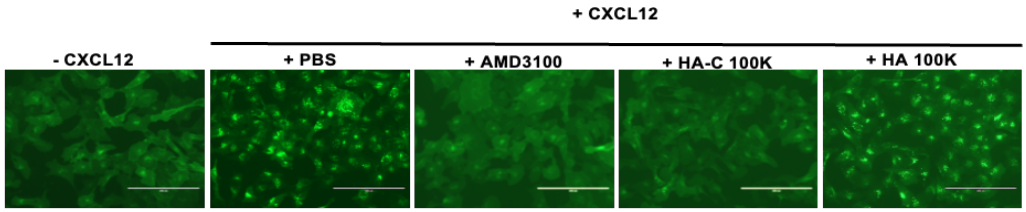

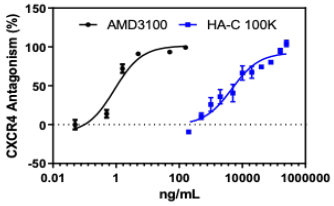

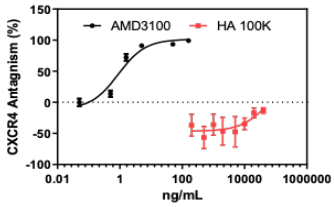

Compound	CXCR4 Antagonism (EC50, ug/mL)	CXCR4 Antagonism (EC50, uM)
AMD3100	0.005	0.01
HA-C 100K	4.7	0.05
HA 100K	-	-

Figure 18. HA-C polymer and CXCR4 antagonism.
(A) HA-C structure. (B) CXCR4 redistribution assay. U2OS-overexpressing EGFP-CXCR4 cells were treated with HA for 30 min before incubation with 10nM CXCL12. AMD3100 (300 nM) was sued as the positive control (scale bar = 200μm) (n=3).

3.3.4 Preparation and characterization of HA-C NPs

Then we formulated HA-C NPs by preparing the polyplexes first then camouflaged polyplexes with HA-C polymer. Polycation was physically complexed with siRNA at different w/w ratios,

polyplexes were formed and siRNA was condensed starting from w/w 2 as illustrated in Figure 19A using electrophoresis. Particles prepared at w/w 2 showed large sizes which are around 400nm. The hydrodynamic size of different w/w ratios showed that starting from w/w 3.5, relatively small particles around 60 nm are formed. Then we formulated HA-C NPs by coating HA-C on the polyplexes by their electrostatic interactions between negatively charged HA and positively charged polyplexes. Mixture of HA and HA-C was used and coated onto polyplexes with different w/w ratios. In the HA-C solutions. We adjusted HA-C/HA ratios to get the smallest size. Figure 19B shows the HA-C/HA at 30% achieved the size below 100 nm, which is suitable for passing through the LSEC fenestrae. Therefore, we chose polyplexes at w/w 5 and HA-C content 30% for further use. In Figure 19B, it is shown that as the HA-C content increases, the zeta potential decreases and presents negative charge on the surface.

The presence of serum makes the polyplexes unstable and facing the problem of dissociation in blood stream before arriving at target sites. The stability of the HA-C NPs against dissociation in a heparin displacement assay was tested, the polyplexes without HA-C coating were used as the control group (Figure 19C). As the heparin concentration increase, siRNA started to dissociate from 80 μg /ml, however, HA-C NPs did not dissociate even at very high concentration of heparin 300 μg/ml, suggesting the high stability of HA-C NPs.

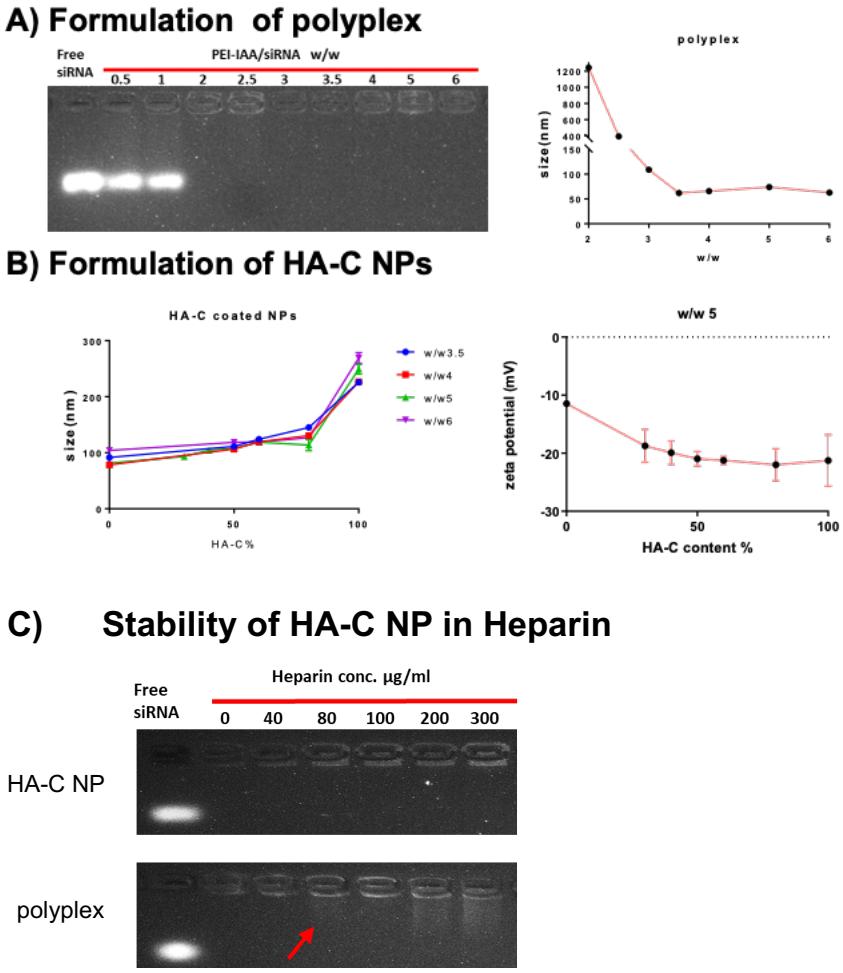

Figure 19. HA-C NP formulation.
(A) polycation/siRNA polyplexes at different w/w ratios, siRNA condensation ability of polyplexes by electrophoresis. Size tested by DLS. (B) Formulation of HA-C NPs. Size and zeta potential of NPs. (C) Heparin replacement assay for stability of HA-C NP. Arrow shows the dissociation. Data are expressed as means ± SD (n=3).

3.3.5 Cytotoxicity and cellular uptake of HA-C NPs/miRNA in hepatic cells

Safety of nanoparticles is the basis for their usage in animals or even future in humans. Thereafter, we evaluated the biocompatibility of HA-C NPs in different hepatic cells. Macrophage Raw 264.7 cell line, LX-2 (human HSCs) and mpHSC (mouse primary HSCs) were leveraged to test the toxicity of HA-C NPs. As shown in Figure 20, HA-C NPs showed

no toxicity in all three cell lines. In contrast, the polyplexes without camouflage exhibited around 5-10% toxicity at high concentrations in each cell types.

The main purpose of the study is to elevate the cellular uptake efficiency to HSCs. We then measured if HA-C coating provide any higher uptake. After incubation for 12 h with HSCs, the cellular uptake efficiency of HA-C NPs was significantly higher than the polyplexes without HA-C coating (Figure 21), suggesting the HA-C NP selective targeting to HSC. That means our HA-C equipped the NPs with more efficient cellular uptake.

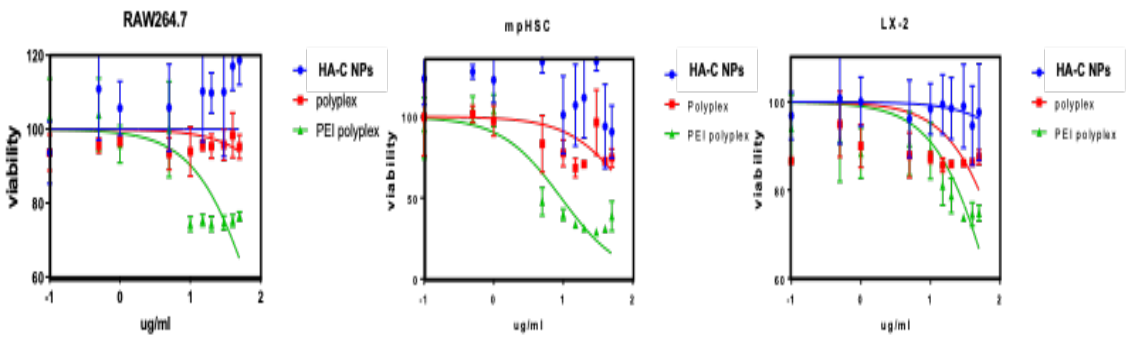

Figure 20. Cytotoxicity of HA-C NPs on hepatic cells.
Raw 264.7, mpHSCs, and LX-2 cell lines were used to test cytotoxicity of HA-C NPs. HA-C NPs showed almost no toxicity on different cells compared to polyplex without HA-C coating and PEI control polyplex (n=3). Statistical significance was evaluated using two-way ANOVA, Data are representative of three experiments ± SD. Comparison between HA-C NPs and polyplex, and comparison between HA-C NPs and PEI polyplex were significant ****p< 0.0001.

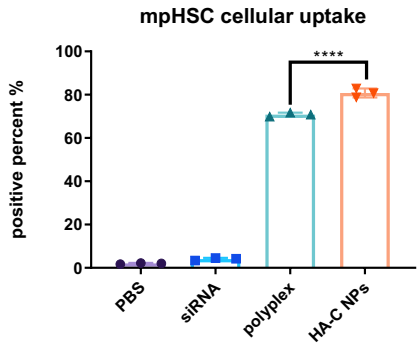

Figure 21. Cellular uptake of HA-C NPs in mpHSC.
Data were analyzed by one-way ANOVA followed by Turkey's comparison test. Data are expressed as mean ± SD (n=3). ****p<0.0001.

3.3.6 Efficacy of HA-C NPs/miRNA transfection

We aimed to use this nanosystem targeting aHSCs in the pathogenesis of AALD. The progression of AALD and fibrogenesis are attributable to the activation of HSCs. Many gene targets are involved in this process that occur in aHSCs. Therefore, we chose microRNA therapy selectively targeting aHSCs. MiR-34a is downregulated in liver fibrosis and is correlated with the elevation of collagen level in activated HSCs. In this part, the TGFβ was used to activate mpHSCs to have an increased mRNA level of Col1a1. The delivery of miR-34a by HA-C NPs successfully downregulated the Collagen I mRNA expression, indicating the efficient miR-34a delivery efficiency of HA-C NP (Figure 22).

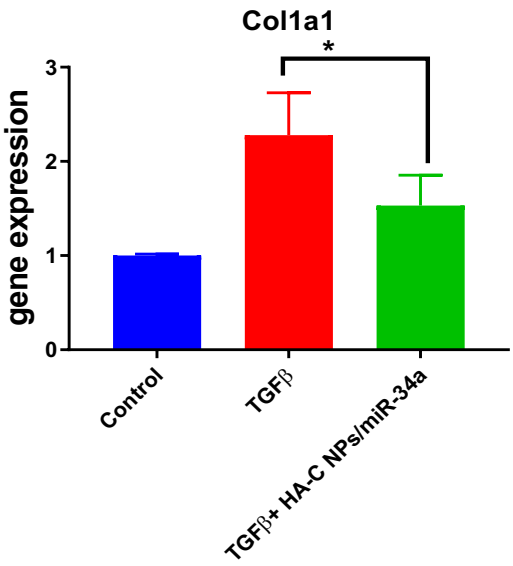

Figure 22. Efficacy of HA-C NPs/miR-34a transfection on aHSC.
Mouse primary HSCs were transfected with HA-C NP/miR-34a followed by activation using TGFβ for 48h. Data were analyzed by one-way ANOVA followed by Turkey's comparison test. Data are expressed as mean ± SD (n=3). *p<0.05.

3.3.7 In Vivo Tissue Distribution and Cellular Localization of HA-C NPs

Pharmacokinetics and biodistribution are of vital importance for the therapeutic efficiency of NPs. Particular ligand-receptor interactions during the pathogenesis of AALD could be leveraged. With the effort to investigate the tissue biodistribution of HA-C NPs delivering nucleic acids, we prepared HA-C NPs/Cy5.5-siRNA and intravenously injected NPs into EtOH/CCl_4 treated mice and pair-fed control mice. 24 hours after the injection, mice were sacrificed and organs were harvested and imaged under IVIS. HA-C NPs mainly accumulated in the liver in EtOH/CCl_4 mice and control mice, followed by kidneys and spleen. Quantitative analysis of fluorescence revealed that HA-C NPs showed higher delivery of Cy5.5-siRNA to

the EtOH/CCl_4 liver where the HSCs are activated compared to pair-fed control livers that are rich in qHSCs (Figure 23C), suggesting the selective targeting effect of HA-C NPs to aHSCs.

We then evaluated the specific uptake of NPs on the cellular levels using FACS. Different hepatic cells were sorted (Figure 24), including LSECs (CD45-CD31+), KCs (CD45+CD11b^{int} F4/80^{hi}), infiltrating monocytes (CD45+CD11b^{hi}F4/80^{int}), aHSCs (CD45-CD31-SMA+) and neutrophils (CD45+Ly6G+). As shown in Figure 25, we compared the Cy5.5 fluorescence in different hepatic cells in both EtOH/CCl_4 mice and pair-fed control mice. Phagocytotic KC uptake of fluorescent RNA was reduced significantly in the EtOH/CCl_4 mice compared to that in pair-fed control mice. In contrast, HSC had higher uptake of fluorescent RNA in the EtOH/CCl_4 mice than in the pair-fed control, suggesting aHSCs in EtOH/CCl_4 are more likely to take up HA-C NPs. In LSEC and monocytes, there was a decreased uptake of fluorescent RNA in the EtOH/CCl_4 mice than in the pair-fed mice. In neutrophils, there were no obvious differences of two groups of mice. Direct comparison of the NP uptake in the different hepatic cell types showed that aHSCs have the highest uptake, followed by KCs, monocytes and LSECs, and neutrophils (Figure 26). These results validated our initial hypothesis that HA-C NPs will elevate targeting to aHSCs while keeping some delivery to KCs. The reason underlying is due to the elevated CXCR4 and CD44 receptors levels on aHSCs, which serve as the active targeting receptors for HA-C NP.

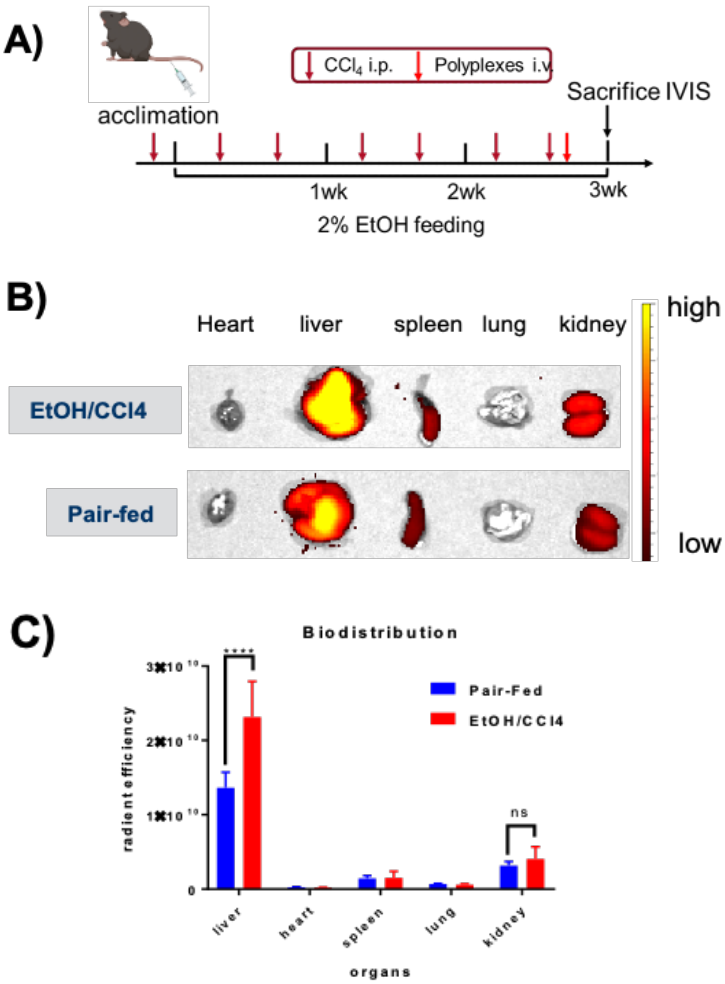

Figure 23. Biodistribution of HA-C NPs.

(A) alcoholic liver fibrosis model, NPs were injected at the end of model. (B) 24 h after the NP injection, mice were sacrificed and organs were harvested imaging under IVIS. (C) Distribution in different organs 24 h after the IV injection of nanoparticles. Data were analyzed by two-way ANOVA followed by Tukey's comparison test. Data are expressed as mean ± SD (n=6). ****p<0.0001.

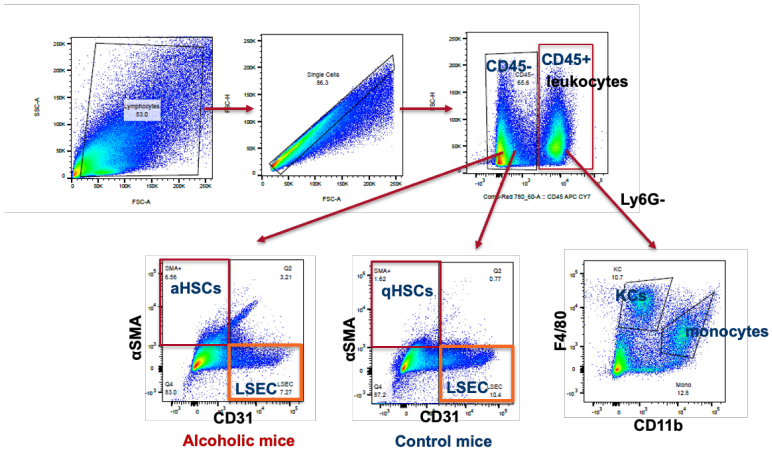

Figure 24. Multi-color flow cytometry sorting by different antibodies, including myeloid cells and non-parenchymal cells.

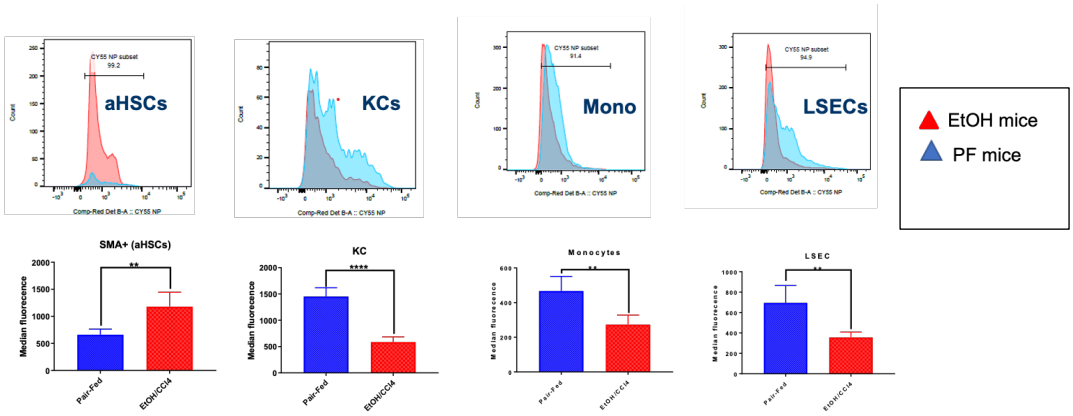

Figure 25. Fluorescent NPs distribution on cellular level and quantification of MFI of NPs in different cells.

The non-parenchymal cells (NPCs) were seperated and detected using cell-specific antibodies. The Cy5.5 fluorescence of HA-C NPs in different NPCs of alcoholic liver and pair-fed control liver was compared. Red peak indicate NPs fluorescence uptake by EtOH mice and blue peak indicate NPs fluorescence uptake by Pair-fed mice. Data were analyzed by one-way ANOVA followed by Tukey's comparison test. Data are expressed as mean ± SEM (n = 3 or 4) ** $p < 0.01$, *** $p < 0.001$, **** $p < 0.0001$.

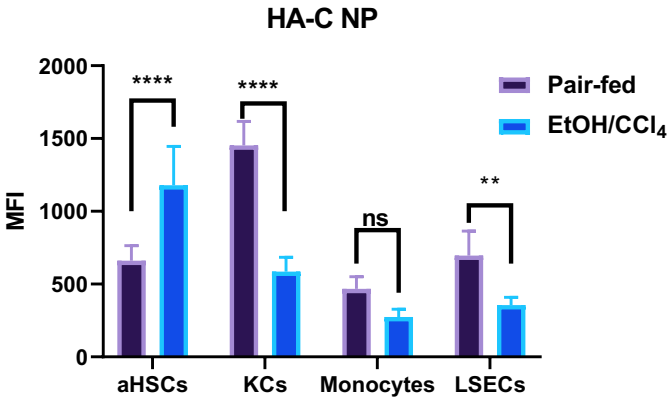

Figure 26. Comparison of Cy5.5 fluorescence in different hepatic cells in alcoholic liver.
Data were analyzed by one-way ANOVA followed by Tukey's comparison test. Data are expressed as mean ± SEM (n = 3 or 4) ** $p < 0.01$, *** $p < 0.001$, **** $p < 0.0001$.

3.4 Conclusion

In conclusion, stable HA-C NP was fabricated with dual active targeting ligands to aHSCs in AALD. It provides an increased cellular uptake and efficient transfection efficiency to aHSCs, In vivo study of mice, HA-C NPs indicate a potential treatment for liver fibrosis by enhanced targeting of nucleic acids to aHSCs during alcoholic liver fibrosis.

Chapter 4. Macrophage membrane-camouflaged miRNA nanocarriers ameliorate alcohol-associated liver fibrosis

4.1 Introduction

Cell therapies, like stem cells and macrophages, are promising and effective for chronic liver fibrosis and cirrhosis [186]. In a previous cytotherapy study [187], bone marrow derived macrophages (BMDMs) were polarized by PBS into M0, LPS/IFN-γ into M1or IL-4 into M2

phenotypes respectively. Hepatic fibrosis models induced by CCl_4 or Bile duct ligation (BDL) were used to test the therapeutic effect of M0, M1 and M2 macrophages. Sirius red and Masson staining of liver sections showed that M1 and M0 BMDMs exhibited the highest ability to reduce liver extracellular matrix deposition than M2. Nevertheless, there are some drawbacks when using live cell treatment. First, the viability is important for the cytotherapy. As a live drug, macrophages used for cytotherapy need to be freshly prepared or carefully cryo-stored before final formulation. Besides, the big size of macrophages impedes their targeting efficiency, they are prone to be taken up by the lungs before they can reach the liver [188,189].

Extracellular vesicles (EVs) have great potential in biomedical applications, many studies have focused on this field. For example, there is interest in exosomes that are one type of EVs which commonly used in biomarker discovery and therapeutic carrier studies. Nanovesicles (NVs), which are prepared by the serial extrusion of cells, have cell membranes and sizes similar to exosomes. These NVs have higher production-yield and are more enriched in proteins and RNAs than exosomes. Moreover, unlike the inconvenience of whole cell macrophages, NVs provide long-term cryo-storage convenience for medical use. Macrophage cell membrane derived NVs are extensively applied in biomedical applications, including cancer, inflammatory diseases, and infectious diseases. It is expected that macrophage derived NVs will be more effective in the intercellular transfer of biomolecules and in the induction of subsequent phenotypic changes in the recipient cells [190].

As efficient gene delivery materials, some polycations such as PEI nanoparticles are undergoing clinical trials, nevertheless, there are few approved on market because of their toxicity and non-degradable properties [191]. The clearance of non-biodegradable NPs is problematic because

the majority of non-biodegrade NPs are more likely to be taken up by MPS and retained from months to years [192]. Combining synthetic polymers with natural biomaterials like macrophage derived NVs has gained much attention during the past years. These biomimetic NVs coating nanocarriers enable prolonged blood circulation time and perform bioactive functions with an efficient accumulation to inflamed, infectious and neoplastic tissues. This macrophage NVs camouflage method can overcome the shortcomings of the immunogenicity of synthetic polymers and avoid the complexity of ligand polymer synthesis [190].

From one previous study [193], leukocyte membrane camouflaged nanoparticles enhanced the blood circulation time by reducing the particle opsonization by highly abundant serum proteins, the consequent specific clearance by phagocytosis was inhibited as well. Leukocyte membrane coating identified significantly reduced particle uptake when the donor membrane matched that of the host phagocytic cells. Thereafter, we designed a macrophage-membrane coated NV as a camouflaged nanocarrier system to deliver small non-coding RNAs. One aim of this design is to avoid MPS uptake and increase the systemic retention time by the macrophage camouflage. Thus, this approach can accelerate the metabolism of polymeric NPs and reduce the potential toxicity of polycations in vivo [193]. Another aim of this study is to show that the macrophage-derived nanovesicles are capable of relieving liver fibrosis by recruiting antifibrotic Ly6C^{lo} macrophages, enhancing MMPs, and reducing TIMPs expression (Figure 27).

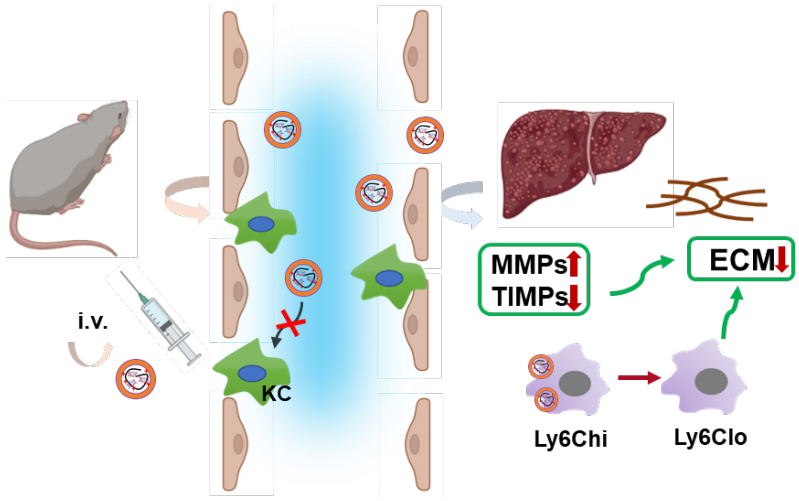

Figure 27. Mechanism of biomimetic NPs (MP) for the treatment of alcohol-associated liver fibrosis.

4.2 Methods and Materials

4.2.1 Isolation of macrophage membranes

The macrophage membrane isolation procedure was modified from a previous study [194]. RAW 264.7 cells were harvested and resuspended at a concentration of 1*10^7 cells/mL in ice-cold Tris-magnesium buffer (TM buffer, pH 7.4, 0.01 M Tris and 0.001 M $MgCl_2$) and prepared through a mini-extruder (Avanti) without a polycarbonate membrane for 20 times to disrupt the cells. The cell homogenate was mixed with 1 M sucrose to a final concentration of 0.25 M sucrose, and then centrifuged at 2000g and 4 °C for 10 min. The supernatant was collected and further centrifuged at 3000g and 4 °C for 30 min to collect the cell membrane. The cell membrane was washed with ice-cold TM-buffer with 0.25 M of sucrose and collected by centrifugation at 3000g and 4 °C for 30 min. The protein content in the purified macrophage membrane was determined by BCA protein assay for further preparation of MPs.

4.2.2 Preparation and fabrication of MPs

MPs were fabricated by coating polyplexes with a macrophage membrane by a direct mixing method. Polyplexes were formulated by complexing PEI-Chol (Cholesterol-modified PEI, cholesterol modification used for decreasing toxicity of PEI) solution with scrambled siRNA solution at w/w 2. Afterwards, the purified macrophage membrane with protein contents 25μg was physically mixed with equal volume of polyplexes (containing 10μg siRNA at PEI-Chol/siRNA w/w ratio 2) to prepare MPs. To characterize the MPs, the particle size and zeta potential of MPs were measured by DLS.

4.2.3 Cellular uptake

Murine RAW 264.7 macrophages (ATCC, Manassas, VA) were cultured under 5% CO_2 in DMEM supplemented with 10% FBS and 1% Pen-Strep at 37°C. When confluency reached 80-90%, the RAW 264.7 cells were scraped to dislodge and subcultured. For uptake evaluation, the cells were seeded in 12-well plates and cultured to 60% confluency. The cells were incubated with the nanoparticles containing fluorescently labeled FAM-siRNA (100 nM) for 4 h. Cellular uptake was measured in Raw 264.7 cells, washed with PBS and the nucleuses were stained with Hoechst 33342 for 10 min. Then the cells were imaged using a Confocal microscopy (LSM800 Laser Scanning Microscope, Zeiss, Jena, Germany).

4.2.4 In Vivo Biodistribution of MPs on EtOH/CCl_4 model

All animal experiments were performed in C57BL/6J female mice purchased from Jackson Laboratories and following the protocol approved by the University of Nebraska Medical

Center Institutional Animal Care and Use Committee. An AALD fibrosis model was established by feeding the mice an EtOH-containing Lieber-DeCarli (LD) daily liquid diet (Dyets Ins., Bethlehem, PA, USA) combined with repeated intraperitoneal injection of CCl_4 for 6 weeks. In brief, on day 0 mice were started on 1% (v/v) EtOH LD liquid diet or control isocaloric liquid diet without EtOH for two days. Starting on day 3, the mice were injected twice per week with CCl_4 (1mL/kg of 10% CCl_4 in olive oil) and fed with 2% EtOH LD liquid diet or the control isocaloric diet. The daily intake of the EtOH mice was monitored, and the following day the equivalent calories were administered to control mice. At the end of the animal model, both the EtOH mice and Pair-fed mice were injected intravenously with 200μL of fluorescently labeled MPs/Cy5.5-siRNA (1mg/kg Cy5.5-siRNA) or Polyplexes/Cy5.5-siRNA as the control. Mice were sacrificed 24 h and 48 h post-injection, and major organs were harvested for imaging by Xenogen IVIS 200.

4.2.5 Flow cytometry

Flow cytometric analysis of tissue leukocytes were performed. Briefly, liver tissues were digested with collagenase type-IV (Worthington) at 37◦C with collagenase solution for 40min. Extracts were filtered using 40μm cell strainers and parenchymal cells were removed by sedimentation for 45 min at 4◦C followed by centrifugation for 5 min at 15g (method modified from previous paper) [177]. The remaining non-parenchymal cells mixture were subjected to red blood cell lysis buffer and washed by PBS using centrifugation for 5 min at 300g. Then the cell pellets were stained by unconjugated anti-CD16/32 (Fc block, BD), and followed by staining with fluorochrome-conjugated antibodies F4/80 and Ly6C (BD bioscience, US) in Cell

staining buffer. After 30min incubation, unbound antibody was washed with PBS [178]. Flow cytometry were performed using a BD FACS LSR II Green flow cytometer. Data were analyzed using FlowJo.

4.2.6 In Vivo Anti-fibrosis efficacy measurements of MPs

All animal experiments were performed in C57BL/6 female mice purchased from Jackson Laboratories following the protocol approved by the University of Nebraska Medical Center Institutional Animal Care and Use Committee. An AALD fibrosis model was established by feeding the mice an EtOH-containing Lieber–DeCarli (LD) daily liquid diet (Dyets Inc., Bethlehem, PA, USA) combined with repeated intraperitoneal injection of CCl_4 for 6 weeks. In brief, on day 0 mice were started on 1% (v/v) EtOH LD liquid diet or control isocaloric liquid diet without EtOH for two days. Starting on day 3, the mice were injected twice per week with CCl_4 (1 mL/kg of 10%CCl_4 in olive oil) and fed with 2% EtOH LD liquid diet or the control isocaloric diet. The daily intake of the EtOH mice was monitored, and the following day the equivalent calories were administered to control mice. Starting the third week, mice were injected twice per week with the treatment nanoparticles. All nanoparticle treatments were given 24 h after a CCl_4 injection. There were three treatment groups, with 6 mice per group: (i) pair-fed control, (ii) EtOH LD diet + CCl_4 + PBS, (iii) EtOH LD diet + CCl_4 + MP/anti-miR- NC. Nanoparticles (10 μL/kg) were injected twice per week from the third week and last for 4 weeks via tail vein at a dose of 1 mg/kg of miRNA and MP composed of polymer/miRNA ratio of 2 coated with macrophage membrane containing protein 1.25mg/kg (protein content tested by BCA assay). Mice were sacrificed 24 h after the

last treatment and the liver tissues as well as the blood samples were collected. The livers were stored in RNAlater (Qiagen, Valencia, CA, USA) or 10% formalin. The mRNA expression of fibrotic markers was analyzed by SYBR Green RT-PCR. Extracted RNA (2 μg) was converted into cDNA using a High-Capacity cDNA Transcription Kit (Applied Biosystems, Waltham, MA, USA). The PCR reactions were run on Rotor-Gene Q (QIAGEN) equipment with iTaq Universal SYBR Green Supermix (Bio- Rad, Hercules, CA, USA) and GAPDH as a housekeeping gene. Relative mRNA levels were calculated based on the comparative threshold value (Ct) method. Primers sequence (5'-3') used include:

FM1_Col1a1: CGTATVACCAAACTCAGAAG
RM1_Col1a1: GAAGCAAAGTTTCCTCCAAG
FM1_MMP2: GAGATCTTCTTCTTCAAGGAC
RM1_MMP2: AATAGACCCAGTACTCATTCC
FM1_MMP9: CTTCCAGTACCAAGACAAAG,
RM1_MMP9: ACCTTGTTCACCTCATTTTG;
FM1_MMP13: CTTTAGAGGGAGAAAATTCTGG,
RM1_MMP13: CATCATCATAACTCCACACG;
FM1_Timp2: GGATTCAGTATGAGATCAAGC
RM1_Timp2: GCCTTTCCTGCAATTAGATAC

4.2.7 Statistical Analysis

The results are presented as mean ± SD or SEM. One-way ANOVA was used and followed by Tukey's multiple comparison test to analyze statistical differences among multiple groups. Differences were assessed to be significant: *p<0.05 was considered as a minimal level of significance, and **p<0.01 and ***p<0.001 were considered as very significantly difference. All the statistical analyses were performed with GraphPad Prism 8.

4.3 Results and Discussion

4.3.1 Fabrication and characterization of MP

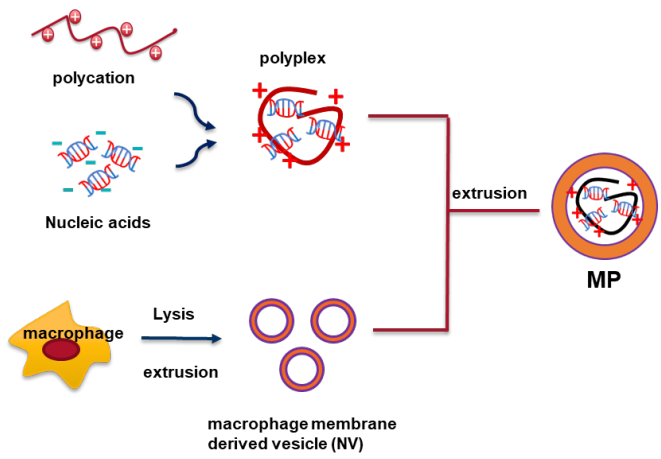

Figure 28. Fabrication of biomimetic nanoparticles.

RAW 264.7 macrophage cells were disrupted first by direct extrusion and lysed under hypotonic conditions. Cell nucleus and organelles were discarded after centrifugation. The protein content in the purified membrane was determined by bicinchoninic acid (BCA) protein assay. MPs with various protein contents were formulated using extrusion through a series of polycarbonate membrane with pore sizes of 400 and 200 nm (Figure 28).

Size, PDI, surface charge and the retention of surface proteins are crucial criteria for the fabrication of a successful biomimetic NP prior to the further therapeutic applications. DLS was used for determining the size of various particles, before decoration with membrane, the size was around 70 nm, and it increased to around 140 nm after camouflage accompanied with a decrease of surface charge (Figure 29 A). This self-assembly process was driven by the electrostatic interaction between the positive surface of polyplexes and negative charge of phosholipids of cell membranes. The evidence suggested the successful decoration of the polyplex with a macrophage membrane.

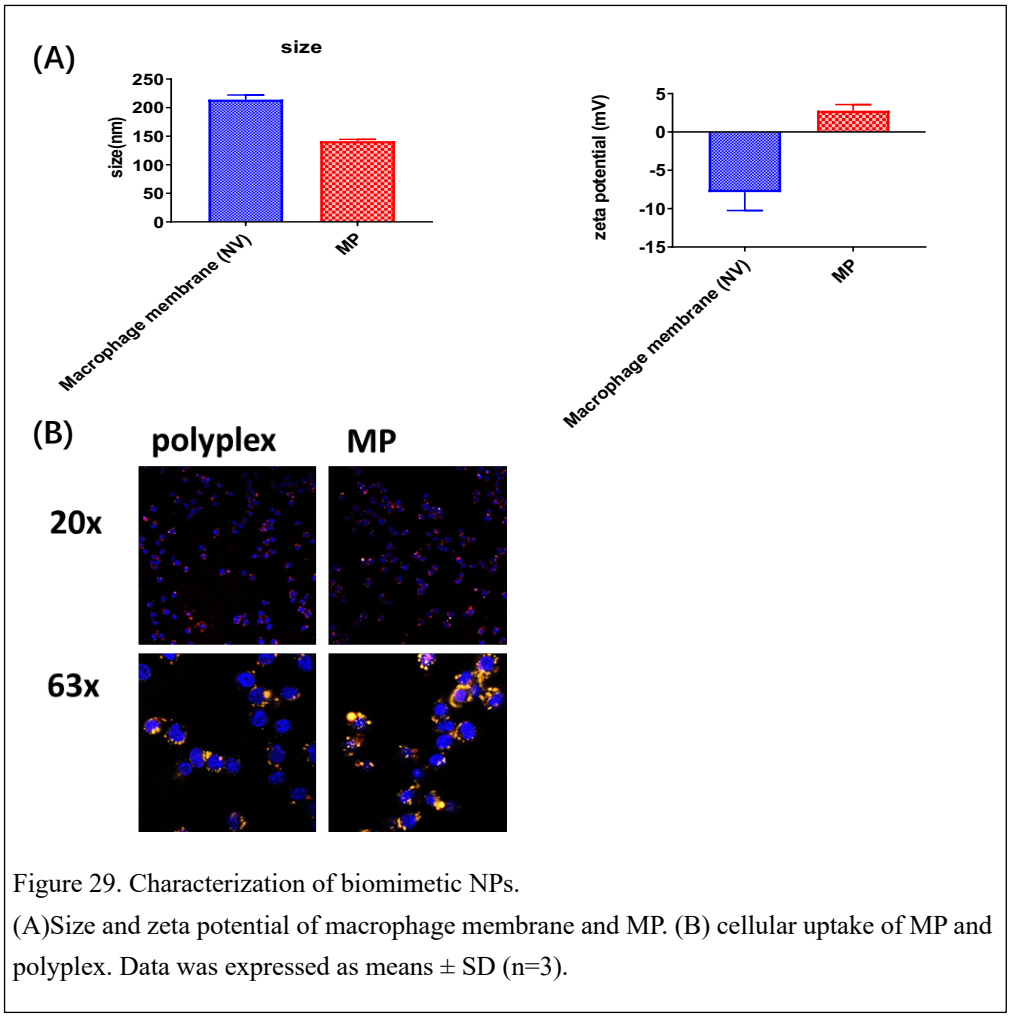

Figure 29. Characterization of biomimetic NPs.
(A)Size and zeta potential of macrophage membrane and MP. (B) cellular uptake of MP and polyplex. Data was expressed as means ± SD (n=3).

4.3.2 In vitro toxicity of MP and uptake by macrophages

Given that the primary targeting site upon the systemic administration is the inflamed liver, macrophages were chosen to test the cellular uptake of MPs in vitro. Kupffer cells are the first cell type that MPs will encounter in the circulation. We did cellular uptake of MPs on Raw 264.7 which mimics cell type of KCs. In figure 29B, MP provided high cellular uptake in Raw 264.7, suggesting a comparable uptake efficiency with control polyplex group by confocal microscopy.

4.3.3 Biodistribution of biomimetic MPs in EtOH/CCl_4 model

To further study if the MPs provide improved delivery efficiency to inflamed liver, EtOH/CCl_4 model was used and mice were intravenously injected with MPs/Cy5.5 RNA or control polyplexes/Cy5.5 RNA. At respective end points of 24 or 48 h, mice were euthanized and the organs collected, washed in PBS, and imaged by IVIS. In figure 30, fluorescence signals showed that both MPs and polyplexes have high accumulation in the liver, followed by other organs, kidney, lung, spleen and heart. Moreover, MPs have slightly higher, yet no significant difference, in the accumulation of polyplexes in EtOH/CCl_4 livers after 48 h, indicating that macrophages camouflage provides a potentially improved targeting to inflamed liver. Importantly, MPs enhanced delivery of nuclei acids in EtOH/CCl_4 liver compared with control pair-fed liver (Figure 30B). Longer time points including 72, 96, 120 h will be tested to verify our hypothesis that MP can enhance the blood circulation of nanoparticles in body. Taken together, we suggest that MPs may improve nucleic acid delivery during AALD, but longer time points are needed. The reason behind this phenomenon may be attributed to the

macrophage cell makers like CD45 and CD11b to help evade MPS surveillance. MPS recognizes macrophage membrane camouflaged nanocarriers as innate macrophage cells, thus less nanocarriers would be taken up by MPS.

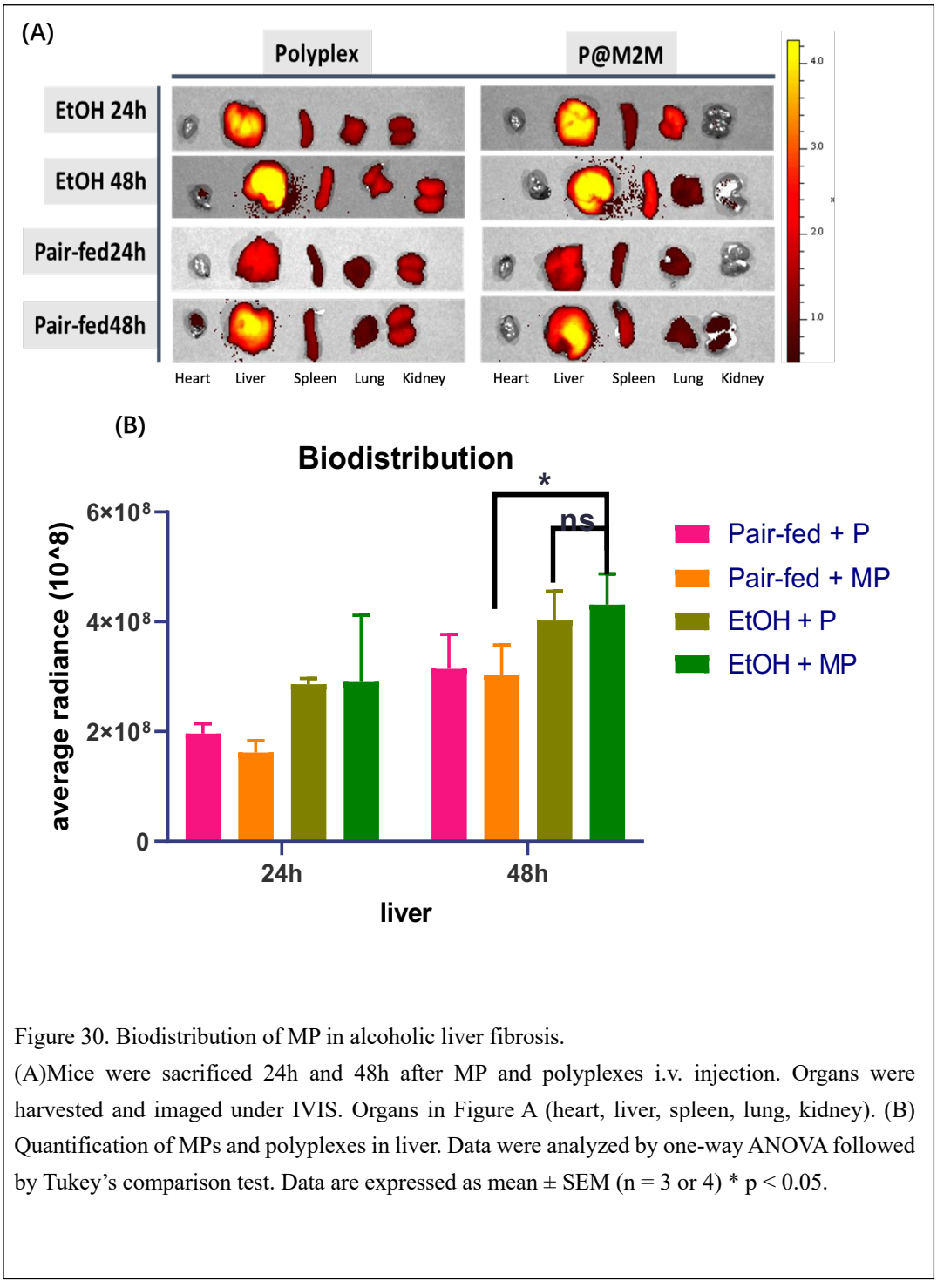

Figure 30. Biodistribution of MP in alcoholic liver fibrosis.
(A)Mice were sacrificed 24h and 48h after MP and polyplexes i.v. injection. Organs were harvested and imaged under IVIS. Organs in Figure A (heart, liver, spleen, lung, kidney). (B) Quantification of MPs and polyplexes in liver. Data were analyzed by one-way ANOVA followed by Tukey's comparison test. Data are expressed as mean ± SEM (n = 3 or 4) * $p < 0.05$.

4.3.4 MP ameliorated fibrosis in EtOH/CCl_4 model

Polyplexes with scrambled RNA were used as the core that was then decorated with macrophage membrane to validate if the macrophage membrane can have therapeutic effects on AALD. To fabricate macrophage-membrane camouflaged nanoparticles, macrophage membranes were first prepared by a serial of extrusion through polycarbonate membranes, 1μm, 400nm, 200nm. Then equal volume of polyplexes and macrophage membrane solution were mixed to get macrophage membrane camouflaged nanoparticles (MP). We used a 6 week EtOH/CCl_4 model with nanoparticles injected 2 weeks after EtOH/CCl_4 induction and for a duration of 4 weeks. At study end, the fibrosis level was evaluated and the mRNA levels of Collagen 1α1 was markedly lowered in EtOH/CCl_4+MP group than in EtOH/CCl_4 + PBS group. Sirius Red staining also verified that collagen was significantly decreased in EtOH/CCl_4+MP group (Figure 31). Results indicate MP could keep the bioactive function of live macrophages that can have anti-fibrotic effect in fibrosis mice. Meanwhile, the MPs give a potential enhanced delivery of nucleic acids to AALD.

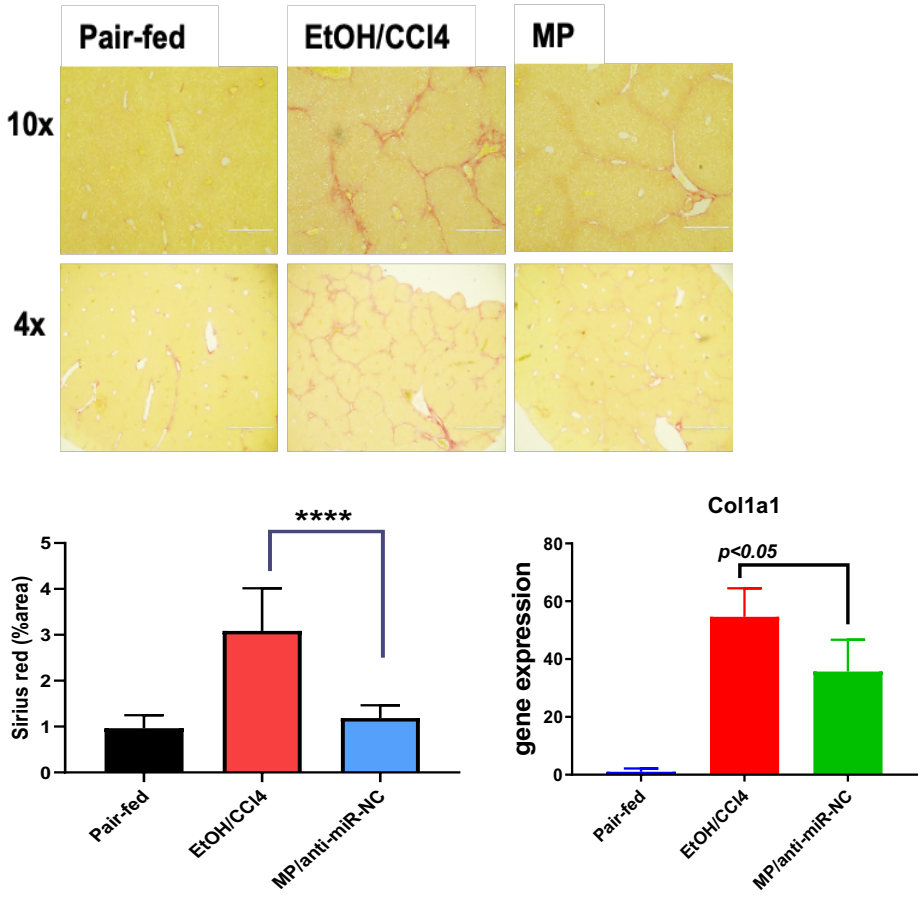

Figure 31. Therapeutic effects of MP/anti-miR-NC on alcoholic liver fibrosis.
Sirius Red staining for liver tissues in different group. Quantification for collagen deposition by Image J. Data were analyzed by one-way ANOVA followed by Tukey's comparison test. Data are expressed by mean ± SEM (n=3 or 4). ** $p < 0.01$, *** $p < 0.001$, **** $p < 0.0001$.

4.3.5 MP modulating hepatic microenvironment by recruiting Ly6C^{lo} phenotype restorative macrophages

We next tested the potential mechanism for the antifibrotic effects of this macrophage membrane camouflaged nanoparticle. Accordingly, during the fibrosis regression process, infiltrated macrophages with a Ly6C^{lo} phenotype expressing high levels of CCR5 and CX3R1 and produce MMPs to ameliorate hepatic fibrosis. Ly6C^{lo} macrophages promote HSCs apoptosis via MMP9 and TNF-related apoptosis inducing ligand (TRAIL) [195,196]. To test that if the MPs recruit Ly6C^{lo} macrophages, the F4/80^{+} macrophages were isolated from fibrotic mice after MP treatment. The fibrotic mice receiving MP recruited significantly higher amount of F4/80^{+}Ly6C^{lo} restorative macrophages compared with EtOH/CCl_4 mice. Besides, we

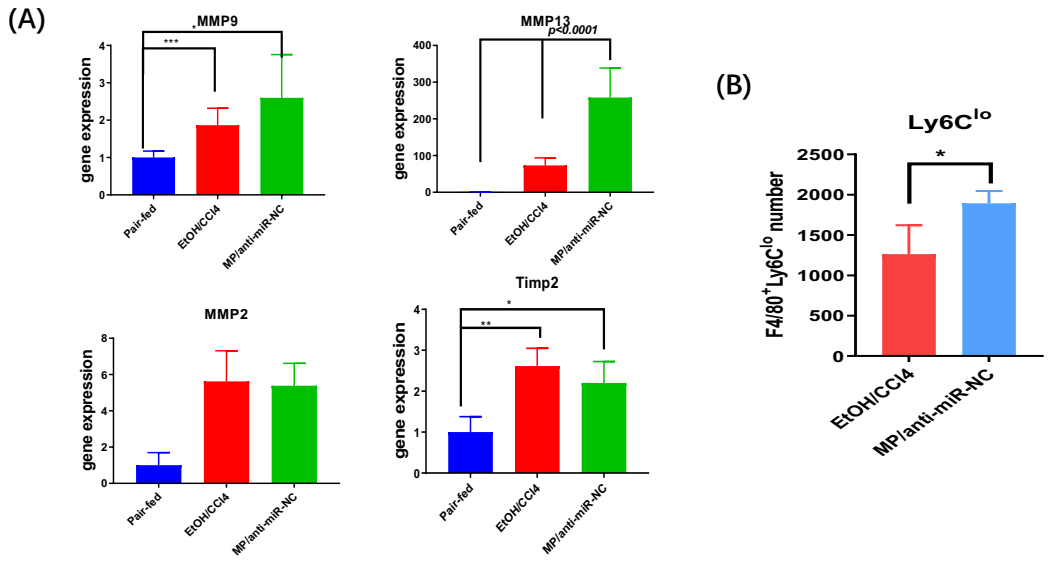

Figure 32. Antifibrotic mechanism of MPs.
(A)MMPs and TIMPs expression in alcoholic liver fibrosis and MP treatment groups. (B) antifibrotic Ly6Clo infiltrated tested by flow cytometry. Data were analyzed by one-way ANOVA followed by Tukey's comparison test. Data are expressed by mean ± SEM. * p<0.05, ** p < 0.01, *** p < 0.001, **** p < 0.0001.

evaluated enzyme levels in mice using RT-PCR, MMP13 was significantly increased in MP

treated group compared with EtOH/CCl_4 group. MMPs play important roles in fibrosis remodeling, they facilitate the resolution of liver fibrosis. MMPs increased in EtOH/CCl_4 mice and further increased by MP treatment. Collectively, regulating MMPs and TIMPs level by $Ly6C^{lo}$ macrophages contributes to the anti-fibrotic effect of MPs.

4.4 Conclusion

Macrophage membrane camouflaged nanocarrier (MP) keep the bioactive antifibrotic function of source macrophages, while providing a potential for enhanced delivery of nucleic acids to AALD.

Discussion

AALD is noteworthy among all the chronic liver diseases as alcohol is one of the leading causes for liver fibrosis and cirrhosis which are responsible for the majority of alcohol-related morbidity and mortality. Cessation of alcohol, nutritional support and corticosteroids are the traditional treatments. However, there are no pharmacological treatments approved. Thus, targeted therapies are urgently needed to provide effective treatment for AALD. In my studies, alcohol-induced liver fibrosis was the main stage we investigated. Nucleic acids delivered by polymeric nanoparticles targeting specific mechanisms were designed to treat alcoholic liver fibrosis.

To understand and evaluate the therapeutic effects of nanoparticles in AALD, well-established animal models are important tools. Currently, there are no animal models that can exactly mimic all the conditions in human alcoholic liver. The development of new drugs for AALD is

hampered by the lack of studies and the drawbacks of existing animal models that do not reflect all the conditions of the human disease. Several rodent models have been developed based on the pattern of alcohol consumption in humans to mimic different stages of AALD [197]. One of the most frequently used diet models is the ad libitum feeding with the Lieber-DeCarli liquid diet (LD) supplemented with ethanol for 4-12 weeks. But this model resembled mild hepatic steatosis in human with moderate or no inflammation [198]. Combination of LD and a "second hit" hepatotoxin such as carbon tetrachloride (CCl_4) provides more severe liver injury conditions [34]. Therefore, to evaluate therapeutic effects of nanoparticle on alcoholic liver fibrosis, we used an alcoholic liver fibrosis model by moderate alcohol consumption using LD with a secondary liver insult by CCl_4.

To achieve targeted therapies for AALD, in chapter 2, we synthesized CXCR4 antagonism ligand-conjugated polymers for active targeting delivery of nucleic acids to activated hepatic cells in alcoholic liver fibrosis model. CXCR4 antagonist conjugated polycation Chol-PCX successfully delivered anti-miR-155 both in vitro and in vivo. The Chol-PCX/anti-miR-155 NPs markedly reduced aminotransferase enzymes and alcohol-related collagen deposition in liver parenchyma in the alcohol liver fibrosis model. Furthermore, in chapter 3, dual-targeting polymer HA-C was synthesized, HA-C polymer include hyaluronic acids that target to CD44 receptor and cyclam that binds to CXCR4 receptor. Both CD44 and CXCR4 are overexpressed on aHSCs. Then the bifunctional HA-C polymer was camouflaged on polyplexes to form HA-C NPs. HA-C NPs distribution was evaluated both in vitro and in vitro. The in vitro results showed enhanced uptake of nucleic acids in mouse primary HSC compared to polyplexes. In alcoholic liver fibrosis mice in vivo, HA-C NPs significantly increased biodistribution of

fluorescent siRNA to aHSCs in alcoholic mice than in qHSCs in healthy mice, suggesting the dual-targeting effect of HA-C NPs. In addition, in chapter 4, biomimetic macrophage-membrane camouflaged nanocarriers (MP) were designed to avoid MPS surveillance and at the same time keep the biofunction of source macrophage to perform an antifibrotic effect. Even though only slightly elevated accumulation of MP in contrast to polyplexes at time points 24 h and 48 h, longer retention time of MP is expected in alcoholic liver fibrosis, which will be performed in future.

From the physicochemical perspectives, liver sinusoids are special capillaries that differ from other capillaries in the human body, because of the presence of open pores or fenestrae in endothelium. To arrive at the HSC in Space of Disse or parenchymal hepatocytes, nanoparticles must be able to evade MPS uptake and pass through the liver fenestrae with a diameter around 100-150nm in rodents. From our studies, physical properties of all NPs were suitable for delivery of nucleic acids to target aHSCs in the dysfunctional microenvironment of alcoholic liver fibrosis. All the nanoparticles have particle size small enough enabling them to pass through the open pores in liver endothelium, arriving at aHSCs that are responsible for the fibrogenesis during AALD. Positive charged Chol-PCX/miRNA NPs can increase the transfection efficiency, negative charged HA-C NPs can increase stability in serum by preventing them from disassociation by heparin. Near neutral surface of MP also prevented opsonization, therefore, avoiding MPS surveillance.

Overall, the active CXCR4 and CD44 binding ligands equip NPs with selective targeting effects, making it possible to specifically bind to aHSCs. Bioactive membrane coated NPs can combine both the advantages of nanomaterials and macrophages to potentiate the therapeutic effects.

Future work

In Chapter 3, biodistribution of HA-C NPs has been investigated on both organ level and cellular level. The next step would be the evaluation of the therapeutic effect of HA-C NPs delivering nucleic acids in the alcoholic liver fibrosis model. According to the biodistribution study in chapter 3, NPs are mainly taken up by aHSCs, followed by KCs. Gene expression of collagen are increased significantly in aHSCs, therefore HA-C/siCol1a1 will be used to treat alcoholic liver fibrosis. MiR-155 is elevated in KCs in AALD as we validated in Chapter 2, therefore, HA-C/siCol1a1 and HA-C/anti-miR-155 will be combined together to potentiate the therapeutic effects of HA-C NPs for AALD.

In the Chapter 4 biodistribution study, only slightly elevated circulation time of MPs was observed in contrast to polyplexes at the measured time points. Longer time points of MP and polyplexes as a control will be tested in alcoholic liver fibrosis. In addition, therapeutic effects of MPs delivering antifibrotic and anti-inflammatory nucleic acids in AALD models will be conducted as well. The promising candidates for miRNAs are listed in Section 1.3.

Bibliography

1. Poznyak, V.; Rekve, D. Global status report on alcohol and health 2018. *Geneva: World Health Organization* **2018**, *450*.
2. Xu, J.; Murphy, S.L.; Kochanek, K.D.; Arias, E. Mortality in the United States, 2021. *NCHS Data Brief* **2022**, 1-8.
3. Julien, J.; Ayer, T.; Bethea, E.D.; Tapper, E.B.; Chhatwal, J. Projected prevalence and mortality associated with alcohol-related liver disease in the USA, 2019–40: a modelling study. *The Lancet Public Health* **2020**, *5*, e316-e323.
4. Dugum, M.; McCullough, A. Diagnosis and management of alcoholic liver disease. *Journal of clinical and translational hepatology* **2015**, *3*, 109.
5. Ramkissoon, R.; Shah, V.H. Alcohol use disorder and alcohol-associated liver disease. *Alcohol Research: Current Reviews* **2022**, *42*.
6. Degré, D.; Stauber, R.E.; Englebert, G.; Sarocchi, F.; Verset, L.; Rainer, F.; Spindelboeck, W.; Njimi, H.; Trépo, E.; Gustot, T. Long-term outcomes in patients with decompensated alcohol-related liver disease, steatohepatitis and Maddrey's discriminant function< 32. *Journal of hepatology* **2020**, *72*, 636-642.
7. Yang, Y.M.; Cho, Y.E.; Hwang, S. Crosstalk between oxidative stress and inflammatory liver injury in the pathogenesis of alcoholic liver disease. *International Journal of Molecular Sciences* **2022**, *23*, 774.
8. Mandrekar, P.; Szabo, G. Signalling pathways in alcohol-induced liver inflammation. *Journal of hepatology* **2009**, *50*, 1258-1266.
9. Lakshman, M.R. Some novel insights into the pathogenesis of alcoholic steatosis.

Alcohol **2004**, *34*, 45-48.

10. Fischer, M.; You, M.; Matsumoto, M.; Crabb, D.W. Peroxisome proliferator-activated receptor α (PPARα) agonist treatment reverses PPARα dysfunction and abnormalities in hepatic lipid metabolism in ethanol-fed mice. *Journal of Biological Chemistry* **2003**, *278*, 27997-28004.
11. You, M.; Crabb, D.W. Molecular mechanisms of alcoholic fatty liver: role of sterol regulatory element-binding proteins. *Alcohol* **2004**, *34*, 39-43.
12. Baraona, E.; Lieber, C.S. Effects of ethanol on lipid metabolism. *Journal of lipid research* **1979**, *20*, 289-315.
13. Farooq, M.O.; Bataller, R. Pathogenesis and management of alcoholic liver disease. *Digestive diseases* **2016**, *34*, 347-355.
14. Szabo, G. Gut–liver axis in alcoholic liver disease. *Gastroenterology* **2015**, *148*, 30-36.
15. Bala, S.; Csak, T.; Saha, B.; Zatsiorsky, J.; Kodys, K.; Catalano, D.; Satishchandran, A.; Szabo, G. The pro-inflammatory effects of miR-155 promote liver fibrosis and alcohol-induced steatohepatitis. *Journal of hepatology* **2016**, *64*, 1378-1387.
16. Hritz, I.; Mandrekar, P.; Velayudham, A.; Catalano, D.; Dolganiuc, A.; Kodys, K.; Kurt-Jones, E.; Szabo, G. The critical role of toll-like receptor (TLR) 4 in alcoholic liver disease is independent of the common TLR adapter MyD88. *Hepatology* **2008**, *48*, 1224-1231.
17. Petrasek, J.; Dolganiuc, A.; Csak, T.; Nath, B.; Hritz, I.; Kodys, K.; Catalano, D.; Kurt-Jones, E.; Mandrekar, P.; Szabo, G. Interferon regulatory factor 3 and type I interferons are protective in alcoholic liver injury in mice by way of crosstalk of parenchymal and

myeloid cells. *Hepatology* **2011**, *53*, 649-660.

18. Pritchard, M.T.; McMullen, M.R.; Stavitsky, A.B.; Cohen, J.I.; Lin, F.; Medof, M.E.; Nagy, L.E. Differential contributions of C3, C5, and decay-accelerating factor to ethanol-induced fatty liver in mice. *Gastroenterology* **2007**, *132*, 1117-1126.

19. Albano, E. Role of adaptive immunity in alcoholic liver disease. *International Journal of Hepatology* **2012**, *2012*.

20. Lackner, C.; Tiniakos, D. Fibrosis and alcohol-related liver disease. *Journal of hepatology* **2019**, *70*, 294-304.

21. Sanz-García, C.; Fernández-Iglesias, A.; Gracia-Sancho, J.; Arráez-Aybar, L.A.; Nevzorova, Y.A.; Cubero, F.J. The space of disse: the liver hub in health and disease. *Livers* **2021**, *1*, 3-26.

22. Albanis, E.; Friedman, S. Antifibrotic agents for liver disease. *American Journal of transplantation* **2006**, *6*, 12-19.

23. Rangwala, F.; Guy, C.D.; Lu, J.; Suzuki, A.; Burchette, J.L.; Abdelmalek, M.F.; Chen, W.; Diehl, A.M. Increased production of sonic hedgehog by ballooned hepatocytes. *The Journal of pathology* **2011**, *224*, 401-410.

24. Jung, Y.; Brown, K.D.; Witek, R.P.; Omenetti, A.; Yang, L.; Vandongen, M.; Milton, R.J.; Hines, I.N.; Rippe, R.A.; Spahr, L. Accumulation of hedgehog-responsive progenitors parallels alcoholic liver disease severity in mice and humans. *Gastroenterology* **2008**, *134*, 1532-1543. e1533.

25. Ogawa, T.; Kawada, N.; Ikeda, K. Effect of natural interferon α on proliferation and apoptosis of hepatic stellate cells. *Hepatology international* **2009**, *3*, 497-503.

26. Kisseleva, T.; Brenner, D. Molecular and cellular mechanisms of liver fibrosis and its regression. *Nature Reviews Gastroenterology & Hepatology* **2021**, *18*, 151-166.

27. Winkle, M.; El-Daly, S.M.; Fabbri, M.; Calin, G.A. Noncoding RNA therapeutics—Challenges and potential solutions. *Nature reviews Drug discovery* **2021**, *20*, 629-651.

28. Cai, Y.; Yu, X.; Hu, S.; Yu, J. A brief review on the mechanisms of miRNA regulation. *Genomics, proteomics & bioinformatics* **2009**, *7*, 147-154.

29. Tang, Y.; Banan, A.; Forsyth, C.B.; Fields, J.Z.; Lau, C.K.; Zhang, L.J.; Keshavarzian, A. Effect of alcohol on miR-212 expression in intestinal epithelial cells and its potential role in alcoholic liver disease. *Alcoholism: Clinical and Experimental Research* **2008**, *32*, 355-364.

30. Bala, S.; Marcos, M.; Kodys, K.; Csak, T.; Catalano, D.; Mandrekar, P.; Szabo, G. Up-regulation of microRNA-155 in macrophages contributes to increased tumor necrosis factor α (TNFα) production via increased mRNA half-life in alcoholic liver disease. *Journal of Biological Chemistry* **2011**, *286*, 1436-1444.

31. Francis, H.; McDaniel, K.; Han, Y.; Liu, X.; Kennedy, L.; Yang, F.; McCarra, J.; Zhou, T.; Glaser, S.; Venter, J. Regulation of the extrinsic apoptotic pathway by microRNA-21 in alcoholic liver injury. *Journal of Biological Chemistry* **2014**, *289*, 27526-27539.

32. Feili, X.; Wu, S.; Ye, W.; Tu, J.; Lou, L. MicroRNA-34a-5p inhibits liver fibrosis by regulating TGF-β1/Smad3 pathway in hepatic stellate cells. *Cell biology international* **2018**, *42*, 1370-1376.

33. Wan, Y.; McDaniel, K.; Wu, N.; Ramos-Lorenzo, S.; Glaser, T.; Venter, J.; Francis, H.; Kennedy, L.; Sato, K.; Zhou, T. Regulation of cellular senescence by miR-34a in

alcoholic liver injury. *The American journal of pathology* **2017**, *187*, 2788-2798.

34. Satishchandran, A.; Ambade, A.; Rao, S.; Hsueh, Y.-C.; Iracheta-Vellve, A.; Tornai, D.; Lowe, P.; Gyongyosi, B.; Li, J.; Catalano, D. MicroRNA 122, regulated by GRLH2, protects livers of mice and patients from ethanol-induced liver disease. *Gastroenterology* **2018**, *154*, 238-252. e237.

35. Yin, H.; Liang, X.; Jogasuria, A.; Davidson, N.O.; You, M. miR-217 regulates ethanol-induced hepatic inflammation by disrupting sirtuin 1–Lipin-1 signaling. *The American Journal of Pathology* **2015**, *185*, 1286-1296.

36. Perry, M.M.; Moschos, S.A.; Williams, A.E.; Shepherd, N.J.; Larner-Svensson, H.M.; Lindsay, M.A. Rapid changes in microRNA-146a expression negatively regulate the IL-1β-induced inflammatory response in human lung alveolar epithelial cells. *The Journal of Immunology* **2008**, *180*, 5689-5698.

37. Sheedy, F.J.; Palsson-McDermott, E.; Hennessy, E.J.; Martin, C.; O'leary, J.J.; Ruan, Q.; Johnson, D.S.; Chen, Y.; O'neill, L.A. Negative regulation of TLR4 via targeting of the proinflammatory tumor suppressor PDCD4 by the microRNA miR-21. *Nature immunology* **2010**, *11*, 141-147.

38. Meng, F.; Glaser, S.S.; Francis, H.; Yang, F.; Han, Y.; Stokes, A.; Staloch, D.; McCarra, J.; Liu, J.; Venter, J. Epigenetic regulation of miR-34a expression in alcoholic liver injury. *The American journal of pathology* **2012**, *181*, 804-817.

39. McDaniel, K.; Herrera, L.; Zhou, T.; Francis, H.; Han, Y.; Levine, P.; Lin, E.; Glaser, S.; Alpini, G.; Meng, F. The functional role of micro RNA s in alcoholic liver injury. *Journal of cellular and molecular medicine* **2014**, *18*, 197-207.

40. Nichols, J.W.; Bae, Y.H. Odyssey of a cancer nanoparticle: from injection site to site of action. *Nano today* **2012**, *7*, 606-618.

41. Dilliard, S.A.; Siegwart, D.J. Passive, active and endogenous organ-targeted lipid and polymer nanoparticles for delivery of genetic drugs. *Nature Reviews Materials* **2023**, 1-19.

42. Nichols, J.W.; Bae, Y.H. EPR: Evidence and fallacy. *Journal of Controlled Release* **2014**, *190*, 451-464.

43. Böttger, R.; Pauli, G.; Chao, P.-H.; Fayez, N.A.; Hohenwarter, L.; Li, S.-D. Lipid-based nanoparticle technologies for liver targeting. *Advanced drug delivery reviews* **2020**, *154*, 79-101.

44. Braet, F.; Wisse, E. Structural and functional aspects of liver sinusoidal endothelial cell fenestrae: a review. *Comparative hepatology* **2002**, *1*, 1-17.

45. Anarjan, F.S. Active targeting drug delivery nanocarriers: Ligands. *Nano-Structures & Nano-Objects* **2019**, *19*, 100370.

46. Viale, M.; Tosto, R.; Giglio, V.; Pappalardo, G.; Oliveri, V.; Maric, I.; Mariggiò, M.A.; Vecchio, G. Cyclodextrin polymers decorated with RGD peptide as delivery systems for targeted anti-cancer chemotherapy. *Investigational New Drugs* **2019**, *37*, 771-778.

47. Li, Y.; Pu, S.; Liu, Q.; Li, R.; Zhang, J.; Wu, T.; Chen, L.; Li, H.; Yang, X.; Zou, M. An integrin-based nanoparticle that targets activated hepatic stellate cells and alleviates liver fibrosis. *Journal of Controlled Release* **2019**, *303*, 77-90.

48. Ji, D.; Wang, Q.; Zhao, Q.; Tong, H.; Yu, M.; Wang, M.; Lu, T.; Jiang, C. Co-delivery of miR-29b and germacrone based on cyclic RGD-modified nanoparticles for liver

fibrosis therapy. *Journal of Nanobiotechnology* **2020**, *18*, 1-11.

49. Caracciolo, G.; Farokhzad, O.C.; Mahmoudi, M. Biological identity of nanoparticles in vivo: clinical implications of the protein corona. *Trends in biotechnology* **2017**, *35*, 257-264.

50. Moghimi, S.M.; Hunter, A.C.; Murray, J.C. Long-circulating and target-specific nanoparticles: theory to practice. *Pharmacological reviews* **2001**, *53*, 283-318.

51. Liu, T.; Choi, H.; Zhou, R.; Chen, I.-W. RES blockade: A strategy for boosting efficiency of nanoparticle drug. *Nano Today* **2015**, *10*, 11-21.

52. Van Rooijen, N.; Sanders, A. Liposome mediated depletion of macrophages: mechanism of action, preparation of liposomes and applications. *Journal of immunological methods* **1994**, *174*, 83-93.

53. Zhang, Z.; Wang, C.; Zha, Y.; Hu, W.; Gao, Z.; Zang, Y.; Chen, J.; Zhang, J.; Dong, L. Corona-directed nucleic acid delivery into hepatic stellate cells for liver fibrosis therapy. *ACS nano* **2015**, *9*, 2405-2419.

54. Zhao, M.; Wang, L.; Wang, M.; Zhou, S.; Lu, Y.; Cui, H.; Racanelli, A.C.; Zhang, L.; Ye, T.; Ding, B. Targeting fibrosis: mechanisms and clinical trials. *Signal Transduction and Targeted Therapy* **2022**, *7*, 1-21.

55. Bansal, M.B.; Chamroonkul, N. Antifibrotics in liver disease: are we getting closer to clinical use? *Hepatology International* **2019**, *13*, 25-39.

56. Guo, Y.-C.; Lu, L.-G. Antihepatic fibrosis drugs in clinical trials. *Journal of Clinical and Translational Hepatology* **2020**, *8*, 304.

57. Baroni, G.S.; D'Ambrosio, L.; Curto, P.; Casini, A.; Mancini, R.; Jezequel, A.M.;

Benedetti, A. Interferon gamma decreases hepatic stellate cell activation and extracellular matrix deposition in rat liver fibrosis. *Hepatology* **1996**, *23*, 1189-1199.

58. Inagaki, Y.; Nemoto, T.; Kushida, M.; Sheng, Y.; Higashi, K.; Ikeda, K.; Kawada, N.; Shirasaki, F.; Takehara, K.; Sugiyama, K. Interferon alfa down-regulates collagen gene transcription and suppresses experimental hepatic fibrosis in mice. *Hepatology* **2003**, *38*, 890-899.

59. Cullis, P.R.; Hope, M.J. Lipid nanoparticle systems for enabling gene therapies. *Molecular Therapy* **2017**, *25*, 1467-1475.

60. Chen, Z. Small-molecule delivery by nanoparticles for anticancer therapy. *Trends in molecular medicine* **2010**, *16*, 594-602.

61. Mejias, M.; Garcia-Pras, E.; Tiani, C.; Miquel, R.; Bosch, J.; Fernandez, M. Beneficial effects of sorafenib on splanchnic, intrahepatic, and portocollateral circulations in portal hypertensive and cirrhotic rats. *Hepatology* **2009**, *49*, 1245-1256.

62. Ma, R.; Chen, J.; Liang, Y.; Lin, S.; Zhu, L.; Liang, X.; Cai, X. Sorafenib: A potential therapeutic drug for hepatic fibrosis and its outcomes. *Biomedicine & Pharmacotherapy* **2017**, *88*, 459-468.

63. Da Fonseca, L.G.; Barroso-Sousa, R.; Bento, A.d.S.A.; Blanco, B.P.; Valente, G.L.; Pfiffer, T.E.F.; Hoff, P.M.; Sabbaga, J. Safety and efficacy of sorafenib in patients with Child-Pugh B advanced hepatocellular carcinoma. *Molecular and clinical oncology* **2015**, *3*, 793-796.

64. Tran, H.T.; Vong, L.B.; Nishikawa, Y.; Nagasaki, Y. Sorafenib-loaded silica-containing redox nanoparticles for oral anti-liver fibrosis therapy. *Journal of Controlled Release*

2022, *345*, 880-891.

65. Sato, Y.; Murase, K.; Kato, J.; Kobune, M.; Sato, T.; Kawano, Y.; Takimoto, R.; Takada, K.; Miyanishi, K.; Matsunaga, T. Resolution of liver cirrhosis using vitamin A–coupled liposomes to deliver siRNA against a collagen-specific chaperone. *Nature biotechnology* **2008**, *26*, 431-442.

66. Yu, M.; Zheng, J. Clearance pathways and tumor targeting of imaging nanoparticles. *ACS nano* **2015**, *9*, 6655-6674.

67. Kim, K.S.; Hur, W.; Park, S.-J.; Hong, S.W.; Choi, J.E.; Goh, E.J.; Yoon, S.K.; Hahn, S.K. Bioimaging for targeted delivery of hyaluronic acid derivatives to the livers in cirrhotic mice using quantum dots. *ACS nano* **2010**, *4*, 3005-3014.

68. El-Mezayen, N.S.; El-Hadidy, W.F.; El-Refaie, W.M.; Shalaby, T.I.; Khattab, M.M.; El-Khatib, A.S. Oral vitamin-A-coupled valsartan nanomedicine: High hepatic stellate cell receptors accessibility and prolonged enterohepatic residence. *Journal of Controlled Release* **2018**, *283*, 32-44.

69. Qiao, J.-B.; Fan, Q.-Q.; Xing, L.; Cui, P.-F.; He, Y.-J.; Zhu, J.-C.; Wang, L.; Pang, T.; Oh, Y.-K.; Zhang, C. Vitamin A-decorated biocompatible micelles for chemogene therapy of liver fibrosis. *Journal of Controlled Release* **2018**, *283*, 113-125.

70. Fan, Q.-Q.; Zhang, C.-L.; Qiao, J.-B.; Cui, P.-F.; Xing, L.; Oh, Y.-K.; Jiang, H.-L. Extracellular matrix-penetrating nanodrill micelles for liver fibrosis therapy. *Biomaterials* **2020**, *230*, 119616.

71. Hu, M.; Wang, Y.; Xu, L.; An, S.; Tang, Y.; Zhou, X.; Li, J.; Liu, R.; Huang, L. Relaxin gene delivery mitigates liver metastasis and synergizes with check point therapy.

Nature communications **2019**, *10*, 1-13.

72. Li, W.; Zhou, C.; Fu, Y.; Chen, T.; Liu, X.; Zhang, Z.; Gong, T. Targeted delivery of hyaluronic acid nanomicelles to hepatic stellate cells in hepatic fibrosis rats. *Acta Pharmaceutica Sinica B* **2020**, *10*, 693-710.

73. Lee, J.; Byun, J.; Shim, G.; Oh, Y.-K. Fibroblast activation protein activated antifibrotic peptide delivery attenuates fibrosis in mouse models of liver fibrosis. *Nature communications* **2022**, *13*, 1-16.

74. Zhang, C.; Hang, Y.; Tang, W.; Sil, D.; Jensen-Smith, H.C.; Bennett, R.G.; McVicker, B.L.; Oupický, D. Dually Active Polycation/miRNA Nanoparticles for the Treatment of Fibrosis in Alcohol-Associated Liver Disease. *Pharmaceutics* **2022**, *14*, 669.

75. Ribera, J.; Vilches, C.; Sanz, V.; de Miguel, I.; Portoles, I.; Cordoba-Jover, B.; Prat, E.; Nunes, V.; Jimenez, W.; Quidant, R. Treatment of Hepatic Fibrosis in Mice Based on Targeted Plasmonic Hyperthermia. *ACS nano* **2021**, *15*, 7547-7562.

76. Azzam, M.; El Safy, S.; Abdelgelil, S.A.; Weiskirchen, R.; Asimakopoulou, A.; de Lorenzi, F.; Lammers, T.; Mansour, S.; Tammam, S. Targeting activated hepatic stellate cells using collagen-binding chitosan nanoparticles for siRNA delivery to fibrotic livers. *Pharmaceutics* **2020**, *12*, 590.

77. Li, F.; Li, Q.-h.; Wang, J.-y.; Zhan, C.-y.; Xie, C.; Lu, W.-y. Effects of interferon-gamma liposomes targeted to platelet-derived growth factor receptor–beta on hepatic fibrosis in rats. *Journal of controlled release* **2012**, *159*, 261-270.

78. Morsy, M.A.; Nair, A.B. Prevention of rat liver fibrosis by selective targeting of hepatic stellate cells using hesperidin carriers. *International journal of pharmaceutics* **2018**,

552, 241-250.

79. Opanasopit, P.; Sakai, M.; Nishikawa, M.; Kawakami, S.; Yamashita, F.; Hashida, M. Inhibition of liver metastasis by targeting of immunomodulators using mannosylated liposome carriers. *Journal of controlled release* **2002**, *80*, 283-294.

80. Liu, Q.; Wang, X.; Liu, X.; Kumar, S.; Gochman, G.; Ji, Y.; Liao, Y.-P.; Chang, C.H.; Situ, W.; Lu, J. Use of polymeric nanoparticle platform targeting the liver to induce treg-mediated antigen-specific immune tolerance in a pulmonary allergen sensitization model. *ACS nano* **2019**, *13*, 4778-4794.

81. Kawakami, S.; Sato, A.; Nishikawa, M.; Yamashita, F.; Hashida, M. Mannose receptor-mediated gene transfer into macrophages using novel mannosylated cationic liposomes. *Gene therapy* **2000**, *7*, 292-299.

82. He, C.; Yin, L.; Tang, C.; Yin, C. Multifunctional polymeric nanoparticles for oral delivery of TNF-α siRNA to macrophages. *Biomaterials* **2013**, *34*, 2843-2854.

83. Wu, F.; Wuensch, S.A.; Azadniv, M.; Ebrahimkhani, M.R.; Crispe, I.N. Galactosylated LDL nanoparticles: a novel targeting delivery system to deliver antigen to macrophages and enhance antigen specific T cell responses. *Molecular pharmaceutics* **2009**, *6*, 1506-1517.

84. Fischer, H.C.; Hauck, T.S.; Gómez-Aristizábal, A.; Chan, W.C. Exploring primary liver macrophages for studying quantum dot interactions with biological systems. *Advanced Materials* **2010**, *22*, 2520-2524.

85. Higuchi, Y.; Kawakami, S.; Yamashita, F.; Hashida, M. The potential role of fucosylated cationic liposome/NFκB decoy complexes in the treatment of cytokine-

related liver disease. *Biomaterials* **2007**, *28*, 532-539.

86. Zhang, W.; Böttger, R.; Qin, Z.; Kulkarni, J.A.; Vogler, J.; Cullis, P.R.; Li, S.D. Phospholipid-Free Small Unilamellar Vesicles for Drug Targeting to Cells in the Liver. *Small* **2019**, *15*, 1901782.

87. Kim, K.-R.; Kim, J.; Back, J.H.; Lee, J.E.; Ahn, D.-R. Cholesterol-Mediated Seeding of Protein Corona on DNA Nanostructures for Targeted Delivery of Oligonucleotide Therapeutics to Treat Liver Fibrosis. *ACS nano* **2022**.

88. Korin, E.; Bejerano, T.; Cohen, S. GalNAc bio-functionalization of nanoparticles assembled by electrostatic interactions improves siRNA targeting to the liver. *Journal of Controlled Release* **2017**, *266*, 310-320.

89. El-Marakby, E.M.; Hathout, R.M.; Taha, I.; Mansour, S.; Mortada, N.D. A novel serum-stable liver targeted cytotoxic system using valerate-conjugated chitosan nanoparticles surface decorated with glycyrrhizin. *International Journal of Pharmaceutics* **2017**, *525*, 123-138.

90. Mishra, D.; Jain, N.; Rajoriya, V.; Jain, A.K. Glycyrrhizin conjugated chitosan nanoparticles for hepatocyte-targeted delivery of lamivudine. *Journal of Pharmacy and Pharmacology* **2014**, *66*, 1082-1093.

91. Takei, Y.; Maruyama, A.; Ferdous, A.; Nishimura, Y.; Kawano, S.; Ikejima, K.; Okumura, S.; Asayama, S.; Nogawa, M.; Hashimoto, M. Targeted gene delivery to sinusoidal endothelial cells: DNA nanoassociate bearing hyaluronan-glycocalyx. *The FASEB journal* **2004**, *18*, 699-701.

92. Bhang, S.H.; Won, N.; Lee, T.-J.; Jin, H.; Nam, J.; Park, J.; Chung, H.; Park, H.-S.;

Sung, Y.-E.; Hahn, S.K. Hyaluronic acid− quantum dot conjugates for in vivo lymphatic vessel imaging. *ACS nano* **2009**, *3*, 1389-1398.

93. Hunt, N.J.; Lockwood, G.P.; Le Couteur, F.H.; McCourt, P.A.; Singla, N.; Kang, S.W.S.; Burgess, A.; Kuncic, Z.; Le Couteur, D.G.; Cogger, V.C. Rapid intestinal uptake and targeted delivery to the liver endothelium using orally administered silver sulfide quantum dots. *ACS nano* **2020**, *14*, 1492-1507.

94. Lee, M.-Y.; Yang, J.-A.; Jung, H.S.; Beack, S.; Choi, J.E.; Hur, W.; Koo, H.; Kim, K.; Yoon, S.K.; Hahn, S.K. Hyaluronic acid–gold nanoparticle/interferon α complex for targeted treatment of hepatitis C virus infection. *ACS nano* **2012**, *6*, 9522-9531.

95. Marrone, G.; Shah, V.H.; Gracia-Sancho, J. Sinusoidal communication in liver fibrosis and regeneration. *Journal of hepatology* **2016**, *65*, 608-617.

96. Özkan, A.; Stolley, D.; Cressman, E.N.; McMillin, M.; DeMorrow, S.; Yankeelov, T.E.; Rylander, M.N. The influence of chronic liver diseases on hepatic vasculature: A liver-on-a-chip review. *Micromachines* **2020**, *11*, 487.

97. Hoshyar, N.; Gray, S.; Han, H.; Bao, G. The effect of nanoparticle size on in vivo pharmacokinetics and cellular interaction. *Nanomedicine* **2016**, *11*, 673-692.

98. Naito, M.; Hasegawa, G.; Takahashi, K. Development, differentiation, and maturation of Kupffer cells. *Microscopy research and technique* **1997**, *39*, 350-364.

99. Davies, L.C.; Jenkins, S.J.; Allen, J.E.; Taylor, P.R. Tissue-resident macrophages. *Nature immunology* **2013**, *14*, 986-995.

100. Dixon, L.J.; Barnes, M.; Tang, H.; Pritchard, M.T.; Nagy, L.E. Kupffer cells in the liver. *Comprehensive Physiology* **2013**, *3*, 785.

101. Suk, J.S.; Xu, Q.; Kim, N.; Hanes, J.; Ensign, L.M. PEGylation as a strategy for improving nanoparticle-based drug and gene delivery. *Advanced drug delivery reviews* **2016**, *99*, 28-51.

102. Lila, A.S.A.; Nawata, K.; Shimizu, T.; Ishida, T.; Kiwada, H. Use of polyglycerol (PG), instead of polyethylene glycol (PEG), prevents induction of the accelerated blood clearance phenomenon against long-circulating liposomes upon repeated administration. *International journal of pharmaceutics* **2013**, *456*, 235-242.

103. Dawidczyk, C.M.; Kim, C.; Park, J.H.; Russell, L.M.; Lee, K.H.; Pomper, M.G.; Searson, P.C. State-of-the-art in design rules for drug delivery platforms: lessons learned from FDA-approved nanomedicines. *Journal of Controlled Release* **2014**, *187*, 133-144.

104. Bhandari, S.; Larsen, A.K.; McCourt, P.; Smedsrød, B.; Sørensen, K.K. The scavenger function of liver sinusoidal endothelial cells in health and disease. *Frontiers in Physiology* **2021**, 1711.

105. Deaciuc, I.V.; Alappat, J.M.; McDonough, K.H.; D'Souza, N.B. Effect of chronic alcohol consumption by rats on tumor necrosis factor-α and interleukin-6 clearance in vivo and by the isolated, perfused liver. *Biochemical pharmacology* **1996**, *52*, 891-899.

106. Wisse, E.; Jacobs, F.; Topal, B.; Frederik, P.; De Geest, B. The size of endothelial fenestrae in human liver sinusoids: implications for hepatocyte-directed gene transfer. *Gene therapy* **2008**, *15*, 1193-1199.

107. Poisson, J.; Lemoinne, S.; Boulanger, C.; Durand, F.; Moreau, R.; Valla, D.; Rautou, P.-E. Liver sinusoidal endothelial cells: Physiology and role in liver diseases. *Journal*

of hepatology **2017**, *66*, 212-227.

108. Zhang, L.-F.; Wang, X.-H.; Zhang, C.-L.; Lee, J.; Duan, B.-W.; Xing, L.; Li, L.; Oh, Y.-K.; Jiang, H.-L. Sequential Nano-Penetrators of Capillarized Liver Sinusoids and Extracellular Matrix Barriers for Liver Fibrosis Therapy. *ACS nano* **2022**, *16*, 14029-14042.

109. Chen, Y.; Huang, Y.; Li, Q.; Luo, Z.; Zhang, Z.; Huang, H.; Sun, J.; Zhang, L.; Sun, R.; Bain, D.J. Targeting Xkr8 via nanoparticle-mediated in situ co-delivery of siRNA and chemotherapy drugs for cancer immunochemotherapy. *Nature Nanotechnology* **2023**, *18*, 193-204.

110. Dhar, D.; Antonucci, L.; Nakagawa, H.; Kim, J.Y.; Glitzner, E.; Caruso, S.; Shalapour, S.; Yang, L.; Valasek, M.A.; Lee, S. Liver cancer initiation requires p53 inhibition by CD44-enhanced growth factor signaling. *Cancer cell* **2018**, *33*, 1061-1077. e1066.

111. Bartneck, M. Lipid nanoparticle formulations for targeting leukocytes with therapeutic RNA in liver fibrosis. *Advanced Drug Delivery Reviews* **2021**, *173*, 70-88.

112. Hayashi, Y.; Takamiya, M.; Jensen, P.B.; Ojea-Jimenez, I.; Claude, H.; Antony, C.; Kjaer-Sorensen, K.; Grabher, C.; Boesen, T.; Gilliland, D. Differential nanoparticle sequestration by macrophages and scavenger endothelial cells visualized in vivo in real-time and at ultrastructural resolution. *ACS nano* **2020**, *14*, 1665-1681.

113. Sørensen, K.K.; McCourt, P.; Berg, T.; Crossley, C.; Couteur, D.L.; Wake, K.; Smedsrød, B. The scavenger endothelial cell: a new player in homeostasis and immunity. *American Journal of Physiology-Regulatory, Integrative and Comparative Physiology* **2012**, *303*, R1217-R1230.

114. Campbell, F.; Bos, F.L.; Sieber, S.; Arias-Alpizar, G.; Koch, B.E.; Huwyler, J.r.; Kros, A.; Bussmann, J. Directing nanoparticle biodistribution through evasion and exploitation of Stab2-dependent nanoparticle uptake. *ACS nano* **2018**, *12*, 2138-2150.

115. Limmer, A.; Ohl, J.; Kurts, C.; Ljunggren, H.-G.; Reiss, Y.; Groettrup, M.; Momburg, F.; Arnold, B.; Knolle, P.A. Efficient presentation of exogenous antigen by liver endothelial cells to CD8+ T cells results in antigen-specific T-cell tolerance. *Nature medicine* **2000**, *6*, 1348-1354.

116. Kim, M.; Jeong, M.; Hur, S.; Cho, Y.; Park, J.; Jung, H.; Seo, Y.; Woo, H.; Nam, K.; Lee, K. Engineered ionizable lipid nanoparticles for targeted delivery of RNA therapeutics into different types of cells in the liver. *Science Advances* **2021**, *7*, eabf4398.

117. Lee, A.-R.; Nam, K.; Lee, B.J.; Lee, S.-W.; Baek, S.-M.; Bang, J.-S.; Choi, S.-K.; Park, S.-J.; Kim, T.-H.; Jeong, K.-S. Hepatic Cellular Distribution of Silica Nanoparticles by Surface Energy Modification. *International journal of molecular sciences* **2019**, *20*, 3812.

118. Donohue, T.M.; Osna, N.A.; Clemens, D.L. Recombinant Hep G2 cells that express alcohol dehydrogenase and cytochrome P450 2E1 as a model of ethanol-elicited cytotoxicity. *The international journal of biochemistry & cell biology* **2006**, *38*, 92-101.

119. CUNNINGHAM, C.C.; COLEMAN, W.B.; SPACH, P.I. The effects of chronic ethanol consumption on hepatic mitochondrial energy metabolism. *Alcohol and Alcoholism* **1990**, *25*, 127-136.

120. Harjumäki, R.; Pridgeon, C.S.; Ingelman-Sundberg, M. CYP2E1 in alcoholic and non-

alcoholic liver injury. Roles of ROS, reactive intermediates and lipid overload. *International Journal of Molecular Sciences* **2021**, *22*, 8221.

121. Gao, B.; Bataller, R. Alcoholic liver disease: pathogenesis and new therapeutic targets. *Gastroenterology* **2011**, *141*, 1572-1585.

122. Sato, Y.; Kinami, Y.; Hashiba, K.; Harashima, H. Different kinetics for the hepatic uptake of lipid nanoparticles between the apolipoprotein E/low density lipoprotein receptor and the N-acetyl-d-galactosamine/asialoglycoprotein receptor pathway. *Journal of Controlled Release* **2020**, *322*, 217-226.

123. Lin, C.; Mostafa, A.; Jans, A.; Wolters, J.C.; Mohamed, M.R.; Van der Vorst, E.P.; Trautwein, C.; Bartneck, M. Targeting Ligand Independent Tropism of siRNA-LNP by Small Molecules for Directed Therapy of Liver or Myeloid Immune Cells. *Advanced Healthcare Materials* **2023**, 2202670.

124. Kulkarni, J.A.; Darjuan, M.M.; Mercer, J.E.; Chen, S.; Van Der Meel, R.; Thewalt, J.L.; Tam, Y.Y.C.; Cullis, P.R. On the formation and morphology of lipid nanoparticles containing ionizable cationic lipids and siRNA. *ACS nano* **2018**, *12*, 4787-4795.

125. Akinc, A.; Querbes, W.; De, S.; Qin, J.; Frank-Kamenetsky, M.; Jayaprakash, K.N.; Jayaraman, M.; Rajeev, K.G.; Cantley, W.L.; Dorkin, J.R. Targeted delivery of RNAi therapeutics with endogenous and exogenous ligand-based mechanisms. *Molecular Therapy* **2010**, *18*, 1357-1364.

126. Gilleron, J.; Querbes, W.; Zeigerer, A.; Borodovsky, A.; Marsico, G.; Schubert, U.; Manygoats, K.; Seifert, S.; Andree, C.; Stöter, M. Image-based analysis of lipid nanoparticle–mediated siRNA delivery, intracellular trafficking and endosomal escape.

Nature biotechnology **2013**, *31*, 638-646.

127. Debacker, A.J.; Voutila, J.; Catley, M.; Blakey, D.; Habib, N. Delivery of oligonucleotides to the liver with GalNAc: from research to registered therapeutic drug. *Molecular Therapy* **2020**, *28*, 1759-1771.

128. Nie, H.; Liu, X.-M.; Yang, Q.-X.; Luo, X.-D.; Zhao, Y.; Zhang, S.-Y. Effect of hydrophile–lipophile balance of the linker in Gal/GalNAc ligands on high-affinity binding of galactosylated liposomes by the asialoglycoprotein receptor. *International Journal of Pharmaceutics* **2022**, *624*, 121967.

129. Zhang, Y.-N.; Poon, W.; Tavares, A.J.; McGilvray, I.D.; Chan, W.C. Nanoparticle–liver interactions: cellular uptake and hepatobiliary elimination. *Journal of controlled release* **2016**, *240*, 332-348.

130. Zhou, L.; Liang, Q.; Li, Y.; Cao, Y.; Li, J.; Yang, J.; Liu, J.; Bi, J.; Liu, Y. Collagenase-I decorated co-delivery micelles potentiate extracellular matrix degradation and hepatic stellate cell targeting for liver fibrosis therapy. *Acta Biomaterialia* **2022**, *152*, 235-254.

131. Borkham-Kamphorst, E.; Weiskirchen, R. The PDGF system and its antagonists in liver fibrosis. *Cytokine & growth factor reviews* **2016**, *28*, 53-61.

132. Luk, J.M.; Zhang, Q.S.; Lee, N.P.; Wo, J.Y.; Leung, P.P.; Liu, L.X.; Hu, M.Y.; Cheung, K.F.; Hui, C.K.; Lau, G.K. Hepatic stellate cell-targeted delivery of M6P-HSA-glycyrrhetinic acid attenuates hepatic fibrogenesis in a bile duct ligation rat model. *Liver International* **2007**, *27*, 548-557.

133. Hong, F.; Tuyama, A.; Lee, T.F.; Loke, J.; Agarwal, R.; Cheng, X.; Garg, A.; Fiel, M.I.; Schwartz, M.; Walewski, J. Hepatic stellate cells express functional CXCR4: Role in

stromal cell–derived factor-1α–mediated stellate cell activation. *Hepatology* **2009**, *49*, 2055-2067.

134. Wald, O.; Pappo, O.; Safadi, R.; Dagan-Berger, M.; Beider, K.; Wald, H.; Franitza, S.; Weiss, I.; Avniel, S.; Boaz, P. Involvement of the CXCL12/CXCR4 pathway in the advanced liver disease that is associated with hepatitis C virus or hepatitis B virus. *European journal of immunology* **2004**, *34*, 1164-1174.

135. Liu, C.-H.; Chan, K.-M.; Chiang, T.; Liu, J.-Y.; Chern, G.-G.; Hsu, F.-F.; Wu, Y.-H.; Liu, Y.-C.; Chen, Y. Dual-functional nanoparticles targeting CXCR4 and delivering antiangiogenic siRNA ameliorate liver fibrosis. *Molecular pharmaceutics* **2016**, *13*, 2253-2262.

136. Bajaj, J.S. Alcohol, liver disease and the gut microbiota. *Nature Reviews Gastroenterology & Hepatology* **2019**, *16*, 235-246.

137. Rehm, J.; Shield, K.D. Global burden of alcohol use disorders and alcohol liver disease. *Biomedicines* **2019**, *7*, 99.

138. Teschke, R. Alcoholic liver disease: alcohol metabolism, cascade of molecular mechanisms, cellular targets, and clinical aspects. *Biomedicines* **2018**, *6*, 106.

139. Shim, Y.-R.; Jeong, W.-I. Recent advances of sterile inflammation and inter-organ cross-talk in alcoholic liver disease. *Experimental & Molecular Medicine* **2020**, *52*, 772-780.

140. Ju, C.; Tacke, F. Hepatic macrophages in homeostasis and liver diseases: from pathogenesis to novel therapeutic strategies. *Cellular & molecular immunology* **2016**, *13*, 316-327.

141. Anselmo, A.C.; Gupta, V.; Zern, B.J.; Pan, D.; Zakrewsky, M.; Muzykantov, V.; Mitragotri, S. Delivering nanoparticles to lungs while avoiding liver and spleen through adsorption on red blood cells. *ACS nano* **2013**, *7*, 11129-11137.

142. Yoo, J.-W.; Chambers, E.; Mitragotri, S. Factors that control the circulation time of nanoparticles in blood: challenges, solutions and future prospects. *Current pharmaceutical design* **2010**, *16*, 2298-2307.

143. Sung, Y.-C.; Liu, Y.-C.; Chao, P.-H.; Chang, C.-C.; Jin, P.-R.; Lin, T.-T.; Lin, J.-A.; Cheng, H.-T.; Wang, J.; Lai, C.P. Combined delivery of sorafenib and a MEK inhibitor using CXCR4-targeted nanoparticles reduces hepatic fibrosis and prevents tumor development. *Theranostics* **2018**, *8*, 894.

144. Lin, T.-T.; Gao, D.-Y.; Liu, Y.-C.; Sung, Y.-C.; Wan, D.; Liu, J.-Y.; Chiang, T.; Wang, L.; Chen, Y. Development and characterization of sorafenib-loaded PLGA nanoparticles for the systemic treatment of liver fibrosis. *Journal of controlled release* **2016**, *221*, 62-70.

145. Paunovska, K.; Da Silva Sanchez, A.J.; Sago, C.D.; Gan, Z.; Lokugamage, M.P.; Islam, F.Z.; Kalathoor, S.; Krupczak, B.R.; Dahlman, J.E. Nanoparticles containing oxidized cholesterol deliver mRNA to the liver microenvironment at clinically relevant doses. *Advanced Materials* **2019**, *31*, 1807748.

146. Maugeri, M.; Nawaz, M.; Papadimitriou, A.; Angerfors, A.; Camponeschi, A.; Na, M.; Hölttä, M.; Skantze, P.; Johansson, S.; Sundqvist, M. Linkage between endosomal escape of LNP-mRNA and loading into EVs for transport to other cells. *Nature communications* **2019**, *10*, 1-15.

147. Richter, L.R.; Wan, Q.; Wen, D.; Zhang, Y.; Yu, J.; Kang, J.k.; Zhu, C.; McKinnon, E.L.; Gu, Z.; Qiang, L. Targeted delivery of notch inhibitor attenuates obesity-induced glucose intolerance and liver fibrosis. *ACS nano* **2020**, *14*, 6878-6886.

148. Torres, J.-L.; Novo-Veleiro, I.; Manzanedo, L.; Alvela-Suárez, L.; Macías, R.; Laso, F.-J.; Marcos, M. Role of microRNAs in alcohol-induced liver disorders and non-alcoholic fatty liver disease. *World journal of gastroenterology* **2018**, *24*, 4104.

149. Li, Z.; Rana, T.M. Therapeutic targeting of microRNAs: current status and future challenges. *Nature reviews Drug discovery* **2014**, *13*, 622-638.

150. Burnett, J.C.; Rossi, J.J. RNA-based therapeutics: current progress and future prospects. *Chemistry & biology* **2012**, *19*, 60-71.

151. Bala, S.; Szabo, G. MicroRNA signature in alcoholic liver disease. *International journal of hepatology* **2012**, *2012*.

152. Szabo, G.; Bala, S. Alcoholic liver disease and the gut-liver axis. *World journal of gastroenterology: WJG* **2010**, *16*, 1321.

153. Seth, D.; Haber, P.S.; Syn, W.K.; Diehl, A.M.; Day, C.P. Pathogenesis of alcohol-induced liver disease: Classical concepts and recent advances. *Journal of gastroenterology and hepatology* **2011**, *26*, 1089-1105.

154. Chen, Y.; Huang, Y.; Reiberger, T.; Duyverman, A.M.; Huang, P.; Samuel, R.; Hiddingh, L.; Roberge, S.; Koppel, C.; Lauwers, G.Y. Differential effects of sorafenib on liver versus tumor fibrosis mediated by stromal-derived factor 1 alpha/C-X-C receptor type 4 axis and myeloid differentiation antigen–positive myeloid cell infiltration in mice. *Hepatology* **2014**, *59*, 1435-1447.

155. Xie, Y.; Hang, Y.; Wang, Y.; Sleightholm, R.; Prajapati, D.R.; Bader, J.; Yu, A.; Tang, W.; Jaramillo, L.; Li, J. Stromal modulation and treatment of metastatic pancreatic cancer with local intraperitoneal triple miRNA/siRNA nanotherapy. *ACS nano* **2020**, *14*, 255-271.

156. Xie, Y.; Wang, Y.; Li, J.; Hang, Y.; Jaramillo, L.; Wehrkamp, C.J.; Phillippi, M.A.; Mohr, A.M.; Chen, Y.; Talmon, G.A. Cholangiocarcinoma therapy with nanoparticles that combine downregulation of MicroRNA-210 with inhibition of cancer cell invasiveness. *Theranostics* **2018**, *8*, 4305.

157. Wang, Y.; Xie, Y.; Williams, J.; Hang, Y.; Richter, L.; Becker, M.; Amador, C.; Oupický, D.; Hyde, R.K. Use of polymeric CXCR4 inhibitors as siRNA delivery vehicles for the treatment of acute myeloid leukemia. *Cancer Gene Therapy* **2020**, *27*, 45-55.

158. Gerlach, L.O.; Skerlj, R.T.; Bridger, G.J.; Schwartz, T.W. Molecular interactions of cyclam and bicyclam non-peptide antagonists with the CXCR4 chemokine receptor. *Journal of Biological Chemistry* **2001**, *276*, 14153-14160.

159. Zhou, Y.; Yu, F.; Zhang, F.; Chen, G.; Wang, K.; Sun, M.; Li, J.; Oupický, D. Cyclam-modified PEI for combined VEGF siRNA silencing and CXCR4 inhibition to treat metastatic breast cancer. *Biomacromolecules* **2018**, *19*, 392-401.

160. Xu, L.; Hui, A.; Albanis, E.; Arthur, M.; O'byrne, S.; Blaner, W.; Mukherjee, P.; Friedman, S.; Eng, F. Human hepatic stellate cell lines, LX-1 and LX-2: new tools for analysis of hepatic fibrosis. *Gut* **2005**, *54*, 142-151.

161. Chiang, D.J.; Roychowdhury, S.; Bush, K.; McMullen, M.R.; Pisano, S.; Niese, K.; Olman, M.A.; Pritchard, M.T.; Nagy, L.E. Adenosine 2A receptor antagonist prevented

and reversed liver fibrosis in a mouse model of ethanol-exacerbated liver fibrosis. *PLoS One* **2013**, *8*, e69114.

162. Schneider, C.A.; Rasband, W.S.; Eliceiri, K.W. NIH Image to ImageJ: 25 years of image analysis. *Nature methods* **2012**, *9*, 671-675.

163. Magee, D.; Treanor, D.; Crellin, D.; Shires, M.; Smith, K.; Mohee, K.; Quirke, P. Colour normalisation in digital histopathology images. In Proceedings of the Proc Optical Tissue Image analysis in Microscopy, Histopathology and Endoscopy (MICCAI Workshop), 2009; pp. 100-111.

164. Ruifrok, A.C.; Johnston, D.A. Quantification of histochemical staining by color deconvolution. *Analytical and quantitative cytology and histology* **2001**, *23*, 291-299.

165. Toth, Z.E.; Mezey, E. Simultaneous visualization of multiple antigens with tyramide signal amplification using antibodies from the same species. *Journal of Histochemistry & Cytochemistry* **2007**, *55*, 545-554.

166. Schindelin, J.; Arganda-Carreras, I.; Frise, E.; Kaynig, V.; Longair, M.; Pietzsch, T.; Preibisch, S.; Rueden, C.; Saalfeld, S.; Schmid, B. Fiji: an open-source platform for biological-image analysis. *Nature methods* **2012**, *9*, 676-682.

167. Bredfeldt, J.S.; Liu, Y.; Conklin, M.W.; Keely, P.J.; Mackie, T.R.; Eliceiri, K.W. Automated quantification of aligned collagen for human breast carcinoma prognosis. *Journal of pathology informatics* **2014**, *5*, 28.

168. Bredfeldt, J.S.; Liu, Y.; Pehlke, C.A.; Conklin, M.W.; Szulczewski, J.M.; Inman, D.R.; Keely, P.J.; Nowak, R.D.; Mackie, T.R.; Eliceiri, K.W. Computational segmentation of collagen fibers from second-harmonic generation images of breast cancer. *Journal of*

biomedical optics **2014**, *19*, 016007.

169. Wu, P.; Luo, X.; Wu, H.; Yu, F.; Wang, K.; Sun, M.; Oupicky, D. Cholesterol Modification Enhances Antimetastatic Activity and siRNA Delivery Efficacy of Poly (ethylenimine)-Based CXCR4 Antagonists. *Macromolecular Bioscience* **2018**, *18*, 1800234.

170. Taranejoo, S.; Liu, J.; Verma, P.; Hourigan, K. A review of the developments of characteristics of PEI derivatives for gene delivery applications. *Journal of Applied Polymer Science* **2015**, *132*.

171. Cicchi, R.; Vogler, N.; Kapsokalyvas, D.; Dietzek, B.; Popp, J.; Pavone, F.S. From molecular structure to tissue architecture: collagen organization probed by SHG microscopy. *Journal of biophotonics* **2013**, *6*, 129-142.

172. Urashima, S.; Tsutsumi, M.; Ozaki, K.; Tsuchishima, M.; Shimanaka, K.; Ueshima, Y.; Takase, S. Immunohistochemical study of hyaluronate receptor (CD44) in alcoholic liver disease. *Alcoholism: Clinical and Experimental Research* **2000**, *24*, 34S-38S.

173. Liu, J.-Y.; Chiang, T.; Liu, C.-H.; Chern, G.-G.; Lin, T.-T.; Gao, D.-Y.; Chen, Y. Delivery of siRNA using CXCR4-targeted nanoparticles modulates tumor microenvironment and achieves a potent antitumor response in liver cancer. *Molecular Therapy* **2015**, *23*, 1772-1782.

174. Saiman, Y.; Jiao, J.; Fiel, M.I.; Friedman, S.L.; Aloman, C.; Bansal, M.B. Inhibition of the CXCL 12/CXCR 4 chemokine axis with AMD 3100, a CXCR 4 small molecule inhibitor, worsens murine hepatic injury. *Hepatology Research* **2015**, *45*, 794-803.

175. Mavier, P.; Martin, N.; Couchie, D.; Préaux, A.-M.; Laperche, Y.; Zafrani, E.S.

Expression of stromal cell-derived factor-1 and of its receptor CXCR4 in liver regeneration from oval cells in rat. *The American journal of pathology* **2004**, *165*, 1969-1977.

176. Baeck, C.; Wei, X.; Bartneck, M.; Fech, V.; Heymann, F.; Gassler, N.; Hittatiya, K.; Eulberg, D.; Luedde, T.; Trautwein, C. Pharmacological inhibition of the chemokine C-C motif chemokine ligand 2 (monocyte chemoattractant protein 1) accelerates liver fibrosis regression by suppressing Ly-6C+ macrophage infiltration in mice. *Hepatology* **2014**, *59*, 1060-1072.

177. Cubero, F.; Nieto, N. Kupffer cells and alcoholic liver disease. *Revista Espanola de Enfermedades Digestivas* **2006**, *98*, 460.

178. Surendran, S.P.; Thomas, R.G.; Moon, M.J.; Jeong, Y.Y. Nanoparticles for the treatment of liver fibrosis. *International journal of nanomedicine* **2017**, *12*, 6997.

179. Dai, W.; Zhao, J.; Tang, N.; Zeng, X.; Wu, K.; Ye, C.; Shi, J.; Lu, C.; Ning, B.; Zhang, J. Micro RNA-155 attenuates activation of hepatic stellate cell by simultaneously preventing EMT process and ERK 1 signalling pathway. *Liver International* **2015**, *35*, 1234-1243.

180. Yoon, H.Y.; Kim, H.R.; Saravanakumar, G.; Heo, R.; Chae, S.Y.; Um, W.; Kim, K.; Kwon, I.C.; Lee, J.Y.; Lee, D.S. Bioreducible hyaluronic acid conjugates as siRNA carrier for tumor targeting. *Journal of controlled release* **2013**, *172*, 653-661.

181. Liang, H.; Li, Z.; Ren, Z.; Jia, Q.; Guo, L.; Li, S.; Zhang, H.; Hu, S.; Zhu, D.; Shen, D. Light-triggered NO-releasing nanoparticles for treating mice with liver fibrosis. *Nano Research* **2020**, *13*, 2197-2202.

182. Tang, W.; Panja, S.; Jogdeo, C.M.; Tang, S.; Ding, L.; Yu, A.; Foster, K.W.; Dsouza, D.L.; Chhonker, Y.S.; Jensen-Smith, H. Modified chitosan for effective renal delivery of siRNA to treat acute kidney injury. *Biomaterials* **2022**, *285*, 121562.

183. Lynch, R.W.; Hawley, C.A.; Pellicoro, A.; Bain, C.C.; Iredale, J.P.; Jenkins, S.J. An efficient method to isolate Kupffer cells eliminating endothelial cell contamination and selective bias. *Journal of leukocyte biology* **2018**, *104*, 579-586.

184. Ergen, C.; Heymann, F.; Gremse, F.; Bartneck, M.; Panzer, U.; Pola, R.; Pechar, M.; Storm, G.; Mohr, N.; Barz, M. Targeting distinct myeloid cell populations in vivo using polymers, liposomes and microbubbles. *Biomaterials* **2017**, *114*, 106-120.

185. Zhang, L.; He, J.; Wang, J.; Liu, J.; Chen, Z.; Deng, B.; Wei, L.; Wu, H.; Liang, B.; Li, H. Knockout RAGE alleviates cardiac fibrosis through repressing endothelial-to-mesenchymal transition (EndMT) mediated by autophagy. *Cell Death & Disease* **2021**, *12*, 470.

186. Liu, P.; Mao, Y.; Xie, Y.; Wei, J.; Yao, J. Stem cells for treatment of liver fibrosis/cirrhosis: clinical progress and therapeutic potential. *Stem Cell Research & Therapy* **2022**, *13*, 1-20.

187. Ma, P.-F.; Gao, C.-C.; Yi, J.; Zhao, J.-L.; Liang, S.-Q.; Zhao, Y.; Ye, Y.-C.; Bai, J.; Zheng, Q.-J.; Dou, K.-F. Cytotherapy with M1-polarized macrophages ameliorates liver fibrosis by modulating immune microenvironment in mice. *Journal of Hepatology* **2017**, *67*, 770-779.

188. Lee, S.; Kivimäe, S.; Dolor, A.; Szoka, F.C. Macrophage-based cell therapies: the long and winding road. *Journal of Controlled Release* **2016**, *240*, 527-540.

189. Chan, M.W.Y.; Viswanathan, S. Recent progress on developing exogenous monocyte/macrophage-based therapies for inflammatory and degenerative diseases. *Cytotherapy* **2019**, *21*, 393-415.

190. Lopes, J.; Lopes, D.; Pereira-Silva, M.; Peixoto, D.; Veiga, F.; Hamblin, M.R.; Conde, J.; Corbo, C.; Zare, E.N.; Ashrafizadeh, M. Macrophage Cell Membrane-Cloaked Nanoplatforms for Biomedical Applications. *Small methods* **2022**, *6*, 2200289.

191. Piotrowski-Daspit, A.S.; Kauffman, A.C.; Bracaglia, L.G.; Saltzman, W.M. Polymeric vehicles for nucleic acid delivery. *Advanced drug delivery reviews* **2020**, *156*, 119-132.

192. Li, J.; Chen, C.; Xia, T. Understanding Nanomaterial–Liver Interactions to Facilitate the Development of Safer Nanoapplications. *Advanced Materials* **2022**, *34*, 2106456.

193. Parodi, A.; Quattrocchi, N.; Van De Ven, A.L.; Chiappini, C.; Evangelopoulos, M.; Martinez, J.O.; Brown, B.S.; Khaled, S.Z.; Yazdi, I.K.; Enzo, M.V. Synthetic nanoparticles functionalized with biomimetic leukocyte membranes possess cell-like functions. *Nature nanotechnology* **2013**, *8*, 61-68.

194. Cao, H.; Dan, Z.; He, X.; Zhang, Z.; Yu, H.; Yin, Q.; Li, Y. Liposomes coated with isolated macrophage membrane can target lung metastasis of breast cancer. *ACS nano* **2016**, *10*, 7738-7748.

195. Kisseleva, T. The origin of fibrogenic myofibroblasts in fibrotic liver. *Hepatology* **2017**, *65*, 1039-1043.

196. Taimr, P.; Higuchi, H.; Kocova, E.; Rippe, R.A.; Friedman, S.; Gores, G.J. Activated stellate cells express the TRAIL receptor-2/death receptor-5 and undergo TRAIL-mediated apoptosis. *Hepatology* **2003**, *37*, 87-95.

197. Lamas-Paz, A.; Hao, F.; Nelson, L.J.; Vázquez, M.T.; Canals, S.; Del Moral, M.G.; Martínez-Naves, E.; Nevzorova, Y.A.; Cubero, F.J. Alcoholic liver disease: Utility of animal models. *World journal of gastroenterology* **2018**, *24*, 5063.

198. Leo, M.A.; Lieber, C.S. Hepatic fibrosis after long-term administration of ethanol and moderate vitamin A supplementation in the rat. *Hepatology* **1983**, *3*, 1-11.